SURFACE RADIATION AND ENERGY BALANCES AT A MID-LATITUDE ALPINE TUNDRA SITE DURING THE SUMMER

by

James Dorrance Bowers

B.A., University of Victoria, 1978

THESIS SUBMITTED IN PARTIAL FULFILLMENT OF
THE REQUIREMENTS FOR THE DEGREE OF
MASTER OF SCIENCE
in the Department
of
Geography

SIMON FRASER UNIVERSITY

January, 1988

APPROVAL

Name: James Dorrance Bowers

Degree: Master of Science

Title of Thesis: Surface Radiation and Energy Balances at a Mid-Latitude Alpine Tundra Site During the Summer

Examining Committee:

Chairman: J.T. Pierce

W.G Bailey
Senior Supervisor

S.T. Wong
Professor

R.B.Sagar
Associate Professor

R.G. Wilson
External Examiner
Director, Air Management Program
B.C. Ministry of Environment and Parks

Date Approved: Jan 14, 1988

PARTIAL COPYRIGHT LICENSE

Title of Thesis/Project/Extended Essay

Surface Radiation and Energy Balances at a

Mid-Latitude Alpine Tundra Site During the Summer

Author:

(signature)

James Dorrance Bowers

(name)

April 21, 1988

(date)

ABSTRACT

The high solar irradiance, strong and persistent winds, limited soil and vegetation development and especially adapted vegetation of the alpine tundra will result in unique and characteristic surface energy regimes. Despite the areal and hydrological significance of alpine tundra environments, there have been few North American studies on those regimes.

To address this lack of information, measurements of the energy and radiation balances were made at Plateau Mountain (2475 m asl) in southwestern Alberta, Canada. Half-hourly flux densities of the components of the radiation and energy balances were determined continuously for the period June 26 - July 26, 1985. Global solar, reflected solar and net radiation flux densities were measured directly. These data were used, in combination with surface temperature measurements, to determine incoming and outgoing longwave radiation flux densities. The Bowen ratio-energy balance approach was used to determine the sensible and latent heat flux densities. Windspeed profile measurements were also made and allowed the aerodynamic characteristics of the surface to be determined. This information, combined with surface temperature and windspeed measurements, permitted the use of an Ohm's law analog approach to determine the sensible heat flux. Sensible heat flux densites were also determined, for portions of the investigation, using the eddy correlation approach.

The surface radiation regime was primarily controlled by atmospheric transmissivity which reached maximum values in excess of 80%. Daily albedo was essentially constant at 17%. Global solar radiation flux densities were generally greater than 25 MJ m^{-2}. Daily incoming longwave radiation flux densities ranged from 17.3 - 24.3 MJ m^{-2} and outgoing values ranged from 26.3 - 32.1 MJ m^{-2}. Daily net radiation flux densities averaged 12.2 MJ m^{-2}. The empirical relationship between net radiation and global solar radiation at this site was similar to relationships observed at lower elevation sites.

The energy balance was dominated by the sensible heat flux. The average daylight period sensible heat flux density was 67% greater than the latent heat flux density. Latent heat flux densities translated to evaporation rates of 1 - 4 mm per day. Soil heat flux densities were on average 10 - 15% of net radiation flux densities. The half-hourly sensible heat flux densities determined using the Ohm's law and eddy correlation approaches agreed very well with the Bowen ratio measurements. The energy balance was strongly affected by the surface's dynamic and variable control over the movement of water vapour to the atmosphere. A large element of this control appeared to be due to the physiological response of vegetation to changing environmental conditions, although the surface was only partially vegetated.

The estimated half-hourly latent heat flux densities from an energy balance based model, which only requires standard climatological and surface temperature data, were compared with the measured values. The model's performance was found to be reasonably good. On average, model estimates were within ±71.5 W m^{-2} of the measured values. The possibility of using a model based on the equilibrium evaporation concept for daylight period or daily latent heat flux densities was also considered. The potential of this approach was limited by the variable nature of the alpine tundra surface's control over the movement of water to the atmosphere.

ACKNOWLEDGEMENTS

Funding was provided by N.S.E.R.C. (operating grant A2614 held by W.G. Bailey), Campbell Scientific Research Corporation of Canada and Simon Fraser University. Permission to conduct research on Plateau Mountain was kindly provided by the Alberta Ministry of Energy and Natural Resources. I would also like to thank the Alberta Ministry of Recreation and Parks for allowing our extended stay at the Cataract Creek campground. Dr. J.A. Davies, of McMaster University, provided the windspeed profile system.

The knowledge, support and patience of my senior supervisor, Dr. W.G. Bailey were welcomed at all stages of the study. The successes in this thesis are largely due to Bill's keen interest and participation. The inciteful comments and suggestions of the other members of the examining comittee, R.B. Sagar, Dr. S.T. Wong and Dr. R.G. Wilson also improved the thesis significantly.

E.J. Weick, my field assistant, lived in a tent and ate my cooking for over six weeks without complaint. I wish Ted equal luck in finding competent and easygoing assistance for his investigations. R.J. Stathers assisted in the field during the early portion of the experiment, and his programs were the basis for much of the analysis. We are all grateful to Bob for his instruction in cycling.

My fellow graduate students were a source of inspiration and temptation at various times, in various ways. JSKI and PATCH (who visited), KARA(who skiied), Jeffers (who ran), IAIN (who climbed), Guy and Anna, GRIS, C. Camp, S. Smythe, I thank you all.

Finally, I'd like to thank Catherine Boniface who participated in all aspects of this thesis, and made it all so enjoyable.

TABLE OF CONTENTS

LIST OF TABLES

LIST OF FIGURES

CHAPTER 1

RATIONALE AND OBJECTIVES

1.1 Introduction

The net receipt of radiative energy at a site's surface, and its subsequent dissipation through the various processes operating at the surface, is of fundamental importance in determining the character of that site. These processes, the receipt of radiative energy and its subseqent dissipation, are described by the site's surface radiation and energy balances. The nature of these balances will largely determine the microclimate of the site, and will have a major impact on the hydrologic, geomorphic and biologic processes occurring there. In particular, the process of evaporation [1] is intrinsically linked with the surface radiation and energy balances. At sites where surface moisture is available, a large amount of the available radiative energy will be used to evaporate that surface moisture.

This thesis attempts to quantitatively describe the nature of the surface radiation and energy balances at an alpine tundra site during the summer. This thesis further considers the possibility of using energy balance based models both as a means of describing the effects of the alpine tundra surface on the energy balance regime, and as a means of estimating the evaporation from an alpine tundra surface.

The following sections outline the general rationale for undertaking the research, and present the specific objectives of the research.

---

[1] Throughout this thesis the term evaporation is used to describe the process by which liquid water on the surface is converted to water vapour in the atmosphere. No distinction is drawn between the types of surfaces which provide the moisture. As the alpine tundra surface will be partially vegetated, the process of transpiration, by which water moves from the interior to the exterior of the plant, is implicitly acknowledged in the measurement of evaporation from the surface. However, mechanisms other than transpiration also move moisture to the evaporating surface and the term evapotranspiration has been avoided.

1.2 Rationale

The reasons for undertaking this research were: (1) the limited knowledge about the surface radiation and energy balances in alpine tundra environments, and (2) the limited knowledge about the evaporation process in alpine tundra environments.

1.2.1 Surface Energy and Radiation Balances of Alpine Tundra

Alpine tundra has been generally defined as the biogeographic zone lying above timberline and below the elevation of the uppermost vascular plants (Löve 1970; Barry and Ives 1974; Price 1981). Alpine tundra is commonly divided into low, middle and high zones. The low alpine tundra zone having the greatest number and diversity of species, while the high zone is characterized by bare rocky ground with occasional mosses, lichens and dwarf vascular plants.

The exact areal extent of alpine tundra is difficult to specify, due to regional and latitudinal differences in timberline. However, alpine tundra represents a significant propoportion of the earth's land surface. Barry (1979) notes that over a quarter of the earth's land surface consists of mountains and high plateaus. A significant proportion of this area would include tundra. Zwinger and Willard (1972) suggest that there are over nine million square kilometres of alpine tundra in the northern hemisphere.

The climates of alpine tundras are not independent of the climates of the regions in which they exist. Consequently, alpine tundra climates are affected by variations in latitude, continentality, altitude and other regional factors. Despite regional variations, alpine tundra climates are uniformly harsh, with short growing seasons, long winters, and strong and persistent winds. Only a limited number of species are able to tolerate these conditions and tundra vegetation is more uniform in aspect and composition than any other major vegetation type (Zwinger and Willard 1972). Despite this uniformity, the alpine tundra surface often displays considerable spatial variation as vegetation responds to micro-scale variations in surficial geology, morphology, soils and climate. Micro-scale variations being loosely defined as those occurring over a horizontal scale of 0.1 m - 1 km.

Major determinants of the nature of the microclimate at an alpine tundra surface will be the amount of radiative energy available at the surface, as described by the surface radiation balance, and the nature of the partitioning of that energy, as described by the surface energy balance. Hence, one key to understanding the spatial variability of alpine tundra surfaces is knowledge of how that surface affects its radiation and energy balance.

It has long been recognized that the increase in solar irradiance associated with increasing elevation, and the nature of the alpine tundra surfaces, would result in characteristic surface radiation and energy balances for such surfaces (Geiger 1961). However, the nature of both the mountain environment and the meteorological instrumentation required for such investigations has resulted in a limited number of actual field measurements of the components of the radiation and energy balances at alpine tundra sites.

In North America there have been only a few published summer field investigations into the energy balances of alpine tundra surfaces (Gates and Janke 1966; Terjung et al. 1969; LeDrew 1975a). The state of knowledge is reportedly better in Europe (Barry 1981), although Lang (1981) observes that the energy balance studies of Turner et al. (1975) and Rott (1979) are the only studies which have been conducted over vegetated surfaces in the European Alps. In subsequent sections, some of the previous research into radiation and energy balances of alpine tundra surfaces will be reviewed.

1.2.2 Evaporation in Alpine Environments

Peattie (1936) observed, "Great and rapid evaporation is one of the most characteristic climatic conditions of high elevations". This is an opinion that is still expressed in general descriptions of alpine climates today (Price 1981). However, Slaymaker (1974) and Lang (1981) have suggested that evaporation is a relatively minor component of high alpine hydrology. These apparently disparate opinions arise from the fact that the high solar radiation loads, low humidities and high windspeeds characteristic of alpine climates result in a high potential for evaporation. Alpine environments can thus be extremely desiccating. However, despite the high potential for evaporation, water balance studies conducted in alpine environments tend to indicate that evaporation is a relatively minor component of the water balance. This refelects the general lack of available surface moisture throughout much of the year in alpine tundra environments.

On the long-term scale (annual or seasonal), evaporation may be relatively insignificant in the alpine tundra environment. On shorter time scales, particularly in the summer, evaporation becomes a much more significant component of the water balance. This temporal concern is of particular interest to the hydrological forecaster attempting to improve the accuracy and specificity of their forecasts. Furthermore, although meteorological conditions at high elevation sites may favour high rates of evaporation, the alpine surfaces affect the movement of water from the sub-surface to the atmosphere. Surface control over the movement of water to the atmosphere may be one cause of the low evaporation rates observed at some alpine locations where water balance studies have been conducted.

Evaporation (the vertical flux of latent heat) is one of the processes which dissipates the net available radiative energy at a site's surface, and is typically a major component of the surface energy balance. The surface energy balance is specific to the immediate surface, radiative energy and atmospheric conditions at the time of the investigation. Surface energy balance studies thus allow the relationship between the evaporation process and those conditions to be investigated. Hence, energy balance based studies of evaporation provide a method of looking at both short-term variations in evaporation and surface effects on the evaporation process.

Understandably, energy balance based studies of the evaporation process have largely been confined to agricultural and forest environments. They have been primarily conducted in agricultural environments, where knowledge about evaporation has more immediately apparent economic significance. On the basis of this research, several physically based models describing the process of evaporation have been developed, notably the combination model and the derivatives thereof. These models provide a physically realistic, but simplified, description of the evaporation process. In addition to their predictive value, these models also assist in the understanding of the evaporation process. The author is unaware of any attempts to apply such models to alpine tundra environments.

1.3 Objectives

The specific objectives of this research were to conduct an investigation during the summer season, at an alpine tundra site, which would;

(1) measure the components of, and describe the nature of the. surface radiation balance;

(2) measure the components of, and describe the nature of the surface energy balance. In particular the nature of the surface's influence on the evaporation process would be investigated;

(3) investigate the possibility of adapting and refining several energy balance based evaporation models for use as predictive and explanatory models in alpine tundra environments. The performance of these models for the alpine tundra surface would be evaluated against data collected in the field study.

Although the data from this investigation would be specific to the site and time of the investigation, the general information about processes gained from such an investigation should be widely applicable. A basic premise of this thesis is that micro-scale information about radiation and energy balances, and the evaporation process, in alpine environments is a prerequisite to improving the understanding of alpine hydrology on a larger scale.

1.4 Organization of the Study

The thesis is organized into six chapters. Chapter 1 provides the rationale and objectives of the study. In Chapter 2 the theroretical framework of the research is outlined. Previous research into the surface radiation and energy balances of tundra sites is reviewed. In Chapter 3 the research site, experimental methods and meteorological conditions during the experiment are described. In Chapter 4 the surface radiation balance measurements are presented and discussed. In Chapter 5 the surface energy balance measurements are presented and discussed. In addition, evaporation modelling results are presented. In Chapter 6 conclusions are drawn about the surface radiation and energy balance regimes of the research site. The performance of the evaporation models is discussed and some suggestions for future research are made.

CHAPTER 2

THEORETICAL FRAMEWORK

2.1 Introduction

This chapter commences with a general theoretical description of the nature of the radiation and energy balances of an alpine tundra surface. The theory of the techniques used to measure the components of the radiation and energy balances is also discussed. The theoretical basis of the evaporation modelling approaches considered is outlined. These modelling approaches have been previously applied to agricultural and other environments, and the discussion concentrates primarily on their theoretical applicability to the alpine tundra environment. Some of the previous research into the radiation and energy balances of tundra environments is discussed. Some of the research that has been conducted at Canadian arctic and sub-arctic tundra sites is discussed, as well as the work that has been conducted in alpine tundra environments. The similar nature of the alpine and arctic tundra surfaces would suggest that there will be similarities in their energy regimes.

A large number of symbols are introduced and defined in subsequent sections. A complete list of all the symbols used in the thesis, and their definitions, is presented in Appendix 1.

2.2 The Surface Radiation Balance

For climatological purposes, radiation can be classified into solar radiation (wavelengths smaller than 4 μm) emanating from the sun, and longwave radiation (wavelengths greater than 4 μm) originating within the earth-atmosphere system. The net amount of radiative energy at a terrestrial surface, Q^*, will be determined by the net receipt of both types of radiation at the surface, as described by the surface radiation balance

$$Q^* = K^* + L^* = (K\downarrow - K\uparrow) + (L\downarrow - L\uparrow) \qquad (2.1)$$

where K^* is the net solar radiation flux density, L^* the net longwave radiation flux density, $K\downarrow$ the global solar radiation flux density, $K\uparrow$ the reflected solar radiation flux density, $L\downarrow$ the incoming longwave radiation flux density and $L\uparrow$ the outgoing longwave radiation flux density.

2.2.1 Solar Radiation

The radiation balance is ultimately dependent on the amount of energy that the earth receives from the sun. This extraterrestrial radiation flux density, K_0, is defined as the amount of radiation incident at the top of the atmosphere on a horizontal plane of unit area. Assuming that the sun's output of solar radiation is constant, K_0 is governed by the well known geometry of the sun-earth relationship. As a result, K_0 can be estimated for any location on the earth's surface (Sellers 1965) from the following

$$K_0 = I_0 \cos Z / RV^2 \qquad (2.2)$$

where I_0, the solar constant, is currently estimated at 1368.6 W m^{-2} ±0.5% (Wilson and Hudson 1981), RV, the radius vector, is defined as the actual distance of the earth from the sun divided by the mean distance, and Z is the solar zenith angle. RV is a function of the time of year, while Z is a function of the time of day, date and latitude.

For a site with an extensive horizontal surface, where the effects of horizon shading and the slope of the receiving surface can be ignored, $K\downarrow$ will be solely determined by the effectiveness of the atmosphere above the site at transmitting K_0 to the surface. This transmissivity, *t*, is defined by

K↓/K_0. K↑ is determined by the surface reflectivity or albedo, *a*, which is defined by K↑/K↓. Thus, for sites with extensive horizontal surfaces at the same latitude and time, differences in K* will be the result of the characteristic *t* and *a* at those sites.

2.2.2 Albedo

Albedo is an intrinsic characteristic of a surface and may vary from 0.05 for water, to more than 0.80 for fresh snow. In the absence of snowcover, tundra surfaces have been observed to have albedos of between 0.15 and 0.25 (Davies 1963; Petzold and Rencz 1975; Rouse 1984). For a surface without snowcover, containing areas of bare soil and vegetation, *a* is primarily a function of the surface characteristics; soil type, soil moisture content, surface roughness, vegetation type, leaf area index, and percent ground cover (Davies and Idso 1979).

Albedo will also vary due to differences in the spectral composition of K↓ (Sellers 1965) and variations in Z (Nkemdirim 1972; Monteith 1973). The latter factor can result in substantial changes in *a* throughout the daylight period, particularly if there is a strong direct component in the solar radiation (Idso et al. 1969a; Stewart 1971; Greenland and Clothier 1975).

2.2.3 Transmissivity

The characteristically high *t* at high elevations has long been recognized. Leonardo da Vinci observed in the Alps,

> "The sun as it fell on the mountain was far brighter than
> in the plains below because a smaller extent of the atmosphere
> lay between the summit of the mountain and the sun."
>
> (Notebooks, Leonardo da Vinci, 1452 - 1519)

Much of the early mountain meteorological research focused on this aspect of alpine environments, and mountain meteorological stations were the source of much of the information used in the early research on solar radiation

(Barry 1981).

Transmissivity increases with elevation primarily as a result of the decrease in the optical air mass, M, through which incoming solar radiation must pass. For an ideal, clean, dry atmosphere (Rayleigh atmosphere)

$$M = P/P_0 \sec Z \tag{2.3}$$

where P is atmospheric pressure, and P_0 is atmospheric pressure at sea level (103 kPa, assuming a U.S. Standard Atmosphere). Hence, at an elevation equivalent to an atmospheric pressure of 75 kPa (approximately 2400 m), M will be 75% of its sea level value.

For a cloudless real-world atmosphere radiation passing through M is not only attenuated by Rayleigh scattering, but also through scattering by aerosols (Mie scattering), and absorption by aerosols, water vapour and ozone. Aerosols, water vapour and ozone are not evenly distributed throughout the vertical column of the atmosphere, either temporally or spatially. As a result, for a cloudless atmosphere, the increase in t with elevation will not be directly proportional to the decrease in M given by equation 2.3 .

Effective methods for estimating cloudless sky t, which account for the effect of attenuating agents in the atmosphere, have been developed and used (Davies et al. 1975). These approaches rely on radiosonde data, empirical approaches and/or published tables to describe the vertical distribution of the above mentioned atmospheric constituents. Alternatively, Lowry (1980) has suggested a simpler semi-empirical approach relating cloudless sky t directly to elevation/pressure.

The Lowry (1980) equation has the form

$$\ln(t) = \sec Z \ln[a + b \ln(\sec Z)] \tag{2.4}$$

where a is an empirically determined t for a given pressure (assuming $Z = 0°$), and b is an empirically determined turbidity adjustment parameter. The model also attempts to account for differences between "moist" and "dry" atmospheres.

Cloud cover greatly complicates attempts to estimate t. Davies et al. (1975) modelled hourly t using hourly cloud cover observations. They found that this data could be used to provide reliable estimates of mean K↓ for 5 – 10 day intervals. The approach was less successful for estimating K↓ over shorter time intervals. Davies and Idso (1979) suggested that improvements upon such an approach will require even more frequent and detailed cloud cover observations.

2.2.4 Outgoing Longwave Radiation

The longwave radiation flux density from a surface is given by the Stefan–Boltzmann equation

$$L\uparrow = \epsilon \ \sigma \ T_0^4 \tag{2.5}$$

where ϵ is the surface emissivity, σ the Stefan–Boltzmann constant (5.67×10^{-8} W m^{-2} K^{-4}) and T_0 the surface temperature (in Kelvin).

The emissivity of bare soils has been shown to vary with water and quartz content (Fuchs and Tanner 1968; Jackson and Idso 1975). A soil with a wet surface has the same ϵ as water (0.97). Bare soil emissivities generally fall in the range of 0.90 – 0.97. Emissivities for individual plant leaves of different species have been measured (Idso et al. 1969b), and they fall in a rather narrow range between 0.94 – 0.99. Davies and Idso (1979) suggest that for radiation studies on surfaces with complete vegetation canopies an ϵ value of 0.98 is suitable. Oke (1978) reviewed several sources and suggests that tundra surface emissivities range from 0.90 - 0.96.

Measurement of surface temperatures is done by either a contact approach or remote thermometry. The latter approach requires an infrared thermometer and knowledge of ϵ. The contact approach requires a network of temperature sensors placed directly on the surface. The contact approach has an element of uncertainty in that the temperature of the sensors may not be representative of the true surface temperature.

2.2.5 Incoming Longwave Radiation

In a similar fashion to $L\uparrow$, $L\downarrow$ is determined by the temperature and emissivity of the atmosphere. Atmospheric emissivity is variable, primarily as a result of fluctuating amounts of water vapour in the atmosphere, but also due to varying amounts of ozone, carbon dioxide and other atmospheric gases. Cloudy skies have considerably higher emissivity than clear skies. Cloud emissivities vary largely with cloud type. The depth of the atmosphere means that $L\downarrow$ at a site will be a function of the emissivity and temperature characteristics of the entire atmospheric column above the site. Due to the general decrease in atmospheric temperature and water vapour content which occur with elevation gain, $L\downarrow$ should decrease as elevation increases.

As with t, radiative transfer approaches can be used to determine $L\downarrow$ when radiosonde data are available. Alternately, several empirical approaches which use surface data to estimate atmospheric emittance have been developed (Brunt 1932; Swinbank 1963; Sellers 1965; Idso 1974; Brutsaert 1975). As with approaches for estimating t, the models for estimating atmospheric longwave emittance are greatly complicated by cloud cover.

LeDrew (1975b) showed that these empirical models must be modified for use at higher elevations. At higher elevations surface measurements are less representative of conditions in the radiatively significant part of the atmosphere, when compared to sites at or near sea level.

2.2.6 Net Longwave Radiation

The limited range of temperatures experienced in the troposphere means that L↓ and L↑ will be similar in magnitude, and that L* will be small. As atmospheric heating is primarily from the surface, L↓ tends to be smaller than L↑, so that L* is generally negative. This negativity is most pronounced during the daylight period when high K↓ values result in T_0 being greater than the atmospheric radiative temperature. At night T_0 tends to be similar to the atmospheric temperature so that L* is less negative. Cloud cover will also reduce the difference between T_0 and atmospheric temperature, as well as increasing atmospheric emissivity. As a result, increases in cloud cover will result in a less negative L*.

Elevation effects on L* are not well documented (Barry 1981). In general, both L↓ and L↑ should decrease in magnitude with increases in elevation as the mean atmospheric and surface temperatures decrease. The relative rates of decrease have not been well studied. Budyko (1974) suggests that below the snowline Q* will be constant as elevation increases, as the increase in K* will be compensated for by an increasingly negative L*. Budyko's (1974) observation is based on concurrent radiation balance studies conducted at different elevations in the Caucasus. The strong dependence of L↓ on local meteorological conditions undoubtedly results in many exceptions to this general observation.

2.3 Relationships Between Solar Radiation and Net Radiation

From the preceding discussion, it is apparent that it is theoretically feasible to estimate Q* at a specific site, at a given time, simply using knowledge about surface and atmospheric conditions at the site. Such an approach is desirable for applications such as evaporation modelling at sites where Q^* data are not available. The vast majority of alpine tundra locations fall into this category. It is also apparent that even for the simple case of a snow-free, flat and homogeneous alpine tundra site, the derivation and application of such a model would be problematic. In particular, accounting for cloud cover effects on $K\downarrow$, and the estimation of $L\downarrow$ would be difficult.

Strong empirical relationships of a simple linear form have been shown between Q^* and $K\downarrow$ (Davies 1967; Fritschen 1967; Idso et al. 1969b; Nkemdirim 1973). Given the much greater availability of $K\downarrow$ data, as compared to Q^* data, it has been suggested that for a single surface type or group of similar surface types, a single empirical expression of this type can be used to estimate Q^* for many applications (Davies and Idso 1979).

The strong relationship between $K\downarrow$ and Q^* is largely explained by the dominance of the radiation balance by the K^* or $(1 - a)\ K\downarrow$ term during the daylight period. Attempting to account for surface effects by including a or the longwave exchange coefficient suggested by Gay (1971) does not significantly improve upon these empirical relationships (Fritschen 1967; Idso 1971).

The strong empirical relationships between $K\downarrow$ and Q^* have been demonstrated for hourly, daylight period, and daily data. However, Idso et al. (1969a) noted that empirical relationships based on daylight period or daily data tend to lack data points near the origin. Hence, it may be more appropriate to use a relationship based on hourly or shorter term data to predict daylight period or daily Q^* values.

Empirical relationships between $K\downarrow$ and Q^* based on limited data sets have been shown to be surprisingly robust when used as predictors of Q^* over a wide range of latitudes and surface types (Davies 1967; Denmead 1976). The effects of elevation on such relationships has not been addressed. The theoretical change in the relative magnitudes of K^* and L^* that occurs with elevation gain might be expected to affect these empirical relationships, and reduce their applicability in alpine environments.

2.4 The Surface Energy Balance

For any vegetated surface, the energy balance can be stated as

$$Q^* + Q_{div} = Q_H + Q_E + Q_G + Q_{stor} + Q_P + Q_V \tag{2.6}$$

in which Q_{div} is the net flux density of energy resulting from the horizontal divergence of sensible and latent heat; Q_H, Q_E and Q_G are respectively the vertical flux densities of sensible, latent, and soil heat; Q_P the flux density of the net energy used for photosynthesis; Q_{stor} the flux density of the net storage of sensible and latent heat in the air over the surface; and Q_V the flux density of the net storage of sensible heat in the phytomass.

Q_{div} is the sum of the flux densities of the horizontal divergence of sensible heat Q_{Hdiv} and latent heat Q_{Ediv}. For the atmospheric layer between the surface, $z = 0$, and a reference height z_r, the divergences are given by

$$Q_{Hdiv} = \int_0^{z_r} \frac{\partial(\rho\ c_p\ u\ T)}{\partial x}\ dz \tag{2.7}$$

and

$$Q_{Ediv} = \int_0^{z_r} \frac{\partial(\rho\ \gamma^{-1}\ c_p\ u\ e)}{\partial x}\ dz \tag{2.8}$$

where x is horizontal distance, u the horizontal windspeed, T the air temperature, e the vapour pressure, c_p the specific heat of air at a constant pressure (1005 J kg^{-1} K^{-1}), ρ the density of dry air, and γ the psychrometric constant. γ is given by $\gamma = c_p\ P/\lambda\ \xi$, where λ is the latent heat of vapourization for liquid water and ξ is the ratio of the molecular weight of water to the mean molecular weight of dry air. λ is approximately 2.45 MJ kg^{-1}, varying slightly with T, and $\xi = 0.622$.

Both ρ and γ will vary with altitude due to decreases in P and T. At 2400 m asl, assuming a U.S. Standard Atmosphere (P = 75.5 kPa), ρ and γ will have values of 0.98 kg m^{-3} and 50.0 Pa K^{-1} respectively. These are the values that were used throughout this experiment.

As ρ, c_p, u and γ can be assumed to be relatively independent of x, equations 2.7 and 2.8 can be approximated by

$$Q_{Hdiv} \cong \rho \; c_p \; \bar{u} \; z_r \frac{\Delta \bar{T}}{\Delta x} \tag{2.9}$$

and

$$Q_{Ediv} \cong \frac{\rho \; c_p}{\gamma} \; \bar{u} \; z_r \frac{\Delta \bar{e}}{\Delta x} \tag{2.10}$$

in which the overbar indicates an average value for the layer between the surface and z_r.

By selecting a measurement site with an extensive area of homogeneous surface, it is often assumed in energy balance studies that Q_{div} will be negligible. Thom (1975) points out that this assumption may be more a function of the difficulty of determining Q_{div} rather than its small magnitude. Thom (1975) shows that only when windspeeds are low or when horizontal gradients of T and e are small can Q_{div} be assumed to be small.

The vertical fluxes, Q_H and Q_E, can be determined by a number of methods which are discussed in subsequent sections. Q_E is the rate at which energy is either being released from the atmosphere by the process of condensation or stored by the process of evaporation. The energy balance is thus inextricably linked to the surface hydrology of the site. A Q_E value of 680 W m^{-2} is equivalent to an evaporation rate of 1 mm $hour^{-1}$ ±2.5%.

At a specific depth, z, soil heat flux density Q_{Gz} can be measured directly with soil heat flux plates. Q_G can then be determined from the following (Hillel 1982)

$$Q_G = Q_{Gz} + C \frac{\Delta \overline{T_s}}{\Delta t} z \qquad (2.11)$$

where C is the volumetric soil heat capacity and $\frac{\Delta \overline{T_s}}{\Delta t}$ is the rate of change in the mean temperature of the soil layer between the surface and z.

For sites with extensive areas of homogeneous soils, it is reasonable to assume that an areal mean Q_G can be determined from the one dimensional expression 2.11 . In areas where soils are less homogeneous, such as alpine sites where soils are typically poorly developed and subject to congeliturbation, the factors that determine the thermal characteristics of the soil will be much more variable. This variability will cause difficulties in the determination of a mean areal Q_G. However, Q_G is typically only a small part of the overall energy balance. Published Q_G values from a wide range of sites generally range from 5% to 10% of the daily total Q^*.

Q_{stor} is the sum of the flux densities of the net storage of sensible heat Q_{Hst} and latent heat Q_{Est} in the air mass between the surface and a reference height z_r. These are given by

$$Q_{Hst} = \int_0^{z_r} \rho \, c_p \frac{\partial T}{\partial t} \, dz \qquad (2.12)$$

and

$$Q_{Est} = \int_0^{z_r} \frac{\rho\ c_p}{\gamma} \frac{\partial e}{\partial t}\ dz \tag{2.13}$$

in which $\frac{\partial T}{\partial t}$ and $\frac{\partial e}{\partial t}$ refer to the temporal rates of change of T and e respectively. Equations 2.12 and 2.13 can be approximated by

$$Q_{Hst} \cong \rho\ c_p \frac{\Delta \overline{T}}{\Delta t} \tag{2.14}$$

and

$$Q_{Est} \cong \frac{\rho\ c_p}{\gamma} \frac{\Delta \overline{e}}{\Delta t} \tag{2.15}$$

where the overbar indicates an average value for the layer between the surface and z_r. Setting z_r = 1.5 m, and assuming $\frac{\Delta \overline{T}}{\Delta t}$ = 10°C hour^{-1}, and $\frac{\Delta \overline{e}}{\Delta t}$ = 1 kPa hour^{-1} results in a Q_{Hst} of 2.95 W m^{-2} and a Q_{Est} of 5.40 W m^{-2}. The low flux densities resulting from these high rates of change for T and e show that for an air mass close to the surface, on an hourly basis, Q_{stor} is negligible.

Thom (1975) shows that for most agricultural crops both Q_V and Q_P will be very small and can be safely neglected in energy balance studies over such surfaces. For an alpine tundra surface where vegetation is areally sparse, and the biomass is very low, that assumption is especially valid.

Neglecting Q_{div}, Q_{stor}, Q_V and Q_P equation 2.6 reduces to

$$Q^* = Q_H + Q_E + Q_G \tag{2.16}$$

which, in the absence of horizontal flux divergence, will be an accurate description of the energy balance over an alpine tundra surface.

2.5 The Bowen Ratio-Energy Balance Approach

The turbulent surface boundary layer is the fully turbulent sub-layer of the atmosphere lying above the laminar airflow surface layer. By definition, within the turbulent boundary layer, the vertical flux densities of sensible and latent heat, and momentum, will be constant with height. When these fluxes are constant with height, the vertical profiles of air temperature, vapour pressure and windspeed will be logarithmic. This attribute of the turbulent surface boundary layer forms the basis of much of the following theory regarding the measurement of the vertical fluxes of sensible and latent heat.

The depth of the turbulent boundary layer at a given site is determined by the horizontal extent of homogeneous surface or fetch upwind of the site. Several rules-of-thumb for determining turbulent boundary layer depth as a function of fetch have been suggested, with height to fetch ratios ranging from 1/40 to 1/200 (Tanner 1963; Thom 1975; Brutsaert 1982).

In the turbulent surface boundary layer, the vertical flux of sensible heat can be described by

$$Q_H = - \rho \; c_p \; K_h \frac{\partial T}{\partial z} \qquad (2.17)$$

and for latent heat

$$Q_E = - \frac{\rho \; c_p}{\gamma} K_v \frac{\partial e}{\partial z} \qquad (2.18)$$

in which $\frac{\partial T}{\partial z}$ and $\frac{\partial e}{\partial z}$ are respectively the vertical gradients of temperature and vapour pressure, and K_h and K_v are respectively the transfer coefficients, or eddy diffusivities, for sensible heat and water vapour. The negative signs maintain the convention that convective fluxes away from the surface are considered positive and those towards the surface are considered negative.

K_h and K_v are transitory, varying with z and the effectiveness of the turbulent transfer process. However, it has been shown that $K_h = K_v$ under all atmospheric stability conditions (Dyer 1967; Dyer and Hicks 1970). Invoking this similarity permits the definition of the Bowen ratio, β, by combining equations 2.17 and 2.18 so that

$$\beta = \frac{Q_H}{Q_E} = \gamma \frac{\Delta T}{\Delta e} \qquad (2.19)$$

where ΔT and Δe refer to differences in T and e measured over the same vertical interval. Combining equation 2.16 with equation 2.19 permits the following expressions to be derived for Q_H and Q_E

$$Q_H = \frac{Q^* - Q_G}{1 + (1/\beta)} \qquad (2.20)$$

and

$$Q_E = \frac{Q^* - Q_G}{1 + \beta} \qquad (2.21)$$

For a site where equation 2.16 is a valid description of the energy balance, it is thus possible to determine Q_H and Q_E from multi-level measurements of T and e, when Q^* and Q_G are known. This is known as the Bowen ratio-energy balance (BREB) approach for measuring Q_H and Q_E.

2.6 The Eddy Correlation Method

In the turbulent surface boundary layer

$$Q_H = - \rho \, c_p \, [\overline{w' \, T'}] \tag{2.22}$$

and

$$Q_E = - \frac{\rho \, c_p}{\gamma} \, [\overline{w' \, e'}] \tag{2.23}$$

where w', T' and e' are respectively the instantaneous deviations from the temporal means of vertical windspeed, air temperature, and vapour pressure. $\overline{w' \, T'}$ thus denotes the time averaged product of the instantaneous covariances of w and T, and $\overline{w' \, e'}$ denotes the time averaged product of the instantaneous covariances of w and e.

To be used as a measurement technique, the eddy correlation approach requires that a large number of accurate measurements be made within the averaging period. Kanemasu et al. (1979) suggest that the sensors used should be capable of accurately responding to fluctuations of T, e and w at a frequency of at least 2 $\bar{u}/z_r$ Hz. Sophisticated instrumentation and data recording equipment are necessary to satisfy this requirement.

This approach has been used in experimental investigations of atmospheric turbulence since Swinbank (1951) first demonstrated its feasability. Recently, with the advent of commercially available sonic anemometers equipped with fast response thermocouples, and portable microprocessor based data recording systems, the approach has been more widely used as a general technique for measuring Q_H (Tanner et al. 1985). Eddy correlation instrumentation for the measurement of Q_E is much less frequently used due to the problems associated with the high frequency measurement of vapour pressure.

2.7 Ohm's Law Analog Method for Determining Sensible and Latent Heat Flux Densities

2.7.1 The Logarithmic Windspeed Profile

As noted in Section 2.5 the vertical profile of windspeed will be logarithmic in the turbulent boundary layer. This is a direct result of the nature of the turbulent exchange of momentum in the boundary layer. The aerodynamic approaches for determining Q_H and Q_E exploit this fundamental characteristic of windspeed in the turbulent boundary layer.

As an air mass moves over a surface, the transfer of momentum from the moving air mass towards the surface results in a drag force or shearing stress, τ, which is equivalent to the momentum flux density. When there are no buoyancy effects resulting from the density stratification associated with a stable or unstable atmosphere, τ can be expressed as

$$\tau = \rho \, u_*^2 \tag{2.24}$$

where u_* describes the effectiveness of the turbulent exchange process, and is referred to as eddy or friction velocity. By definition, in the turbulent boundary layer, τ will be constant with height so that u_* will also be constant with height.

For neutral stability conditions, the slope of the logarithmic windspeed profile has been experimentally shown to be related to u_* by the dimensionless von Karman's constant, k, (Brutsaert 1982), so that

$$\frac{\partial u}{\partial z} = \frac{u_*}{k\ z} \ . \qquad (2.25)$$

The value of k is generally considered to be 0.41 (Yaglom 1977).

The logarithmic windspeed profile equation, for neutral stability conditions, can thus be stated as

$$u_z = \frac{u_*}{k} \ln \frac{(z - d)}{z_0} \qquad (2.26)$$

where u_z is the windspeed at height z, z_0 is the roughness length and is defined by the criteria that $u_{z_0} = 0$, and d is the zero plane displacement height.

d is a function of vegetation height h, and is the height that z_0 is displaced above the surface by the vegetation. The value of d is typically 0.6h to 0.8h (Thom 1975). For an alpine tundra surface where vegetation cover is sparse and incomplete, the vegetation consists primarily of ground hugging mat plants, and the vegetation height does not change significantly over the growing season, it is reasonable to assume that d = 0. This is the assumption made for the remainder of this discussion.

z_0 is a measure of the aerodynamic roughness of the surface and is typically an order of magnitude less than the height of the surface roughness elements (Thom 1975). Both z_0 and u_* are intrinsic characteristics of a site's surface, and can be determined graphically from windspeed profile measurements made under neutral stability conditions.

Equation 2.25 can be generalized to be applicable in non-neutral stability conditions by introducing a dimensionless function ϕ_M. This function accounts for the effects of non-neutral stability conditions on the windspeed profile, so

$$\frac{\partial u}{\partial z} = \frac{u_*}{k\ z}\ \phi_M\ . \tag{2.27}$$

In unstable conditions ϕ_M will be greater than unity to account for the enhancement of the turbulent transfer process. In stable conditions ϕ_M will be less than unity to account for its supression. In neutral conditions ϕ_M will be equal to 1. Most appropriately ϕ_M should be empirically related to z/L, where L is the Obhukov stability length (Dyer 1974). In practice, it is possible to approximate z/L by the gradient form of the Richardson number Ri (Panofsky 1963; Thom 1975). The gradient form of the Richardson number is given by

$$Ri = \frac{g}{T}\ \frac{(T_2-T_1)\ (z_2-z_1)}{(u_2-u_1)^2} \tag{2.28}$$

where the subscripts refer to different levels of measurement, T is the mean air temperature (Kelvin) between the levels, and g is the acceleration of gravity. The calculated Ri from equation 2.28 would refer to the stability of the atmosphere between levels 1 and 2, where level 1 is closest to the surface.

Yaglom (1977) and Brutsaert (1982) have reviewed much of the work on the empirical relationship between ϕ_M and Ri, and concur with Dyer (1974) and Thom (1975), that in stable conditions, Ri ≥ 0.01,

$$\phi_M = (1 - 5\ Ri)^{-1} \tag{2.29}$$

and in unstable conditions, Ri ≤ -0.01,

$$\phi_M = (1 - 16\ Ri)^{0.25}\ . \tag{2.30}$$

The logarithmic windspeed profile equation, for the hypothetical tundra site can thus be stated as

$$u_z = \frac{u_*}{k} \ln \left(\frac{z}{z_0}\right) + \Phi_M \tag{2.31}$$

where Φ_M is the vertically integrated ϕ_M given by

$$\Phi_M = \int_{z_0}^{z} \frac{(\phi_M - 1)}{z} \, dz \, . \tag{2.32}$$

In stable conditions

$$\Phi_M = 1 - (1 - 5\ Ri)^{-1} \, . \tag{2.33}$$

For moderately unstable conditions the tabulated values of Φ_M presented by Dyer and Hicks (1970) can be approximated using the following polynomial (Kanemasu et al. 1979)

$$\ln(\Phi_M) = 0.032 + 0.048 \ln(Ri) + 0.132 [\ln(Ri)]^2 \, . \tag{2.34}$$

2.7.2 Aerodynamic Resistances and the Ohm's Law Analog

The aerodynamic resistance, r_a, to the transfer of heat or vapour from the surface through an atmospheric layer of thickness z_r is given by

$$r_a = \int_{0}^{z_r} \frac{dz}{K_{h,v} + k_{h,v}} \tag{2.35}$$

where $K_{h,v}$ is the eddy diffusivity of either heat or vapour and $k_{h,v}$ is the molecular diffusivity of either heat or vapour. The aerodynamic resistances to both heat and water vapour transfer can be assumed to be similar because; (1) as previously mentioned, it has been demonstrated that $K_h = K_v$ under all atmospheric stability conditions; and (2) the values of k_h and k_v are similar, and typically 5–6 orders of magnitude less than K_h and K_v.

By analogy with Ohm's law, the vertical flux densities of heat and vapour at height z can thus be described by

$$Q_H = - \rho \, c_p \, \frac{(T_0 - T_z)}{r_a} \tag{2.36}$$

and

$$Q_E = - \frac{\rho \, c_p}{\gamma} \, \frac{(e_0 - e_z)}{r_a} \, . \tag{2.37}$$

Similarly, the Ohm's law analog expression for the momentum flux density at height z can be stated as

$$\tau = \rho \, \frac{u_{z_0} - u_z}{r_{am}} \tag{2.38}$$

where r_{am} is the aerodynamic resistance to the transfer of momentum. Acknowledging that u_{z_0} must be 0, it follows that

$$r_{am} = \frac{(\ln(z/z_0) + \Phi_M)^2}{k^2 \, u_z} \, . \tag{2.39}$$

For an atmospheric layer with a given thickness, r_a will always be greater than r_{am}. The resistance to the transfer of heat or water vapour to or from the surface is ultimately determined by the resistance to the transfer of those properties by molecular diffusion through the laminar sub-layer of the atmosphere. Momentum on the other hand, is transferred from the moving air mass to the surface both through the process of molecular diffusion through the laminar sub-layer, and through the much more effective surface pressure forces or bluff-body effects.

Thom (1972) suggests that for vegetated surfaces which do not include large, regularly spaced, impermeable roughness elements, this bluff-body effect or excess resistance to the transfer of heat and water vapour, r_b, can be approximated by

$$r_b = 6.266 \ u_*^{-0.666} \tag{2.40}$$

where u_* is in m s^{-1}. Further, Thom (1972) suggests that this relationship will be valid over a wide range of z_0 values. Garret and Hicks (1973) and Brutsaert (1982) present both theoretical and experimental results which support this observation. The aerodynamic resistance to the vertical movement of heat or water vapour can thus be stated as

$$r_a = r_{am} + r_b = \frac{(\ln(z/z_0) + \Phi_M)^2}{k^2 \ u_z} + 6.266 \ u_*^{-0.666} \tag{2.41}$$

It is thus theoretically possible, when the surface and atmospheric parameters z_0, u_* and Φ_M are known, to use equation 2.36 to determine Q_H from measurements of T_0, T_{zr} and u_{zr}, and to use equation 2.37 to determine Q_E from measurements of e_0, e_{zr} and u_{zr}. For the remainder of the thesis, this technique of combining aerodynamic resistances and the Ohm's law analogy to determine sensible and latent heat flux densities will be referred to as the Ohm's law approach.

As a measurement technique the approach has two major weaknesses. The first is the requirement of T_0 and e_0 data. Secondly, there is the uncertainty regarding the parameterization of r_a.

As noted in Section 2.42, the measurement of T_0 can be difficult. Errors in the measurement of T_0 will result in errors in the Q_H values determined using the Ohm's law approach. The sensitivity of the approach to errors in T_0 can be determined by assuming the ρ, c_p, T_z and r_a terms in equation 2.36 are known and free of error, and differentiating the expression with respect to T_0. This shows that the magnitude of the error in Q_H, resulting from errors in T_0, will vary inversely with the square of r_a. For r_a values ranging from 10 - 100 s m^{-1}, a ±1° C error in T_0 will result in a ±0.1 - 9.9 W m^{-2} error in Q_H. For the same range of r_a values, a ±5° C error in T_0 will result in a ±0.5 - 49.3 W m^{-2} error in Q_H. Hence, errors in T_0 measurement will only result in large errors (≥50 W m^{-2}) in Q_H when the error in T_0 is ≥ ±5° C, or r_a is ≤ 10 s m^{-1}.

Measurement of e_0 is even more problematic than T_0. As a method of directly determining Q_E, the Ohm's law approach is generally restricted to situations where it can be assumed that the atmosphere at the surface is saturated, $e_0 = e_S(T_0)$. Such a situation could not be expected to persist at the surface of an alpine tundra for an extended period of time. For practical purposes, the Ohm's law approach is thus limited to the direct determination of Q_H in the summer alpine tundra environment. However, it is possible to use the approach to determine Q_E as a residual, combining equations 2.11 and 2.36 so that

$$Q_E = Q^* - Q_G - \rho \, c_p \, \frac{(T_0 - T_z)}{r_a} \, . \qquad (2.42)$$

Characteristics of the alpine tundra surface may reduce some of the uncertainty in parameterizing surface roughness and atmospheric stability, and the resultant error in Q_H, as determined using the Ohm's law approach. The lack of large roughness elements on the alpine tundra surface permits measurements of T_z and u_z to be made close to the surface. Bradley (1972) shows that when $z \leq 1.0$ m the effects of unstable or slightly stable atmosphere on the logarithmic windspeed profile equation 2.31 will be negligible. Bailey and Davies (1981a) showed that equation 2.41 for determining r_a was relatively insensitive to errors in z_0 and r_b, particularly at higher windspeeds. On the basis of these results for agricultural surfaces, the Ohm's law approach could be expected to be quite robust when applied to aerodynamically smoother alpine tundra surfaces.

2.8 Combination Model and Equilibrium Approaches for Modelling Evaporation

2.8.1 Combination Model

As the preceding discussions have shown, evaporation can be thought of as a process of vertical transportation of water vapour through eddy diffusion, where the rate of transport will be primarily determined by the difference in the water vapour content at the surface (source) and the atmosphere (sink). It can also be thought of as a process which degrades the net available energy at the surface through the conversion of some of that energy to latent heat. Combination approaches for evaporation modelling attempt to combine these two concepts to develop methods for estimating evaporation that require measurements of T, e and u at only one level.

Monteith (1965) extended the Penman (1948) combination model for potential evaporation to non-potential situations, over completely vegetated surfaces, by introducing a bulk canopy resistance term r_{st}. Monteith's (1965) model is based on the assumption that the air in a leaf's stomatal cavity is always saturated, and the temperature in the stomatal cavity is the same as the leaf's surface temperature, T_0. The bulk canopy resistance is assumed to be formed by the individual stomata resistances operating in parallel. On the basis of these assumptions

$$r_{st} = \frac{\rho\ c_p}{\gamma} \frac{e_s(T_0) - e_z}{Q_E} . \qquad (2.43)$$

Monteith's (1965) version of the combination model can be stated as

$$Q_E = \frac{S(Q^* - Q_G) + \rho\ c_p[e_s(T_z) - e_z]/r_a}{S + \gamma + \gamma(r_{st}/r_a)} \qquad (2.44)$$

where S is the slope of the saturation vapour pressure–air temperature curve at T_z.

The strength of the combination model is that only measurements of T_z, e_z and the $(Q^* - Q_G)$ term are required to determine Q_E. As discussed in preceding sections, it may be possible to approximate the value of $(Q^* - Q_G)$, with a high degree of confidence, from solar radiation measurements. The drawbacks of the combination model are its reliance on the parameterization of the resistance terms r_a and r_{st}. The approach outlined in Section 2.7.2 can be used to determine r_a for many surfaces, but the determination of r_{st} is less straight forward. Brutsaert (1982) points out that r_{st} is a function of season, soil moisture, plant species physiology, canopy morphology and other intricate and intertwined factors. He suggests that the combination model has limited practical predictive value. On the other hand, Bailey and Davies (1981a) found that for an agricultural site with a complete vegetation canopy, the combination model was relatively insensitive to errors in the estimation of r_{st}.

The assumption of a surface completely covered by a uniform vegetation canopy implicit in the combination model is not valid for the alpine tundra surface, which will include large unvegetated areas. The combination model thus has little value as a practical method for determining evaporation in the alpine tundra environment. However the model has diagnostic value. When Q_E, Q^*, Q_G, r_a, e_z and T_z are known, it is possible to use a residual approach to solve equation 2.44 for r_{st}. It should be noted that this residual technique for determining r_{st} will be sensitive to errors in the measured terms. In particular, when Q_E is small, errors in Q_E will result in large errors in the calculated r_{st}. Bailey and Davies (1981b) showed that for a completely vegetated agricultural surface (soybeans), r_{st} values determined in this fashion were comparable to measured leaf stomatal resistances. This residual approach has also been used to describe canopy resistances of a grass turf canopy (Johns et al. 1983), a prairie grassland (Ripley and Redmann 1976), a Douglas fir forest (Tan and Black 1976), and a large number of agricultural surfaces. Brutsaert (1982) suggests that this approach can also be used to describe the surface resistance of a completely non-vegetated surfaces. However, in this latter application the calculated resistance no longer describes the vegetative canopy resistance, but the resistance of the top layer of the bare soil to the transfer of water to the atmosphere.

For the partially vegetated alpine tundra surface, a general surface resistance, r_s, can be postulated. This general resistance would be determined by the net resistance of both the vegetated and non-vegetated portions of the surface to the transfer of water vapour to the atmosphere. Assuming that r_s is analagous to r_{st}, the combination model provides a method of quantitatively describing the behavior of the tundra surface with regard to the movement of water vapour to the atmosphere.

2.8.2 *Equilibrium Model*

Slatyer and McIlroy (1961) addressed the issue of adapting the Penman (1948) model to non-potential conditions by suggesting the wet-bulb depression at the surface, D_0, could be measured. The wet-bulb depression, D, is given by $T - T_W$. This resulted in

$$Q_E = \frac{S}{S + \gamma} (Q^* - Q_G) + \frac{\rho\, c_p}{r_a} (D_z - D_0) \qquad (2.45)$$

where D_z is the wet-bulb depression at a reference height z. Determination of D_0 is difficult so this model does not provide a significant practical advantage over other combination modelling approaches. Slatyer and McIlroy (1961) observed that in situations where $D_0 = D_z = 0$ or $D_0 = D_z \neq 0$, the second term of equation 2.45 becomes 0. This would occur either in situations where the air mass between the surface and the reference height z was saturated, or when the vertical T profile paralleled the T_W profile. Both situations would suggest that the overlying air mass was in equilibrium with the surface. The expression

$$Q_{eq} = \frac{S}{S + \gamma} (Q^* - Q_G) \qquad (2.46)$$

is referred to as the equilibrium evaporation model, and Q_{eq} is the latent heat flux density resulting from equilibrium evaporation.

Wilson (1971) discussed equilibrium evaporation and showed that the equilibrium situation may not persist for long periods of time. However, on a daily basis, or for longer periods of time, Q_{eq} will tend to be similar to Q_E.

Priestley and Taylor (1972) reviewed a wide range of experimental data and concluded empirically that, in the absence of advection, potential evaporation tends to be a fixed percentage of equilibrium evaporation. They proposed the following simple model

$$Q_{pe} = \alpha_{PT} \frac{S}{S + \gamma} (Q^* - Q_G) \qquad (2.47)$$

where Q_{pe} is the latent heat flux density resulting from potential evaporation, and α_{PT}, the dimensionless Priestley–Taylor coefficient, was found to be 1.26 for a wide range of diverse surfaces. A large number of subsequent investigations have confirmed that value of α_{PT} (Brutsaert 1982), although a physical explanation for the apparently constant value of α_{PT} has not been presented (Monteith 1981).

Davies and Allen (1973) suggested that for modelling actual evaporation a variable α value could be assumed. They demonstrated a strong empirical relationship between α, as defined by daily Q_E/Q_{eq}, and volumetric soil moisture, for an agricultural surface in southern Ontario. The theoretical validity of the assumption was examined by Mawdsley and Ali (1985). Mawdsley and Ali (1985) also demonstrated empirical relationships between α and several indices of soil moisture for various agricultural surfaces.

Stewart (1972), Stewart and Rouse (1976), Rouse et al. (1977) and Marsh et al. (1981) have all found that both fixed and variable α type equilibrium models can be used to model daily Q_E for high latitude tundra surfaces.

2.9 Previous Energy Balance Measurements in Alpine Tundra Environments

Barry (1981) notes that there has been a very limited number of investigations into the energy balances of alpine sites. The number of studies over snow and ice surfaces substantially outnumbers the studies conducted over vegetated surfaces.

In an early study, Gates and Janke (1966) considered the role of the vegetation component and the non-radiative fluxes in the energy balance of a vegetated alpine site. Data were collected for several summer days at Niwot Ridge, Colorado, U.S.A. (3350 m asl), and included K↓, K↑, L↓, L↑, and some windspeed, temperature and humidity measurements. Although their study was primarily concerned with the describing the radiative fluxes, an energy balance was postulated for an individual plant leaf. The role of high solar irradiances, high surface temperatures, and the importance of wind to the energy balance regime of alpine environments were all speculated upon.

Terjung et al. (1969) attempted to collect a complete set of energy balance data, using the BREB approach to measure Q_H and Q_E, for a site in the White Mountains, California, U.S.A. (3580 m asl). They collected 12 hours of data on an "exceptionally clear" mid-July day. Unfortunately they were unable to measure vapour pressure profiles successfully, and an aerodynamic approach, with no adjustment for stability effects, was used to determine Q_H and Q_E. Terjung et al. (1969) measured very high radiative flux densites. A 12 hr value for K↓ of 41.06 MJ m^{-2} was recorded. For the same period they reported that Q^* was 22.63 MJ m^{-2}, Q_H was 6.70 MJ m^{-2}, Q_E was 13.83 MJ m^{-2}, and Q_G was 2.51 MJ m^{-2}. The high Q_E values may be attributable to their site being located near a small pond.

The Terjung et al. (1969) experiment is notable as one of the first North American efforts to quantitatively describe the energy balance of an alpine environment. It illustrates some of the special characteristics of such environments, in particular high solar irradiances and surface temperatures.

Conducted almost concurrently with the work of Terjung et al. (1969) was the work done as part of the High Mountain Environment Project (HMEP) at Chitistone Pass in the Wrangell Mountains, Alaska. HMEP was a semi-autonomous research project conducted from 1966 through 1970 as part of the Icefield Ranges Research Project (Marcus 1973). Data was collected at

Chitistone Pass during the summers of 1967, 1968 and 1969.

The microclimate work at Chitistone Pass has been described by Brazel (1970), Brazel and Outcalt (1973) and Aufdemberge (1974). Brazel (1970) and Brazel and Outcalt (1973) presented some mean daily data collected in the summer of 1968. Brazel and Outcalt (1973) also presented one day of hourly data from August, 1967. In both papers an aerodynamic approach (not adjusted for stability) was used to determine the convective fluxes. Aufdemberge (1974) presented selected daily data from the summer of 1969, and compared the tundra surface energy balance of Chitistone Pass with the energy balance of a glacier site (Capps Glacier). Aufdemberge (1974) also used an aerodynamic approach to calculate the convective fluxes, but included an adjustment for stability.

The Chitistone Pass work relied heavily on manual data collection and data recording. This resulted in quite low frequencies of instrument interrogation and discontinuous data records. The rather simple approaches used to determine Q_H and Q_E at this site can be attributed to this limited data set.

The Chitistone Pass work is not commonly referred to in discussions of alpine energy balances. This may be because of the relatively low elevation of the site (1700 m asl). Certainly the low elevation, high latitude and cloudy weather at this site resulted in lower solar irradiances then have been measured at mid-latitude alpine sites.

LeDrew's (1975a) study is the most complete North American attempt to describe the energy balance of a mid-latitude alpine site. Data was collected over the summer of 1973 at Niwot Ridge, Colorado, U.S.A. The data collection program was similar to that of the Chitistone Pass work, and relied heavily on manual data collection and recording.

LeDrew (1975a) unsuccessfully attempted to use a stability corrected aerodynamic model for the estimation of Q_E. Difficulties in applying the aerodynamic approach were attributed to advection. Q_E was actually determined for the entire experiment by an empirical relationship between Q_{pe} and Q_E. The relationship was developed using Q_E data collected from a small, weighing lysimeter operated at the site during the last three weeks of the experiment.

The reported mean daily energy balance values at the Niwot Ridge site for the period June 25 - August 24, 1973 were Q^* of 12.48 MJ m^{-2}, Q_H of 6.20 MJ m^{-2}, Q_E of 4.73 MJ m^{-2}, and Q_G of 1.55 MJ m^{-2}.

The most sophisticated alpine energy balance results that have appeared in English language journals appear to be those of Staudinger and Rott (1981). They presented data collected during the summers of 1977 and 1978 at two sites in the Austrian Alps, a cultivated pasture at 1960 m asl, and a flat topped ridge at 2580 m asl. Through the use of automated data recording and sensor interrogation, data was collected far more frequently than in the previously discussed studies.

The BREB approach was used to determine Q_H and Q_E at both sites. A lysimeter was operated at the high elevation site for 6 weeks during the summer of 1978. Notably, the Q_E values from the lysimeter were some 20% higher than the values from the BREB approach. For both sites Q_E was consistently the dominant term in the energy balance.

Staudinger and Rott (1981) used the collected data to investigate the effects of atmospheric stability on the convective transfer process at their sites, and investigated relationships between the Φ_M function and Ri.

The very broad similarities between alpine and arctic tundras are well documented. There have been a number of studies of energy balances of arctic tundra surfaces, some of which are summarized by Lewis and Callaghan

(1976). A considerable amount of work on the microclimates of Canadian arctic tundra sites has been published, eg., Addison and Bliss (1980), Ohmura (1982) and Rouse (1984). LeDrew and Weller (1978) have presented a direct comparison of the Niwot Ridge experiment data, with data collected at Barrow, Alaska. This paper illustrates that, although the surfaces are similar, latitudinal differences result in the energy regimes of the sites being extremely different.

CHAPTER 3

EXPERIMENTAL PROCEDURE

3.1 Introduction

The field measurements for this investigation were made at a site on Plateau Mountain which is located in the Livingstone Range of the Rocky Mountains in southwestern Alberta, Canada, at about 50° 15′ N and 114° 31′ W. A map showing the the location of Plateau Mountain is presented in Figure 3.1.

This chapter describes the characteristics of the site, the field techniques used and summarizes the general meteorological conditions experienced during the investigation.

3.2 Site Description

The summit topography of Plateau Mountain is characterized by extensive areas of flat to gently rolling terrain lying well above treeline. The summit surface has been described as a fellfield (Bryant and Scheinberg 1970), and is underlain by relic permafrost (Harris and Brown 1978). Much of the surface exhibits a wide range of periglacial patterned ground structures, including sorted and non-sorted polygons and nets (Bryant and Scheinberg 1970; Harris and Brown 1978).

The instrumentation site was located in the summit area, at an elevation of about 2475 m asl. The site has a slight northwest aspect. The average slope of a 200 m transect running from SE to NW through the middle of the site is approximately 3% . An elevated gravel surface road runs north and south 100 m to the west of the instrumentation site. The slope becomes east facing 125 m to the east of the instrumentation site, and 235 m to the east of the site the mountain falls away in steep cliffs.

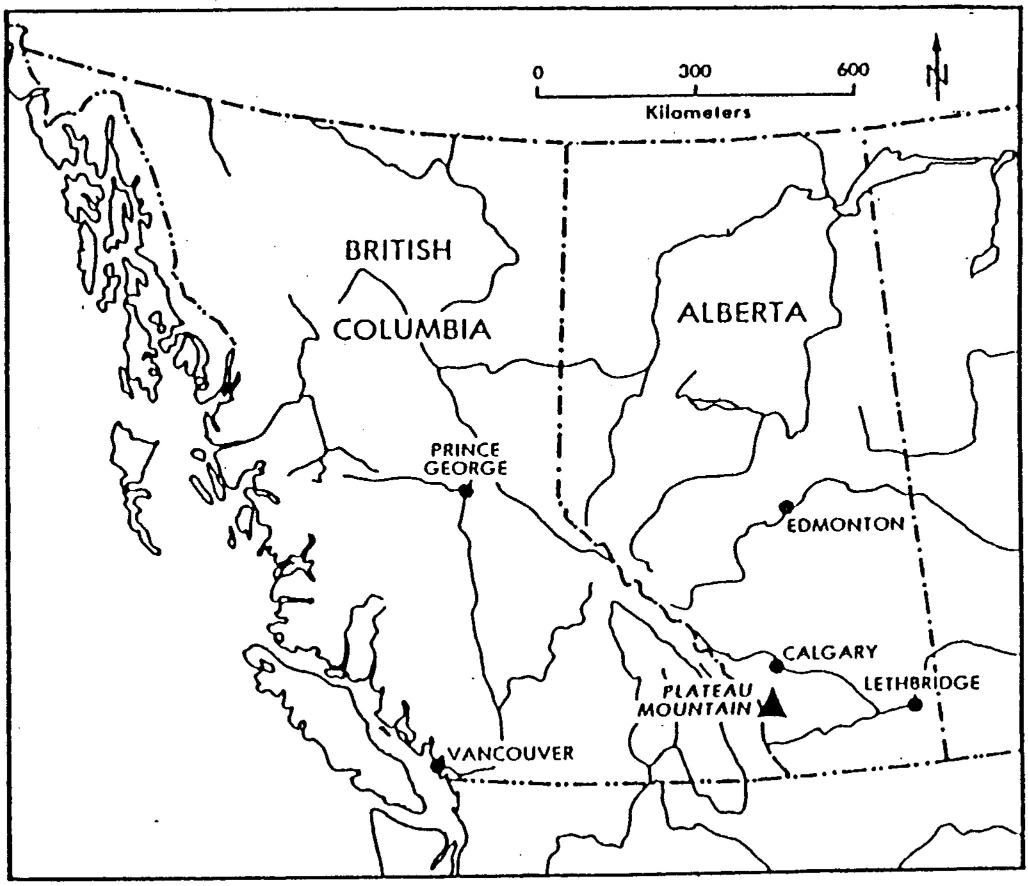

Figure 3.1. Map showing location of Plateau Mountain.

There was evidence of water draining from the higher areas southeast of the site, to a low area west of the site and adjacent to the road enbankment. Water was not observed flowing in open channels towards this low area, but a puddle would form adjacent to the road enbankment after larger precipitation events. Small puddles of standing water were observed in depressions in the drainage area after precipitation events, and during the initial stages of the study.

In the area of instrumentation, the surface was dominated by frost mounds or frost hummocks 2 - 4 m in diameter. The tops of the hummocks were generally covered with bare gravel and lichens. The sides of the hummocks were partially covered with mat forming species, primarily *Dryas hookeriana*, *Silene aucolis* and *Salix nivalis*. The mat forming species were often encroaching on to the summits of the mounds. The low lying areas between the hummocks had developed more of a turf, dominated by various species of *Carex*, *Saxifraga*, *Potentilla* and grasses. Figure 3.2 shows a typical hummock in the vicinity of the site. A similar surface type was found immediately north, west and east of the instrumentation. To the south of the instrumentation there were slightly less areas of bare soil, rock and mat forming species, and more areas of turf. Figure 3.3 shows the site as viewed from approximately 100 m to the south. In Figure 3.3, a Stevenson screen and a temporary shelter erected for the data recording equipment are visible on the horizon.

Bryant and Scheinberg (1970) described similar vegetation types in association with the frost hummocks at Plateau Mountain. They considered the difference between the vegetation found on the hummocks, and the vegetation found between the hummocks to be a function of both succession and microclimate. The vegetation types at the experiment site are characteristic of those found on windswept ridges, with well drained soils, and small amounts of snow accumulation in the middle and upper alpine zones of this part of the Rocky Mountains (Ogilvie 1976; Holland and Cohen 1982).

Figure 3.2. Photograph of typical frost hummock in the instrumentation area.

Figure 3.3. Photograph showing instrumentation site as viewed from 100 m to the south.

About 100 m due east of the instrumentation the surface exhibited increasing numbers of stone rings. The same transition occurred several hundred metres to the north and south, and on the west side of the road. The gravel road and the stone rings represented significant discontinuites in the surface homogeneity, and were considered to be the fetch boundaries.

Allowing for the discussed micro-scale variations in vegetation, it would be reasonable to assume that the surface was homogeneous in terms of vegetation and aerodynamic roughness for at least 100 m to the east and west of the instrumentation, and for several hundred metres to the north and south. Assuming a height to fetch ratio of 1/100 (Thom 1975), measurements taken at heights above the surface of 1 m or less would have been within the turbulent boundary layer, irrespective of the wind direction. The prevailing winds were from the southwest during the investigation, and in that direction there were several hundred metres of fetch.

3.3 Experimental Procedure

3.3.1 Measurement of Radiative Flux Densities

$K\downarrow$ was measured with an Eppley PSP pyranometer mounted on a tripod 1.5 m above the surface. $K\uparrow$ was measured with an inverted Middleton CN7 Solarimeter mounted on a horizontal arm projecting 1 m from the tripod. A side by side 24 hour intercomparison of the Middleton and Eppley pyranometers was carried out in the field at the end of the experiment. The sensors were found to agree within 0.1% of each other. This level of agreement was confirmed by the calibrations done by the Atmospheric Radiation Centre, Atmospheric Environment Service, at the end of the experiment.

Two Middleton CN-1 pyrradiometers were mounted on the same tripod as the pyranometers. One pyrradiometer measured Q^* directly. The lower hemisphere of the other pyrradiometer was covered with a blackbody cavity.

The temperature of the blackbody cavity was measured with a thermocouple junction referenced to an Omega cold junction compensator. This instrument provided data for the determination of the incoming all-wave radiation flux density, $Q\downarrow$. The tripod and attached radiation sensors are shown in Figure 3.4.

Using the measured Q^*, $K\downarrow$ and $K\uparrow$ values it is possible to determine L^* from simple algebraic manipulation of the radiation balance equation (equation 2.1). It is worthwhile to acknowledge that the errors in all three measured terms are accumulated in the calculated L^*. Two approaches could then be used for partitioning L^* into $L\downarrow$ and $L\uparrow$.

The first approach involves calculating $L\uparrow$ from the measured T_0 using the Stefan-Boltzmann expression (equation 2.5). For this experiment ϵ was estimated at 0.90. The measurement of T_0 is discussed in a subsequent section. $L\downarrow$ can then be simply calculated by adding $L\uparrow$ to the calculated L^*.

The second approach involves using the $Q\downarrow$ value from the blackbody cavity equipped Middleton pyrradiometer. $L\downarrow$ can then be determined from

$$L\downarrow = Q\downarrow - K\downarrow \tag{3.1}$$

and $L\uparrow$ can be calculated by residual. This second approach has the advantage that $L\uparrow$ and $L\downarrow$ are calculated from more independent expressions, which reduces the accumulating errors. The second method also provides a non-contact approach for determining radiative surface temperatures. Unfortunately, post-experiment analysis of the $Q\downarrow$ data revealed that a nonsystematic sensor error, most likely associated with the measurement of the temperature of the blackbody cavity, had occurred. Others have reported similar problems with this type of sensor (Enz et. al. 1975; Rouse 1984). The failure of the $Q\downarrow$ sensor, and the large accumulating error associated with the approach used to determine the longwave fluxes reduced the quality of the longwave radiation flux density data collected during this experiment.

Errors associated with the determination of each term of the radiation balance are are presented and discussed in Appendix 2.

All the radiation sensors were calibrated by the Atmospheric Radiation Centre, Atmospheric Environment Service, at the end of the experiment. Radiative fluxes for all the radiation sensors were calculated using the calibrations provided by the Atmospheric Radiation Centre.

Daily and daylight period radiation totals were calculated by summing the appropriate half-hourly flux densities. Daily and daylight mean t and a were calculated using the mean daily and daylight values of K_0, $K\uparrow$ and $K\downarrow$.

3.3.2 Measurement of Vertical Profiles of Air Temperature and Vapour Pressure

Measurements of T and T_W were made at four separate levels above the surface using a differential psychrometer system which was operated continuously for the period of the experiment. Similar systems have been described by Pruitt and Lourence (1969), Davies and Allen (1973), Rouse et al. (1977), and Bailey and Davies (1981b). Measurements were initially made at 0.25 m, 0.50 m, 1.0 m and 1.5 m above the surface. This spacing was changed on the afternoon of July 4 to 0.25 m, 0.50 m, 0.75 m and 1.0 m above the surface, as vertical vapour pressure gradients became quite low at heights above 1.0 m as the experiment progressed. The differential psychrometer system is shown in Figure 3.5.

Differences in T between levels 1-2, 2-3, and 3-4 were measured with thermopiles constructed of 0.51 mm diameter copper-constantan wire. The junctions were housed in 4 mm diameter, 350 mm long, stainless steel tubing. The thermopile junctions were approximately 1 mm from the end of the tubing. The tubing was filled with polyester resin, after the thermopiles were threaded into the tubing, to provide rigidity and strength. Differences in T_W

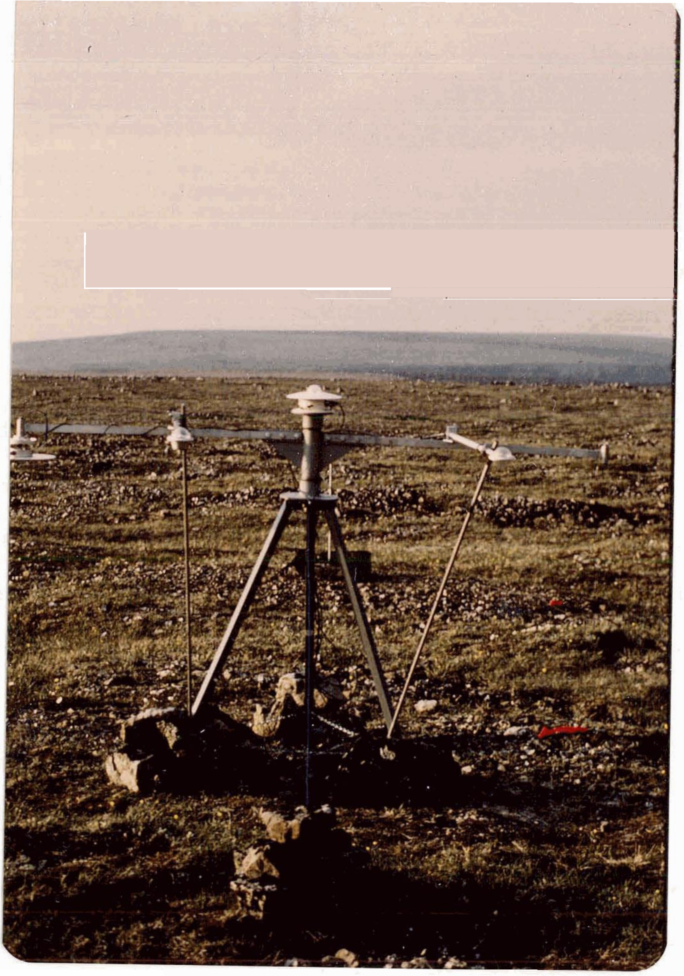

Figure 3.4. Photograph of tripod with attached pyranometers and pyrradiometers.

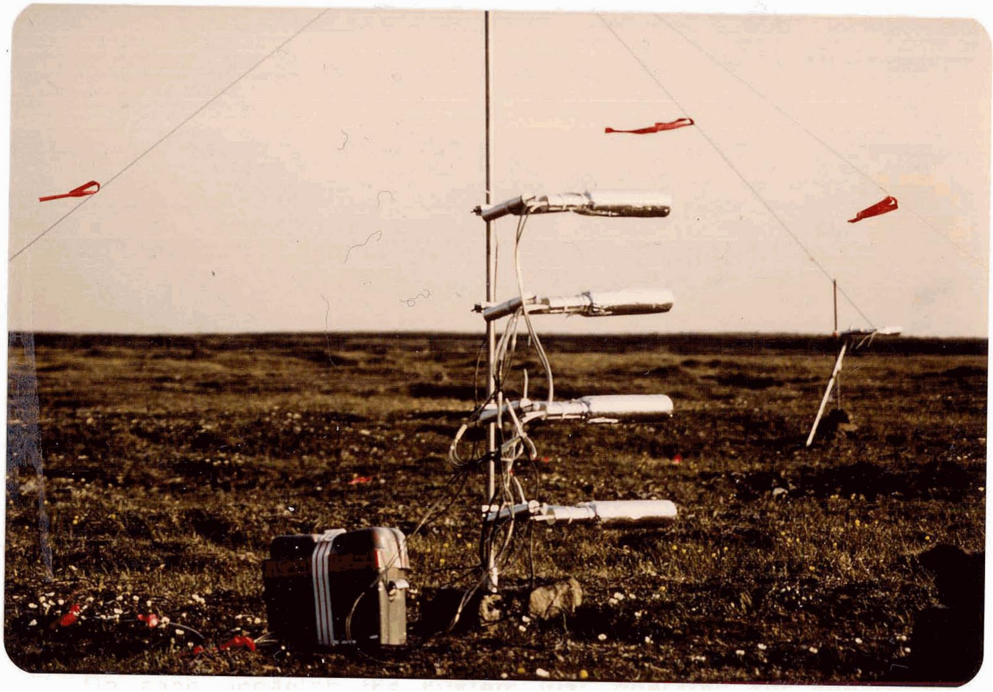

Figure 3.5. Photograph of four level differential psychrometer system.

were measured using identical thermopiles housed in 4 mm diameter, 250 mm long, stainless steel tubing. The extra length of the T sensors allowed them to be bent slightly, so that the T thermopile was in alignment with the T_W thermopile. The T_W sensor was covered with tightly stretched cotton wicking which was kept moist by a capillary fed supply of distilled water. The non-sensing ends of the tubes containing the T and T_W thermopiles were mounted in a circular block of acryllic plastic 35 mm in diameter and 65 mm long. The stainless steel tubing was fed through 2 holes drilled approximately 10 mm apart near the centre of the plastic block. The plastic block was mounted in a plastic "T" type pipe fitting in which the aspiration fan was housed, and to which the hardware for attaching the sensor to its vertical stand was fixed.

The sensors were shielded by an inner shield of 30 mm diameter plastic pipe, 235 mm in length. An outer shield, 45 mm in diameter and 275 mm in length, constructed from 15 mm thick open cell foam, was placed over the inner shield. A 7.5 mm air space separated the two shields. Aspiration was provided by a Micronel 12V DC fan mounted so as to draw air in along the inner shield, at a rate exceeding 3 m s^{-1}. Reflective silver mylar tape was placed on the shields and mounting hardware to minimize radiative heating.

Absolute T and T_W were measured at the lowest level using single junction thermocouples. T and T_W at each level were then determined by adding the measured temperature differences between levels, to the measured absolute temperatures.

Side by side intercomparisons of the sensors in the laboratory show that the system is capable of resolving temperature differences between levels to witnin ±0.05°C . This observed degree of resolution agrees well with the results of the error analysis presented in Appendix 2.

Wicking was replaced on the T_W sensors on two occasions, July 2 and July 11. On each occasion the system was operated for several hours without wicking to compare the T and T_w sensors at each level. Similar intercomparisons were conducted at the beginning and end of the experiment. The results from these intercomparisons supported the laboratory estimation of the resolution of the system.

Vapour pressure at each level was calculated from the psychrometric equation

$$e = e_s(T_w) - \gamma(T - T_w) \qquad (3.2)$$

where $e_s(T_w)$ is the saturation vapour pressure at T_w. $e_s(T_w)$ was determined from the following well known expression (Murray, 1967)

$$e_s(T_w) = X * \exp \frac{Y * T_w}{T_w + V} \qquad (3.3)$$

where X,Y and V are empirically determined constants.

3.3.3 Determination of Sensible and Latent Heat Flux Densities Using the BREB Approach

The 4 level differential psychrometer system provided six different combinations of $\Delta T/\Delta e$ for the calculation of β using equation 2.24. They are determined from the differences in T and e between levels 1-2, 2-3, 3-4, 1-3, 2-4 and 1-4, where level 1 is the level closest to the surface. Theoretically, all 6 values should be the same for measurements made within the turbulent boundary layer. However, limitations in instrumentation and measurement capabilities can result in differing values. These difficulties are exacerbated in dry climates where Δe tends to be small and ΔT tends to be quite large.

β was initially determined using a linear regression approach to fit a straight line through the 6 ΔT-Δe pairs measured in each half-hour period. The slope of the line was then considered to be the best estimate of $\Delta T/\Delta e$ for that period.

A tendency for a bi-modal distribution of ΔT-Δe pairs to develop in the afternoon was noted. The $\Delta T/\Delta e$ values based on the differences between levels 1-2, 1-3 and 1-4 being significantly different than those based on the differences between levels 2-3, 2-4 and 3-4. The consistent occurrence of the bi-modal distribution in the afternoons suggests that level 1 was too close to the surface, and may also have been experiencing radiative heating errors. The problems with the data from level 1 caused all data from that level to be rejected. β was determined using the linear regression approach, and the T and e measurements made at levels 2, 3 and 4.

The transition periods between night and day pose problems for the use of a regression technique for determining β. During these periods, the vertical gradients of T and e become very small as the normal nocturnal temperature inversion develops and ends. For this experiment the transition periods were dealt with by using interpolation to estimate Q_H and Q_E. The low Q^* values that occur in these periods, and their short duration (2 - 3 hrs) limit the impact of this estimation approach on the calculated daily totals of Q_E and Q_H.

Daily and daylight period values of the energy balance components were calculated by summing the appropriate half-hour flux densities.

Errors associated with the determination of Q_H and Q_E using the BREB approach are presented and discussed in Appendix 2.

3.3.4 Measurement of Horizontal Differences in Air Temperature and Vapour Pressure

A single level system designed to measure differences in T and e, at one level, over a horizontal distance of approximately 15 m, was operated continuously for the period of the experiment.

Two sensors identical to the sensors used at each level of the differential psychrometer were constructed. The thermopiles used to measure differences in T and T_w between the two sensors were separated by 20 m of copper-constantan wire. The sensor nearest the data loggers (sensor A) was set at a fixed location, and was equipped with 2 single junction thermocouples for the measurement of absolute T and T_w. T and T_w at the far sensor (sensor B) were then determined by adding the measured differences in temperature between the sensors, to the absolute temperatures measured at sensor A. Vapour pressure at each sensor was determined using the equation 3.2. Sensor B was moved between 4 fixed locations, all of which were approximately 15 m from Sensor A. By moving sensor B it was possible to keep sensors A and B in approximate alignment with the direction of the prevailing wind. Both sensors were initially operated at 1.0 m above the surface, and lowered to 0.75 m above the surface on July 6.

Assuming that the profiles of T and e at sensor A were parallel to the profiles at sensor B, this system would provide the necessary $\frac{\Delta\bar{T}}{\Delta x}$ and $\frac{\Delta\bar{e}}{\Delta x}$ to determine Q_{Hdiv} and Q_{Ediv} from equations 2.9 and 2.10.

The data from the system used to measure the horizontal differences of T and e did not support a detailed determination of horizontal flux divergence. This was primarily due to problems in aligning the system with the wind direction, micro-scale relief in the area of the instrumentation and the resolution of the system. However, the data can be used to provide an approximation of the probable maximum amount of horizontal flux divergence.

For the period of the experiment the ΔT and Δe measurements, made at a height of 1 m above the surface, over the horizontal distance of 15 m generally fell within the resolution limits of the measuring system. The absolute values of Δe were generally less than 15 Pa, and the absolute values of ΔT were generally less than 0.05 °C. Assuming the system to be perfectly aligned with the wind direction, and a mean windspeed ($\bar{u}$) for the interval between the surface and z_r of 4 m s^{-1}, these ΔT and Δe values would result in a total horizontal flux divergence of ±100 W m^{-2} . A $\bar{u}$ value of 4 m s^{-1} over the interval between the surface and z_r would result in a u value at z_r of approximately 6 - 7 m s^{-1}. As u at 1 m was generally less then 6 m s^{-1} the value of ±100 W m^{-2} can be taken as an approximate upper bound to horizontal flux divergence. Actual horizontal flux divergenge values of ± 50 - 60 W m^{-2} seem quite probable, and are accepted as part of the measurement error associated with the BREB approach.

3.3.5 Eddy Correlation Measurement of the Sensible Heat Flux

A Campbell Scientific CA27T sonic anemometer equipped with a 0.0127 mm diameter chromel-constantan thermocouple junction was used to measure vertical windspeeds and air temperatures. The sonic anemometer and thermocouple were sampled at a rate of 10 Hz, and $\bar{w}$ and $\bar{T}$ were calculated at 5 minute intervals. All signal processing was done using a Campbell Scientific CR7 data logger system.

The measurements were initially made at 1.0 m above the surface, and on the afternoon of July 6 the sensor was lowered to 0.75 m above the surface.

The fragile nature of the thermocouple and the possibility of moisture damage to the sonic anemometer prevented the operation of the CA27T for the whole period of the experiment. Approximately 140 hours of data were collected using this system. Figure 3.6 shows the sonic anemometer with thermocouple.

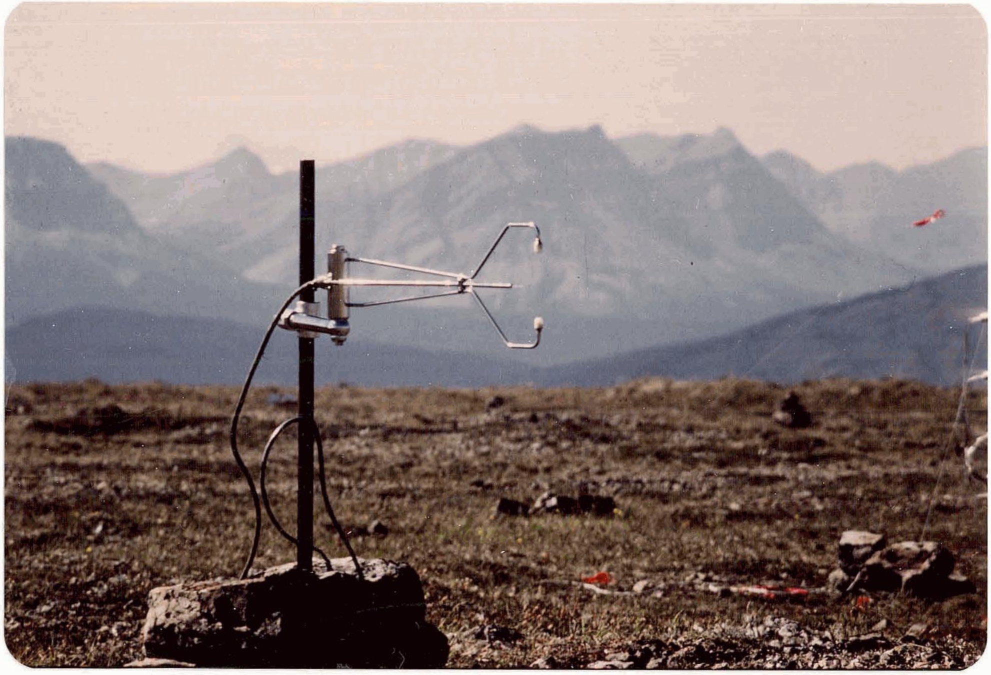

Figure 3.6. Photograph of CA27T sonic anemometer with thermocouple.

Figure 3.7. Photograph of single thermocouple junction of surface temperature array. Pencil pointing to thermocouple junction indicates scale.

3.3.6 Determination of Surface Aerodynamic Characteristics and Measurements of Stability, Windspeed and Wind Direction

Windspeed profiles were measured for portions of 16 separate days during the experiment. A cup anemometer system (Rimco) designed by Bradley (1969) was used. This system requires an attendant and could not be operated continuously for the period of the experiment. A total of 108 hours of windspeed profile data were collected. Windspeeds were measured at 4 separate levels for half-hour averaging periods. The levels were set at the same height above the surface as the differential psychrometer sensors.

Thirty five of the half-hourly vertical windspeed profile measurements were made in conditions which satisfied the neutrality requirement of $Ri \leq |0.01|$. Typically these neutral cases occurred in the early morning, evening or during periods of high windspeeds. The mean z_0 value determined from the neutral profiles was 2.1 mm. The maximum and minimum z_0 values were 0.1 mm and 5.8 mm respectively, and the standard deviation was 1.4 mm. The 2.1 mm value indicates that the aerodynamic surface roughness at Plateau Mountain was between that of a bare soil surface and a short grass surface (Monteith 1973; Thom 1975; Kanemasu et al. 1979).

As multi-level windspeed measurements were not available for the entire period of the experiment, a modified form of equation 2.28 was used to determine Ri. The modified equation makes the assumption that T_0 describes the air temperature at z_0, so that

$$Ri = \frac{g}{T} \frac{(T_z - T_0)\ (z - z_0)}{(u_z - u_{z_0})^2} \qquad (3.4)$$

where T is the mean temperature between the surface and reference height. Ri values calculated from equation 3.4 showed good agreement with concurrent values calculated using equation 2.28, and the vertical windspeed profile data.

A Met One anemometer and wind vane were operated continuously for the period of the experiment. Both instruments were mounted 1 m above the surface. The Met One anemometer windspeed measurements were in excellent agreement with the concurrent measurements made at the 1 m level by the Bradley-Rimco system.

3.3.7 Soil Sampling and Analysis

Six soil samples were taken every two days. Sampling procedure consisted of digging a small trench in the surface, pressing a sharp edged 50 mm deep sampling tin into the surface, then removing the tin, using a trowel inserted horizontally from the trench to retain the sample in the tin. Samples were taken from the 0-50 mm layer and the 50-100 mm layer. The amount of disturbance to the sample was assessed at the the time of sampling, and samples considered to be good for bulk density analysis were noted. Observations were also made of the general location of the sample and surface vegetation at the sample location. Of the 120 samples taken, 61 were assessed to be good for bulk density analysis, 38 of those were from the 0-50 mm layer and 23 were from the 50-100 mm layer. Sample tins were sealed with tape and mailed to Simon Fraser University. There they were weighed, oven dried for 24 hours at 105°C, and then reweighed.

After weighing, drying and reweighing, 38 of the 61 soil samples judged good for bulk density analysis in the field were passed through a 2 mm sieve. The fraction from each sample with a diameter of greater than 2 mm was weighed and its volume determined by water displacement. Bulk density ρ_b was then calculated, correcting for the greater than 2 mm diameter fraction (McKeague 1972). Loss on ignition (LOI) analysis (Ball 1964; McKeague 1972) was performed on 24 of the 38 sieved samples. Results from these analyses are presented in Table 3.1.

Table 3.1. Summary of soils analysis results for samples taken at Plateau Mountain, June 26 - July 26, 1985.

	Units	All Samples	0-50 mm Samples	50-100 mm Samples
<u>Oven Drying Results</u>				
# of cases		120	60	60
weight of H_2O in sample				
mean	g	41.8	40.5	43.2
std. dev.	g	31.9	28.8	34.9
<u>Sieving Results</u>				
# of cases		38	25	13
weight of >2 mm fraction				
mean	g	69.2	39.7	126.1
std. dev.	g	68.7	46.5	70.0
volume of >2 mm fraction				
mean	10^3 mm^3	30.4	17.4	55.2
std. dev.	10^3 mm^3	30.1	20.8	30.2
density of >2 mm fraction				
mean	10^3 kg m^{-3}	2.3	2.3	2.2
std. dev.	10^3 kg m^{-3}	0.41	0.38	0.44
weight of ≤2 mm fraction				
mean	g	46.8	44.4	51.4
std. dev.	g	17.8	19.2	14.3
volume of ≤2 mm fraction				
mean	10^3 mm^3	198.1	207.6	179.8
std. dev.	10^3 mm^3	32.2	29.4	30.2
bulk density				
mean	10^3 kg m^{-3}	0.25	0.23	0.30
std. dev.	10^3 kg m^{-3}	0.15	0.17	0.10
$\frac{\text{>2 mm weight}}{\text{dry bulk weight}}$				
mean		0.417	0.325	0.580
std. dev.		0.308	0.285	0.287

(Table 3.1 continued)

	Units	All Samples	0-50 mm Samples	50-100 mm Samples
LOI Analysis Results				
# of cases		24	14	10
weight of organic fraction				
mean	g	16.6	18.7	13.5
std. dev.	g	7.9	7.3	8.1
organic weight / dry bulk weight				
mean		0.233	0.303	0.135
std. dev.		0.193	0.191	0.155

The high standard deviations for the ratio of $\frac{\text{>2 mm weight}}{\text{dry bulk weight}}$ and the ratio of $\frac{\text{organic weight}}{\text{dry bulk weight}}$ for the samples from the 0–50 mm layer illustrate the highly variable nature of the alpine soils at Plateau Mountain. Bryant and Scheinberg (1970) found similar variability. The extremely low bulk densities are considered to be a function of both the high porosity of the soils, and the difficulty of sampling soils with such a large gravel fraction.

A linear regression was performed between the organic and dry bulk weights of the 14 samples from the 0–50 mm layer for which LOI analysis was done. The slope of this regression line was considered to be the best estimate of the ratio of organic weight to dry bulk weight for the 60 samples from the 0–50 mm layer. There was not a strong relationship between the organic and dry bulk weights of the 14 samples. This would be expected from the high standard deviations already discussed. However, it was felt that this approach provided as adequate an estimate of the average ratio of organic weight to dry bulk weight, as using the means of the 14 samples would have done, and was less susceptible to the effects of outliers. On the basis of this ratio, the average weight of organic matter for all the samples from the 0–50 mm layer was estimated as 15.1 g, and the average weight of mineral matter as 73.3 g.

To calculate the volumetric fraction of organic material, X_o, and the volumetric fraction of mineral material, X_m, in the soils an average density of 1.3×10^3 kg m^{-3} was assumed for the organic material (Hillel 1982), and the average measured density of the greater than 2 mm fraction, 2.3×10^3 kg m^{-3}, was assumed for the mineral matter. On the basis of these assumptions the average X_o for the 0–50 mm layer was calculated to be 5.4%, and X_m was calculated to be 15.5% .

The volumetric fraction of water in the soil, X_w, can be measured by a variety of techniques (Schmugge et al. 1980; Hillel 1982; Munro 1982). For this experiment X_w was calculated from

$$X_w = (M_w \frac{\rho_w}{\text{sample volume}})\ 100\% \qquad (3.5)$$

with M_w being the mass of water in the sample, as determined by the difference between the fresh and oven dried soil sample weights, and ρ_w the density of water. Munro (1982) suggests that this approach is less sensitive to sampling errors when compared to other gravimetric techniques. For days on which no soil samples were taken X_w was estimated by interpolation.

3.3.8 Measurement of Soil Heat Flux Density, Soil Temperature and Surface Temperature

The soil heat flux density at the surface was determined from equation 2.11. Soil heat flux density at 50 mm below the surface was measured continuously using three Thornthwaite soil heat flux disks connected in series. Mean soil temperature in the 0-50 mm layer was measured using 2 arrays of 5 single junction thermocouples housed in 2 mm diameter stainless steel tubing. The thermocouples were placed at 10, 20, 30, 40 and 50 mm below the surface at 2 separate locations near the soil heat flux plates. The two arrays were connected in parallel.

The volumetric heat capacity of the soil, C, can be calculated by summing the volumetric heat capacities of the constituents of the soil weighted according to their volume fractions (Hillel 1982), so

$$C = \Sigma\ X_s C_s + X_w C_w + X_a C_a\ , \qquad (3.6)$$

where X_s, X_w and X_a are the volumetric fractions of solids, water and air in the soil and C_s, C_w and C_a are their volumetric heat capacities. The solid fraction includes various types of minerals and organics, and Σ indicates the summation of the respective heat capacities of the solid fractions, weighted by their volumes. Equation 3.6 can be simplified by assuming average heat capacities for minerals, C_m, and organics, C_o, of 2.0 MJ m^{-3} K^{-1} and 2.5 MJ m^{-3} K^{-1} respectively. C_a is 3 orders of magnitude less than the heat capacity of the other soil constituents (Ca = 0.0012 MJ m^{-3} K^{-1}), and its contribution to the overall heat capacity is neglegible (Hillel, 1982). As a result equation 3.6 can be restated as

$$C = 2.0\ X_m + 2.5\ X_o + 4.2\ X_w\ (\mathrm{MJ\ m^{-3}\ K^{-1}})\ . \tag{3.7}$$

As X_m and X_o will be relatively constant for a given soil type, C will primarily vary with X_w.

Substituting the calculated X_m and X_o values discussed in Section 3.3.7 into equation 3.6 resulted in the following expression for determining the volumetric heat capacity of the 0–50 mm soil layer at the study site

$$C = 0.427\ \mathrm{MJ\ m^{-3}\ K^{-1}} + (X_w\ 4.19\ \mathrm{MJ\ m^{-3}\ K^{-1}}). \tag{3.8}$$

Low values of X_w (0 - 5%) substituted into equation 3.8 yield volumetric soil heat capacity values of 0.4 - 0.6 MJ m^{-3} K^{-1}. Published volumetric heat capacities (Geiger 1961; Oke 1978; Hillel 1982) for other dry, porous soils also fall into this range.

Surface temperature, T_0, was measured with 2 arrays of 4 single junction thermocouples constructed of 0.127 mm diameter copper–constantan wire. Each junction was affixed to the surface using a staple approximately 25 mm back from the junction. Figure 3.7 shows a single junction from one array. The arrays were staked out in 1 m^2 plots and wired in parallel to provide the average surface temperature in those plots.

In additon to the measurements necessary to determine Q_G and T_0, measurements were also made of the vertical temperature profile of the soil. Thermocouple junctions were placed at 0.01, 0.10, 0.25, 0.50 and 0.75 m below the surface to measure the soil temperature profile.

3.3.9 Data Recording

Three Campbell Scientific data loggers were used, a CR21, 21X, and CR7, to record and process the data generated by the Met One anemometer and windvane, radiation instrumentation, and thermocouple based sensors. The data loggers were all programmed to determine half-hour averages. In the case of sensors which generated continuous analog signals, the data loggers were programmed to interrogate the sensors on 10 second intervals. The data loggers were placed in environmental enclosures, which in turn were placed in a temporary 1 m x 1 m x 1.5 m shelter that was erected at the site. Figure 3.8 shows the data logger installation.

3.3.10 Meteorological Data Collection

There is a limited number of permanent stations collecting meteorological data in the vicinity of Plateau Mountain. In the immediate area are two Alberta Forest Service fire lookouts, Raspberry Ridge at 50° 18′ N, 114° 31′ W and 2362 m asl, and Hailstone Butte at 50° 10′ N, 114° 27′ W and 2373 m a.s.l, where meteorological observations are made twice daily during the summer. The Alberta Forest Service also operates a year round station at Kananaskis at 51° 02′ N, 115° 03′ W and 1380 m asl. The nearest Atmospheric Environment Service synoptic stations are at Banff, Calgary and Lethbridge. Data from all the above stations are published by the Atmospheric Environment Service.

At the Plateau Mountain instrumentation site, a Stevenson screen with its base 1 m above the surface was erected. The screen contained maximum, minimum and standard mercury thermometers, and a Weather Measure

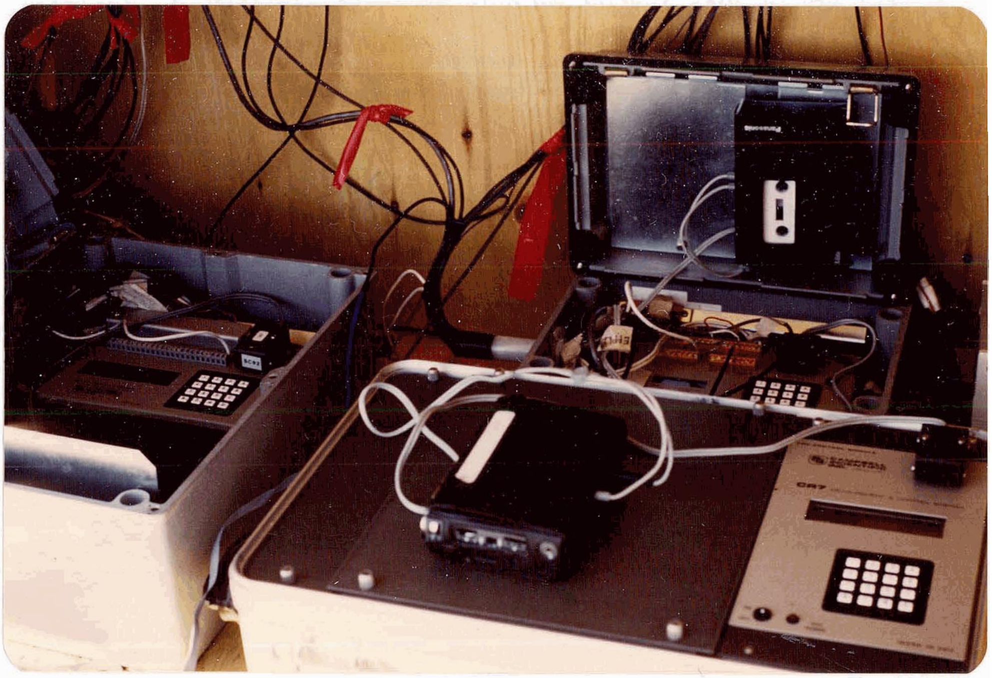

Figure 3.8. Photograph of data system installation.

thermohygrograph. A Weather Measure tipping bucket rain gauge was placed on the ground adjacent to the data logger shelter, and two standard precipitation collection gauges were placed near the Stevenson screen. A Weather Measure barograph and Thommen altimeter were placed in the data logger shelter.

3.4 Summary of Conditions During Experiment

The investigation was conducted over the period June 25 - July 26 1985. The general regional weather conditions during the experiment period can be summarized as being slightly warmer and sunnier than average, and much drier than average. The May through July period of 1985 was one of the driest recorded in southern Alberta. Monthly data from selected meteorological stations in the area are presented in Table 3.2. Daily data from the Plateau Mountain site are presented in Table 3.3.

The beginning of the investigation coincided with a general increase in temperature in the region. Minimum temperatures of less than 0°C were regularly recorded at Hailstone Butte and Raspberry Ridge lookouts in the first three weeks of June, but did not occur after that date. For the period of the experiment the mean daily temperatures at Hailstone Butte and Raspberry Ridge lookouts were 12.0°C and 11.6°C, respectively. Mean daily temperatures at Plateau Mountain were approximately 1 - 2°C cooler than at the above stations. The above results are based on the standard procedure for determining mean daily temperature, using the morning readings of the maximum and minimum thermometers.

Peak streamflow occurred in the Plateau Mountain area in late May and early June, and this is probably the period when most of the snow on Plateau Mountain melted (Alberta River Forecast Centre, personal communication). The flat summit topography and its exposure to the prevailing winds prevent much of the summit area from accumulating a thick snow

Table 3.2. Monthly precipitation, mean air temperature and hours of bright sunshine at Raspberry Ridge, Hailstone Butte, Kananaskis, Banff and Calgary, May - July, 1985.

Station		Precip. (mm)	Percent of normal	Temp. (°C)	Difference from normal (°C)	Hours of bright sunshine	Percent of normal
Raspberry Ridge	May	NA	NA	NA	NA	NA	NA
	June	23.4	26 %	5.7	-0.5	NA	NA
	July	21.0	46 %	12.4	2.4	NA	NA
Hailstone Butte	May	NA	NA	NA	NA	NA	NA
	June	16.7	17 %	5.8	-0.3	NA	NA
	July	30.5	55 %	12.3	2.3	NA	NA
Kananaskis	May	62.8	79 %	8.9	1.8	260.5	123 %
	June	34.2	34 %	10.7	-0.4	265.0	111 %
	July	31.4	52 %	15.4	1.4	327.3	115 %
Banff	May	65.4	126 %	9.5	1.8	NA	NA
	June	51.8	84 %	14.7	3.1	NA	NA
	July	15.0	35 %	17.2	2.5	NA	NA
Calgary	May	21.9	45 %	11.8	2.4	281.8	119 %
	June	40.9	46 %	13.1	-0.4	328.6	123 %
	July	53.2	81 %	18.4	2.1	359.4	112 %

NA indicates that data was not available.

Source: Monthly Weather Record Atmospheric Environment Service, Environment Canada. Normal values are from Canadian Cimate Normals, 1951 - 1980. Atmospheric Environment Service, Environment Canada.

Table 3.3. Daily precipitation, air temperature[1], surface temperature and windspeed[1] data for Plateau Mountain, June 26 - July 26, 1985.

Date	Precip. (mm)	T_{max} (°C)	T_{min} (°C)	Mean T (°C)	$T_{o\,max}$[2] (°C)	Mean T_o (°C)	u_{max}[2] (m s⁻¹)	Mean u (m s⁻¹)
June 26	0.5	13.9	-0.5	6.7	27.7	11.0	--[3]	--
June 27	0.8	16.4	2.8	9.6	29.7	12.2	6.8	4.7
June 28	0.0	16.9	5.6	11.3	28.1	13.7	5.5	3.9
June 29	0.8	17.8	6.1	12.0	29.6	13.7	6.9	4.9
June 30	0.0	17.8	9.4	13.6	30.7	13.7	6.3	3.8
July 1	0.0	19.4	9.4	14.4	31.5	15.5	8.9	5.8
July 2	0.0	19.4	7.8	18.6	31.2	15.5	9.5	6.5
July 3	0.0	20.5	8.3	14.4	32.9	17.5	8.9	5.5
July 4	0.0	22.5	8.0	15.3	38.6	18.2	6.5	3.7
July 5	0.0	19.4	11.7	15.6	30.5	16.9	9.3	7.7
July 6	0.0	19.4	1.7	10.6	30.7	14.8	10.3	7.2
July 7	0.0	19.4	4.4	11.9	30.9	15.7	8.9	5.4
July 8	0.0	21.7	10.0	15.9	34.8	18.0	10.3	6.7
July 9	0.0	22.8	10.6	16.7	34.8	18.1	---	--
July 10	0.5	21.6	8.9	15.3	31.0	16.6	9.8	5.6
July 11	0.0	20.6	8.9	14.8	34.0	16.9	7.3	4.9
July 12	0.0	15.6	5.6	10.6	26.6	12.1	7.2	4.0
July 13	0.5	10.0	1.6	5.8	20.1	8.9	6.1	2.6
July 14	0.0	16.7	0.6	8.7	34.6	13.9	---	--
July 15	1.5	13.3	7.2	10.3	33.1	13.7	7.0	3.8
July 16	9.8	----	---	----	26.0	8.4	8.5	4.1
July 17	16.0	----	---	----	14.3	4.7	4.8	3.0
July 18	0.0	16.0	-1.7	7.2	25.3	10.1	5.5	3.7
July 19	0.0	----	----	----	28.8	11.8	4.9	3.2
July 20	0.0	20.6	5.6	13.1	33.7	15.3	7.5	4.3
July 21	0.0	22.2	2.2	12.2	35.0	18.0	5.9	4.2
July 22	1.0	21.7	10.0	15.9	32.9	15.5	9.4	5.4
July 23	5.5	14.4	5.0	9.7	22.5	10.4	8.7	3.7
July 24	0.0	15.6	2.2	8.9	26.6	11.9	7.2	4.8
July 25	0.0	17.2	3.3	10.3	31.2	14.4	6.9	4.2
July 26	0.0	---	---	---	32.0	15.6	7.6	4.6

[1] Air temperature and windspeed at 1 m above the surface.

[2] Half-hour average value.

[3] Dashed lines indicate that data was not available.

cover. A large snow cornice persisted along the eastern edge of the mountain for most of the summer of 1985. The lack of thick snow cover at the instrumentation site and the early runoff period suggest that the surface of Plateau mountain had already undergone some drying before the investigation began. However, the surface was noticeably damp in the early part of the investigation.

Only two significant precipitation events occurred during the experiment. Evening thunderstorm activity in the early part of the investigation was common, but resulted only in traces of precipitation at the site. The first significant precipitation event occurred in the period July 15-17 and resulted in 27 mm of precipitation at Plateau mountain, 24.6 mm of precipitation at Hailstone Butte lookout and 17.0 mm of precipitation at Raspberry Ridge lookout. This was a mixed rain and snow event at Plateau Mountain. The second event occurred in the period July 22-23 and resulted in 6.5 mm of precipitation at Plateau Mountain, 5.1 mm of precipitation at Hailstone Butte lookout, and 4.2 mm of precipitation at Raspberry Ridge lookout. All this precipitation fell as rain at Plateau Mountain.

The determination of the surface moisture regime at Plateau Mountain proved difficult. There was considerable areal variation in the distribution of soil moisture, with the tops of the hummocks tending to be much drier than the areas under the mat plants, and between the hummocks. This variability was apparent in the samples from both the 0-50 mm and 50-100 mm soil layers. The daily estimates of soil moisture from the 0-50 mm layer, along with the daily precipitation amounts, are presented in Figure 3.9. The large standard deviations for the soil moisture measurements shown in Figure 3.9 are due to the areal variations in the daily samples. Standard deviations are not shown for the soil moisture values determined by interpolation.

Throughout the investigation, the deeper layers of the soil (depths > 0.2 m) were qualitatively observed to be very moist. As with the soil moisture in the 0-50 mm layer, there appeared to be considerable areal variation of this deeper soil moisture. At the beginning of the experiment, liquid water was observed in the soil at a depth of 0.16 m . On July 1, despite the lack of precipitation and the strong drying conditions preceding this day, liquid water could still be observed in the soil at depths of 0.20 m. At the end of the experiment it was noted that 0.3 m stakes used for the instrumentation mast guy wires came out of the ground with mud clinging to them.

The prevailing winds were from the southwest during the experiment, with winds from that direction being recorded for 64% of the experiment's duration. Half-hour windspeeds at 1 m above the surface were generally between 3 - 5 m s^{-1}. Instantaneous windspeeds approaching 20 m s^{-1} were recorded on several occasions. There were very few calm periods.

Surface atmospheric pressure as measured by the barograph was near constant at the site, with a maximum variation of less than 1.2 kPa. This was confirmed by the altimeter which showed very little variation.

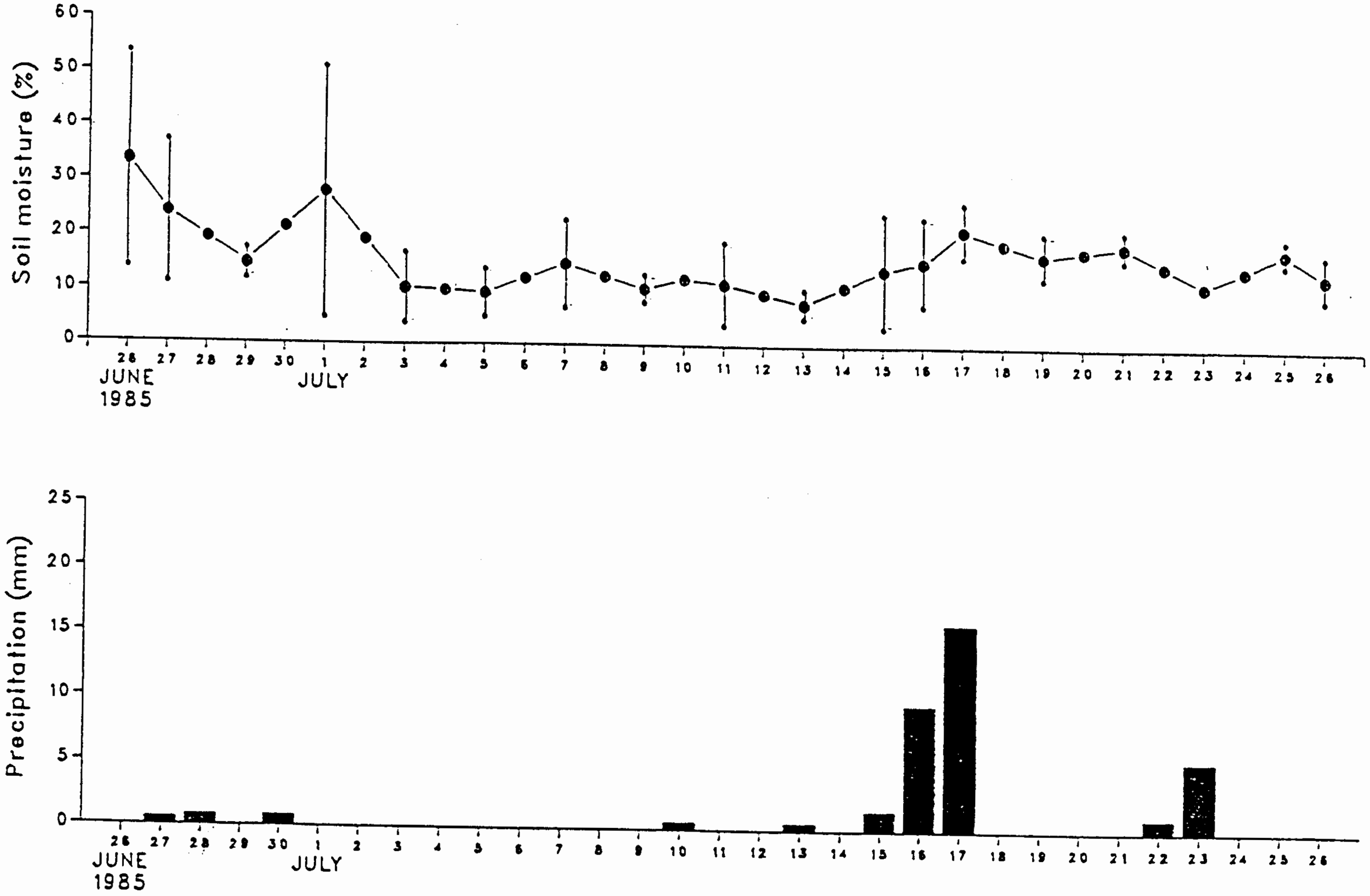

Figure 3.9. Daily volumetric soil moisture (0-50 mm) and precipitation, Plateau Mountain, June 26 - July 26, 1985.

CHAPTER 4

SURFACE RADIATION REGIME - MEASUREMENT RESULTS AND DISCUSSION

4.1 Introduction

In this chapter the results from the measurements of solar, longwave and net radiation flux densities made at Plateau Mountain are presented. Both daily data for the entire experiment, and half-hourly data for selected days are presented. The solar, longwave and net radiation regimes at Plateau Mountain during the experiment are then discussed. The empirical relationships between the measured K↓ and Q*, both daily and half-hourly, are presented and compared with a similar relationship derived by Davies (1967).

4.2 Measurement Results

4.2.1 Daily Data

All the daily, daylight and night values of the measured radiation balance components are presented in Appendix 3, along with the daily *t*, *a* and calculated daily K_0. The daylight period was defined as the sum of all the half-hour periods for which the calculated K_0 was greater then zero. Daily values for July 9 and July 14 are not included in Appendix 3, due to periods of missing data on these days. The data for July 17 includes a brief period when it is likely that some of the radiation sensors were covered by snow, and values for that day must be treated judiciously. The data from Appendix 3 are summarized in Table 4.1. The daily values of the radiation balance components over the period of the experiment are plotted in Figure 4.1, and the daily *a* and *t* are plotted in Figure 4.2.

Table 4.1. Summary of daily, daylight and night period radiation balance data, Plateau Mountain, June 26 - July 26, 1985.

		Minimum	Maximum	Mean	Std. Dev.	Coeff. of Variation
K_0	daily	38.8	41.8	40.6	---	--
$K\downarrow$	daily	10.3	33.1	25.8	6.1	0.238
$K\uparrow$	daily	1.9	5.7	4.4	1.0	0.230
K^*	daily	8.2	27.4	21.4	5.1	0.239
t	daily	0.257	0.793	0.635	0.15	0.233
a	daily	0.159	0.211	0.172	0.009	0.051
$L\downarrow$	daily	17.3	24.3	20.9	1.7	0.082
	daylight	12.1	16.8	14.4	1.3	0.087
	night	5.3	8.0	6.5	0.7	0.100
$L\uparrow$	daily	26.3	32.1	30.1	1.4	0.046
	daylight	18.3	23.7	21.7	1.3	0.059
	night	7.6	9.3	8.4	3.3	0.387
L^*	daily	-12.0	-2.4	-9.2	2.6	0.284
	daylight	-9.3	-1.8	-7.3	2.0	0.280
	night	-2.7	-0.4	-1.9	0.6	0.321
Q^*	daily	5.8	15.8	12.2	2.8	0.230
	daylight	6.3	18.1	14.1	3.3	0.232
	night	-2.7	-0.4	-1.9	0.6	0.321

All values are in $\mathrm{MJ\ m^{-2}}$, except t, a and coefficients of variation, which are dimensionless.
Values for July 9 and July 14 are excluded due to periods of missing data on those days.

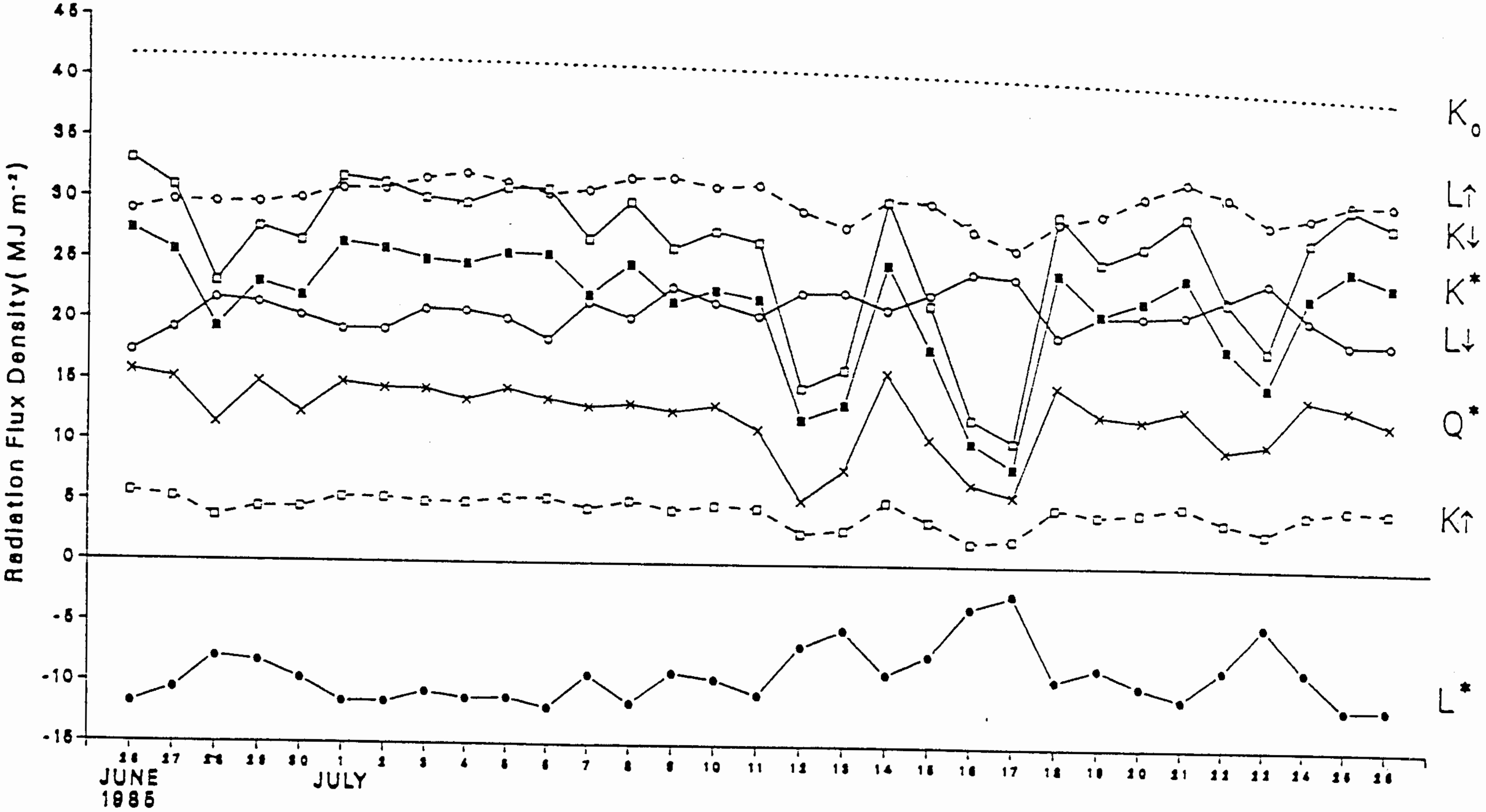

Figure 4.1 Daily radiation balance component flux densities, Plateau Mountain, June 26 - July 26, 1985.

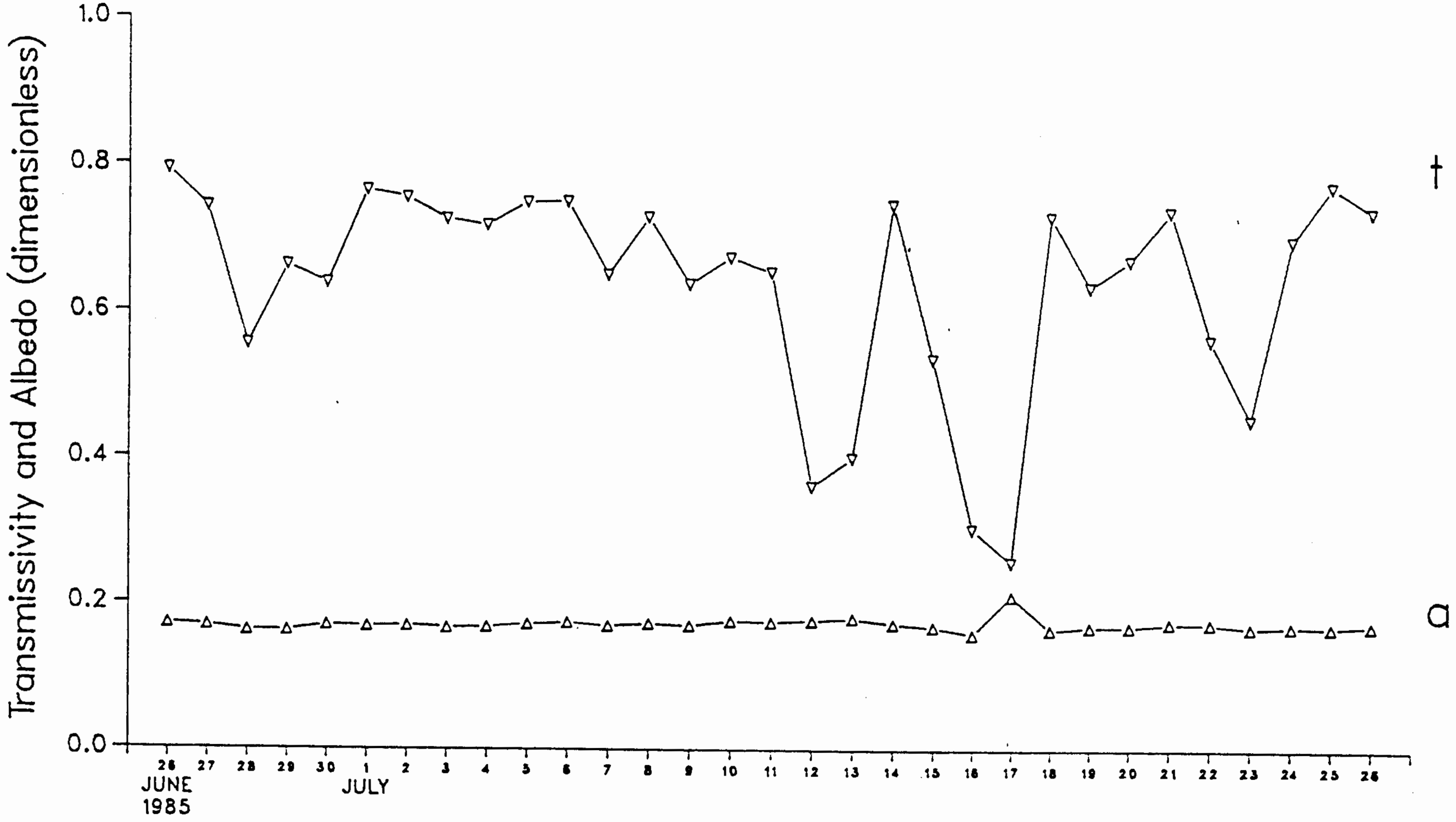

Figure 4.2. Daily atmospheric transmissivity and surface albedo, Plateau Mountain, June 26 - July 26, 1985.

4.2.2 Half-hourly Data for Selected Days

Five days of half-hourly radiation flux density data were selected to illustrate the characteristics of the daily radiation balance regime under different conditions. The days selected were June 26, July 10, July 17, July 18 and July 25. The half-hourly data from these days is summarized in Table 4.2

Data from June 26 and July 25 are presented to illustrate the radiation regime under near cloudless conditions. Data for these days are presented in Figures 4.3 and 4.4. There were no noticeable clouds during the daylight period of July 25, and only a very light buildup of cumulus clouds on the afternoon and evening of June 26. On June 26, the temporal proximity to the summer solstice, and the high daily t resulted in the highest daily K↓ during the experiment being measured.

The data for July 17 and July 18 includes radiation flux density measurements made during periods of heavy overcast skies and precipitation, partly cloudy conditions, and cloudless conditions. The effects of these varying conditions on the radiation balance are illustrated. The radiation balance data for July 17 and 18 are presented in Figures 4.5 and 4.6 .

Thunderstorms began on the afternoon of July 16 and developed into a general rain by that evening. The rain continued most of that night, changing to snow some time after sunrise on July 17. During the period between 13:00 MDT July 16, and 15:00 MDT July 17 over 25 mm of precipitation was recorded. The sky was completely obscured by heavy low cloud during this precipitation event. The cloud cover became more broken during the afternoon of July 17. For a portion of the morning of July 17 the site was snow covered. Figure 4.5 shows the effect of the snowcover on the radiation balance during this period. Figures 4.7 and 4.8 are photographs of the site taken during the snowstorm on the morning of July 17. The photographs show the greatly reduced visibility and heavy cloud cover during the snowstorm. The snow at the site on the morning of July 17 was gone by that afternoon. The night of July 17 and the morning of July 18 were cloudless, and the best visibility conditions during the experiment were experienced in this period. Cumulus cloud began developing over the site on the afternoon of July 18.

The data for July 10, presented in Figure 4.9, shows the effect of smoke and haze on the radiation regime of an otherwise cloudless day. On July 10 the sky conditions were near cloudless in the morning, but in the afternoon the sky was obscured by smoke and haze. The smoke originated from forest fires in the Canal Flats area of British Columbia, some 70 km west of Plateau Mountain. Small amounts of ash were also observed in the air and on the surface. Hailstone Butte and Raspberry Ridge lookouts also reported limited visibility due to smoke and haze on the afternoon of July 10.

The photographs in Figures 4.10 and 4.11 were both taken from approximately the same location, looking north from the data logger shelter. The photograph in Figure 4.10 was taken in the late afternoon of a day with good visibility, while the photograph in Figure 4.11 was taken at 17:30 MDT on July 10. The effect of the smoke on the visibility at the site on the late afternoon of July 10 is clearly shown.

Table 4.2. Summary of half-hourly radiation flux densities, Plateau Mountain, June 26, July 10, July 17, July 18, July 25, 1985.

	June 26	July 10	July 17	July 18	July 25
K_0 max	1177.0	1165.5	1155.1	1153.3	1139.1
K_0 mean	483.2	473.3	464.0	462.5	450.3
K↓ max	994.0	937.0	767.0	951.0	938.0
K↓ mean	383.3	318.8	119.5	337.8	347.7
K↑ max	160.5	151.5	115.5	153.6	149.5
K↑ mean	66.0	56.3	25.2	55.8	58.9
K* max	833.5	786.0	651.5	802.1	789.5
K* mean	317.4	262.6	94.3	281.9	288.7
L↓ max	232.9	308.5	310.3	251.5	244.6
L↓ min	167.6	228.0	218.7	187.5	165.7
L↓ mean	200.6	250.6	276.9	221.4	217.5
L↑ max	418.0	436.6	348.2	404.8	438.1
L↑ min	274.3	312.0	287.4	283.1	295.0
L↑ mean	335.7	361.2	304.3	330.4	351.6
L* max	-83.5	-15.0	12.8	-67.7	-77.1
L* min	-238.9	-206.1	-107.9	-178.6	-224.3
L* mean	-135.1	-110.6	-27.4	-109.1	-134.1
Q* max	609.5	579.9	567.0	628.9	567.2
Q* min	-91.5	-88.8	-69.7	-76.5	-89.6
Q* mean	182.3	152.0	66.9	172.9	154.7
a max	0.411	0.292	0.642	0.303	0.340
a min	0.159	0.159	0.134	0.149	0.156
t max	0.853	0.812	0.831	0.847	0.825
t min	0.355	0.333	0.043	0.448	0.331

All values are in W m^{-2}, except for a and t which are dimensionless.

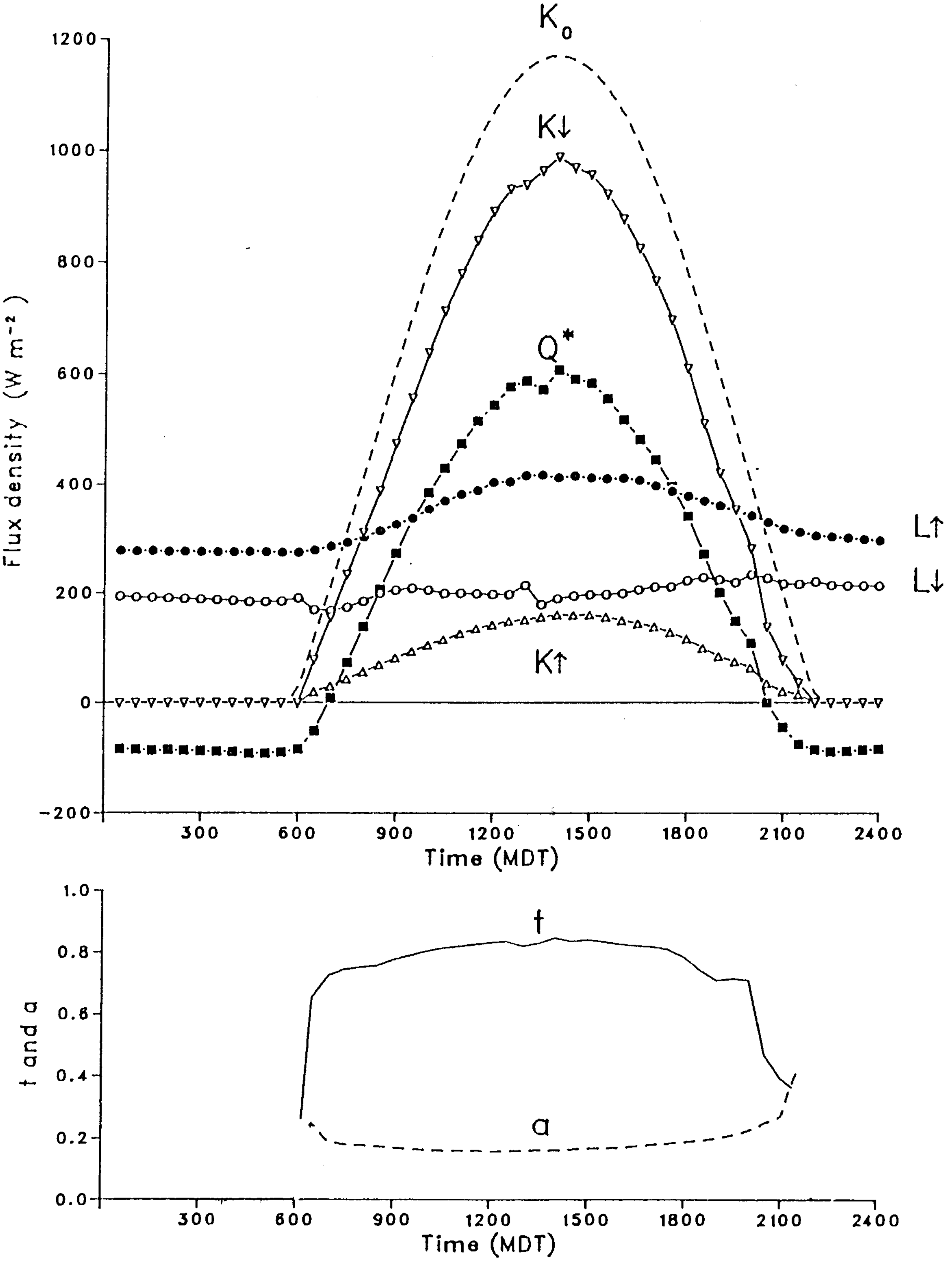

Figure 4.3. Half-hourly radiation flux densities, transmissivity and albedo for a near cloudless day, June 26, 1985, Plateau Mountain.

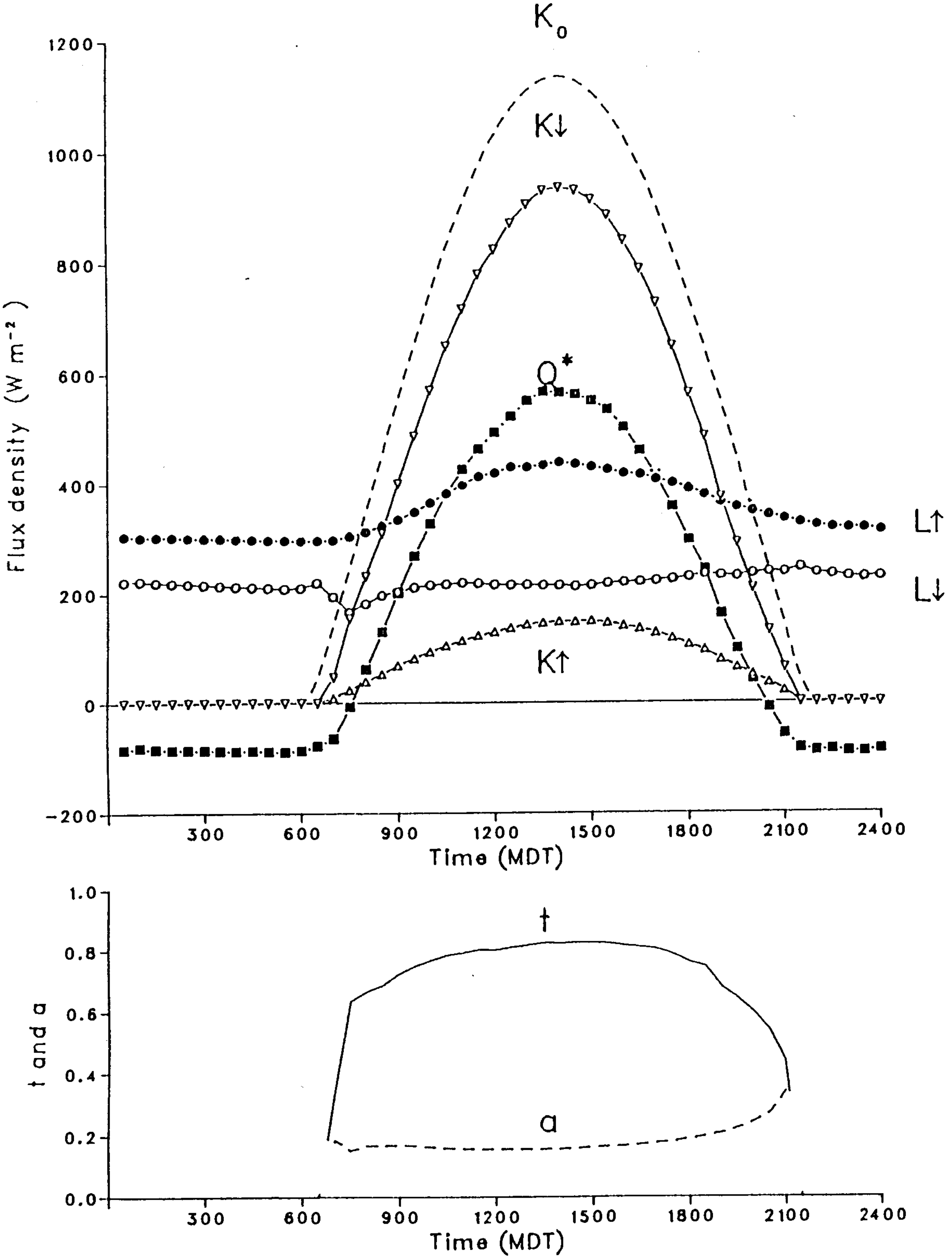

Figure 4.4. Half-hourly radiation flux densities, transmissivity and albedo for a near cloudless day, July 25, 1985, Plateau Mountain.

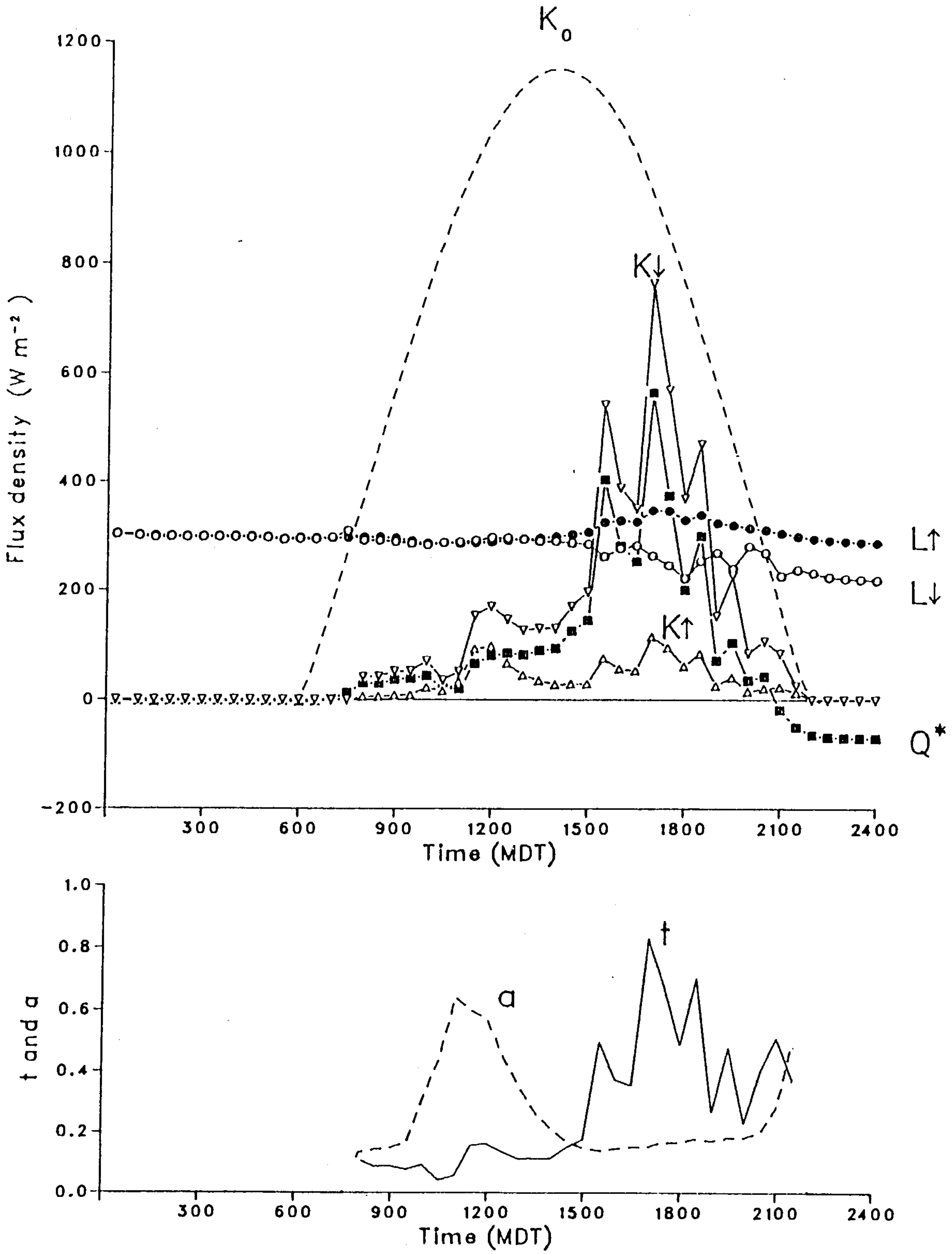

Figure 4.5. Half-hourly radiation flux densities, transmissivity and albedo during the snowstorm and subsequent clearing on, July 17, 1985, Plateau Mountain.

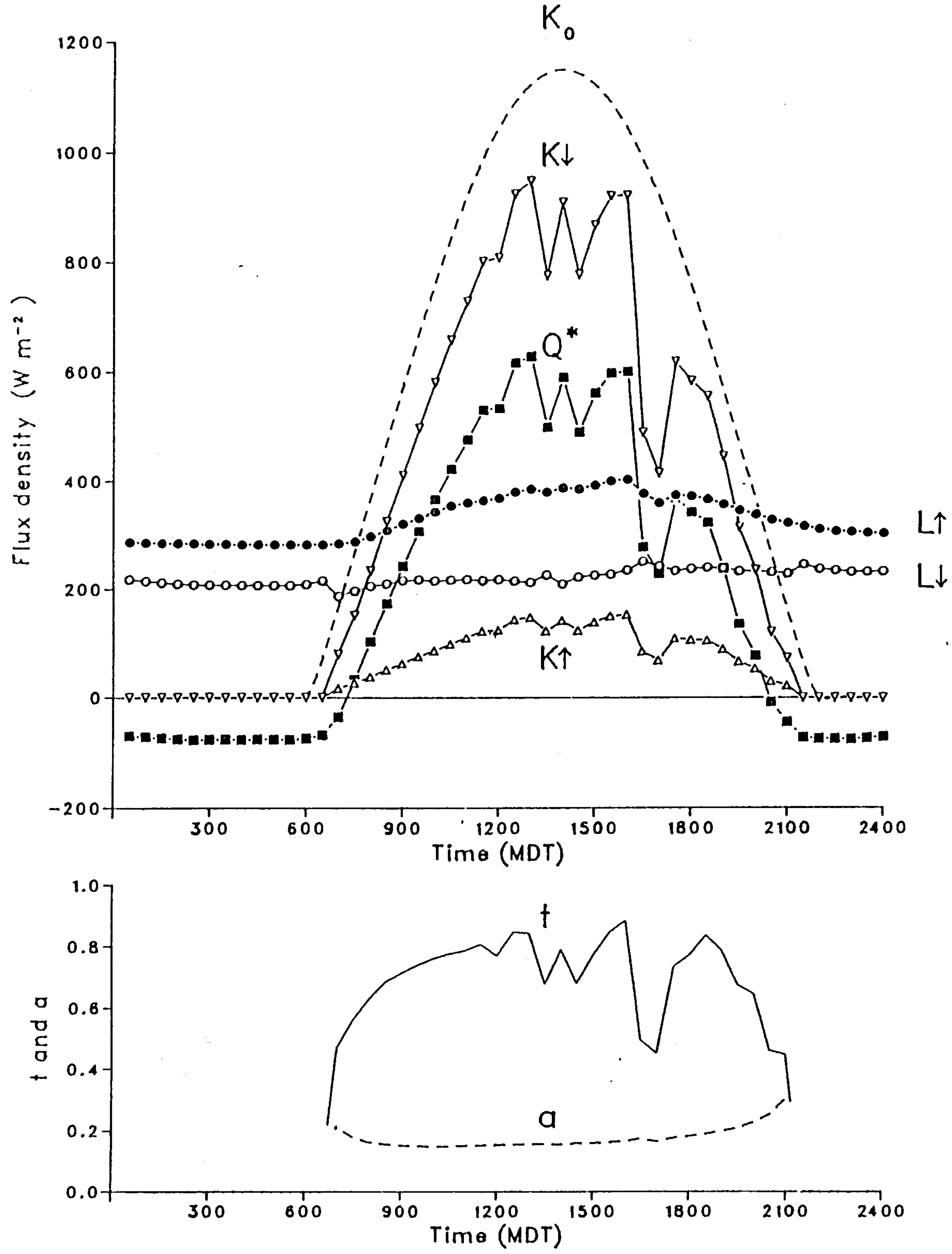

Figure 4.6. Half-hourly radiation flux densities, transmissivity and albedo during cloudy-bright conditions on July 18, 1985, Plateau Mountain.

Figure 4.7. Photograph of site during snowstorm on the morning of July 17, 1985.

Figure 4.8. Photograph of site during snowstorm on the morning of July 17, 1985.

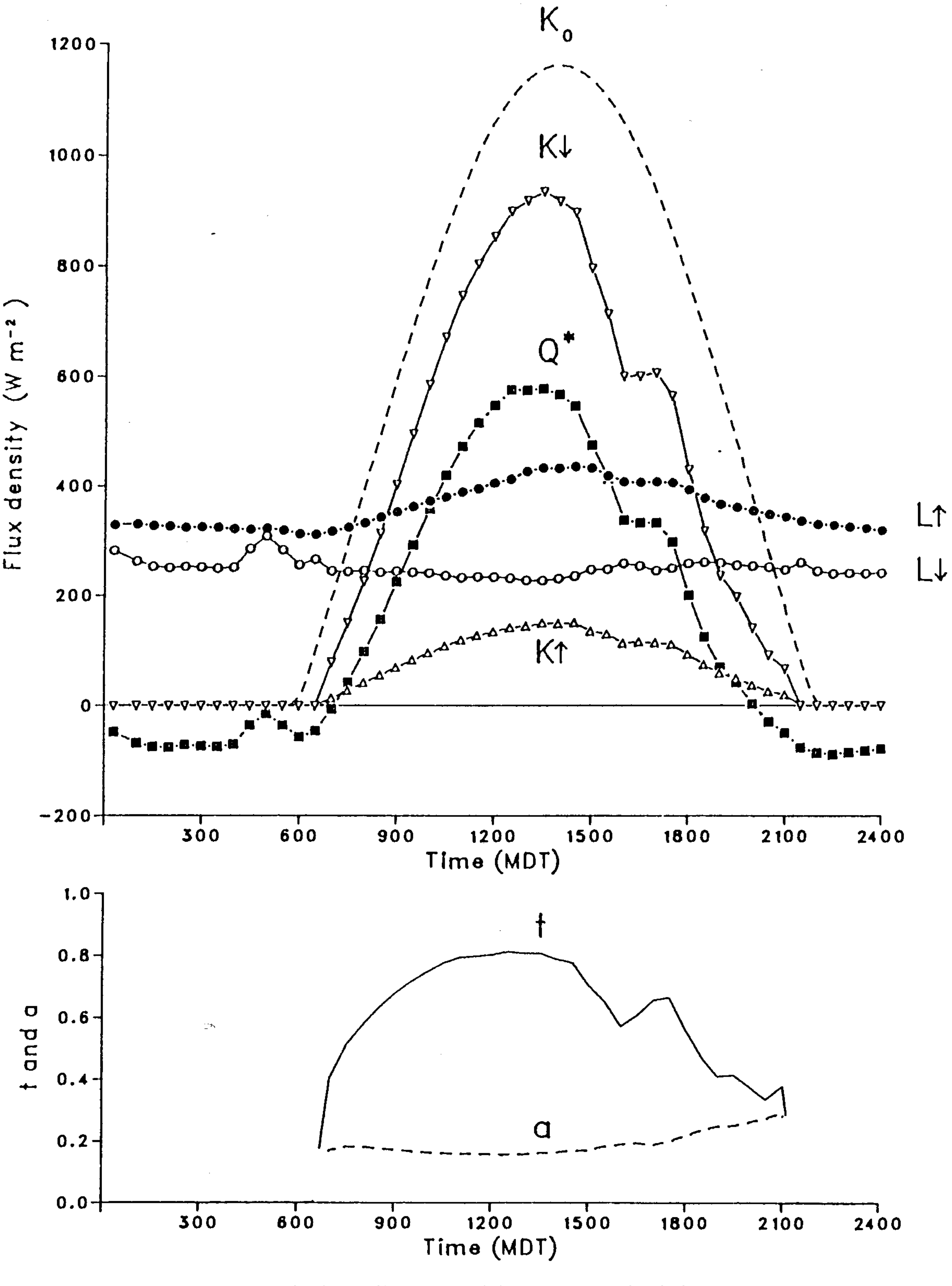

Figure 4.9. Half-hourly radiation flux densities, transmissivity and albedo, including a period when the sky was obscured by smoke and haze on July 10, 1985, Plateau Mountain.

Figure 4.10. Photograph taken looking north from instrumentation site on a day with good visibility.

Figure 4.11. Photograph taken looking north from instrumentation site on the afternoon of July 10, when the sky was obscured by smoke and haze.

4.3 Discussion of Solar Radiation Flux Densities, Transmissivity and Albedo

4.3.1 Solar Radiation Flux Densities

During the period of the experiment, the post-solstice decrease in solar declination resulted in a slight decrease in the magnitude of K_0, and a decrease in the length of the daylight period. The maximum half-hourly K_0 value went from 1177.0 W m^{-2} to 1139.1 W m^{-2}, and daylight period length decreased from 16.1 hours to 15.2 hours. As a result, daily K_0 decreased from 41.8 MJ m^{-2} on June 26 to 38.8 MJ m^{-2} on July 25.

As noted in Chapter 3, the region experienced below normal cloud cover during the experiment, with both Kananaskis and Calgary recording above normal hours of bright sunshine during June and July. The below normal cloud cover, in a region which normally receives high insolation during the summer (Hare and Thomas 1979), combined with the high t values characteristic of alpine locations, resulted in generally high daily $K\downarrow$ values being measured during the experiment. Daily $K\downarrow$ ranged from a maximum of 33.1 MJ m^{-2} on June 26, to a minimum of 10.3 MJ m^{-2} on July 17, averaging 25.8 MJ m^{-2} over the 28 days for which daily values were determined. The variations in the daily $K\downarrow$ values (std. dev. 6.1 MJ m^{-2}) were primarily a result of the variations in daily t, as illustrated in Figure 4.2 . Although the daily $K\downarrow$ values were essentially determined by daily t, the decreasing daylength also had a slight effect. For example, on July 2 the daily t (0.76) was slightly less than that for July 25 (0.77). However, the daily $K\downarrow$ on July 2 (31.3 MJ m^{-2}) was slightly greater than for July 25 (30.0 MJ m^{-2}).

Figure 4.2 also shows that daily a was essentially constant at the site. As a consequence of the constant nature of daily a, daily $K\uparrow$ and K^* closely tracked daily $K\downarrow$. As there was only a slight seasonal change in K_0, and daily a was almost constant, variations in daily t had the most effect on the daily solar radiation balance over the period of the experiment. The controlling role played by daily *t* on the daily solar radiation balance is clearly shown by the similarity of the coefficients of variation for daily *t*, $K\downarrow$, $K\uparrow$ and K^*.

4.3.2 Transmissivity

Average daily *t* was 0.635, but variable (std. dev. 0.148). The lowest daily *t* (0.303) occurred on July 17, a day characterized by extensive cumulus cloud cover and precipitation. The highest daily *t* (0.793) was measured on June 26, a day characterized by near cloudless sky conditions. Daily *t* did not exhibit a particular trend over the experiment period, although more low daily *t* values were recorded in the latter part of the experiment than in the early part. This is primarily attributable to the increased frequency of cloud cover in the daylight periods, during the latter part of the experiment. The decreasing solar declination after the summer solstice, and the consequent increase in M would have only reduced daily *t* by approximately 0.01 over the period of the experiment.

The high daily *t* values characteristic of high elevation locations were experienced on several occasions during the experiment. Daily *t* exceeded 0.75 on 6 days, and approached 0.80 on 2 of those days. Similarly high daily *t* values have been measured at other mid-latitude alpine sites, and at lower elevation sites on particularly clear days (Gates and Janke 1966; Terjung et. al. 1969; Ripley and Redman 1976; Staudinger and Rott 1981). Figures 4.3 and 4.4 show that on days without cloud cover, half-hourly *t* was essentially a function of the solar zenith angle. On these days the maximum half-hour *t* value would occur at solar noon and would approach 0.85. On days with partial cloud cover, the half-hourly maximum *t* values would also approach 0.85 during bright periods when the solar disc was not obscured by clouds.

Cloud cover effects on *t* obviously varied with the cloud type, extent, duration, location and time of day. Cloud cover observations were not made continuously during the experiment, and were not made in enough detail to quantify the effects of clouds on *t*. Persistent and complete coverage of the sky by heavy low cloud, as on the morning of July 17, resulted in the most significant and continuous reduction of *t*. More characteristically, the sky was only partially obscured by clouds. Partial cloud cover resulted in effects ranging from the large fluctuations in *t* during periods of alternating cloudy-bright conditions, as seen on the afternoons of July 17 and July 18, to the almost insignificant reductions in *t* caused by the passage of single clouds, as seen at mid-day on June 26. The data for June 26 also shows the effect of the development of thunderclouds in the late evening, which accelerated the decrease in *t* during the last few hours of the daylight period.

The smoke, haze and ash in the atmosphere on the afternoon of July 10 reduced *t*. Cloud cover in this period may have had an effect on *t*, but as the sky was completely obscured by smoke it was impossible to make cloud observations. Sky conditions prior to, and immediately after, the smoke period suggest that clouds were not involved in the reduction of *t*.

As it is based on a large number of observations at varying altitudes, Lowry's (1980) empirical relationship between direct-beam transmissivity and atmospheric pressure provides an interesting standard against which the transmissivity data from Plateau Mountain can be compared. Assuming "dry conditions" and a constant atmospheric pressure of 75 kPa, the Lowry expression would predict a maximum half-hourly *t* of 0.828 on June 26, decreasing to 0.824 on July 25, which agrees very well with the observed maximum values on those days. In Figures 4.12 and 4.13 the observed half-hourly *t* values for June 26 and July 25 are compared with the predicted values from the Lowry expression. In both cases there is very good agreement between the predicted and observed values. This is particularly surprising considering that the observed *t* values are based on calculations which do not discriminate between direct solar radiation and diffuse solar radiation, while the Lowry expression only predicts direct beam transmissivity.

The divergence between the predicted and observed values on the morning of June 26 may be attributable to this discrepancy.

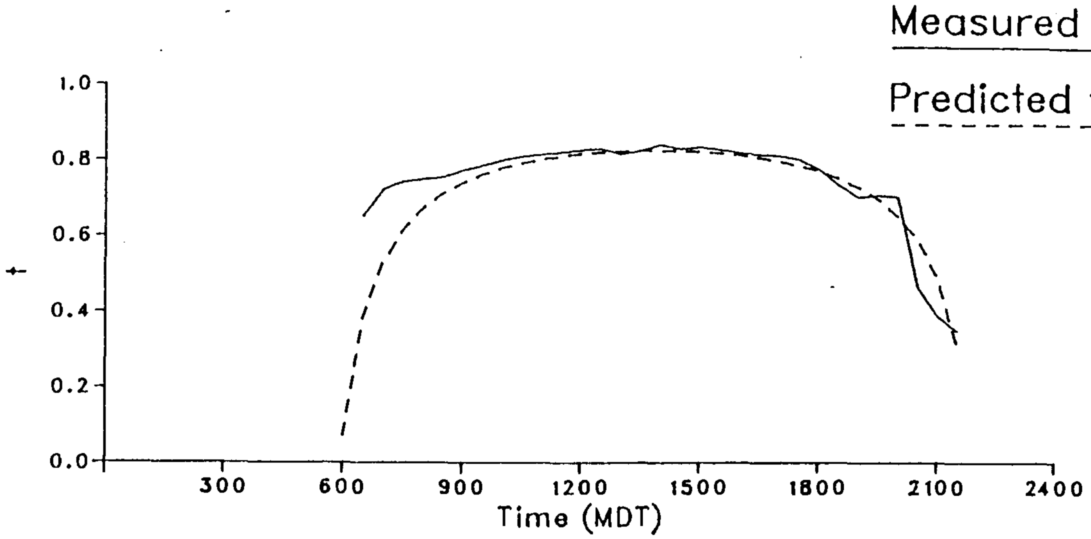

Figure 4.12. Comparison of predicted (Lowry expression) and observed half-hourly transmissivity at Plateau Mountain, June 26, 1985.

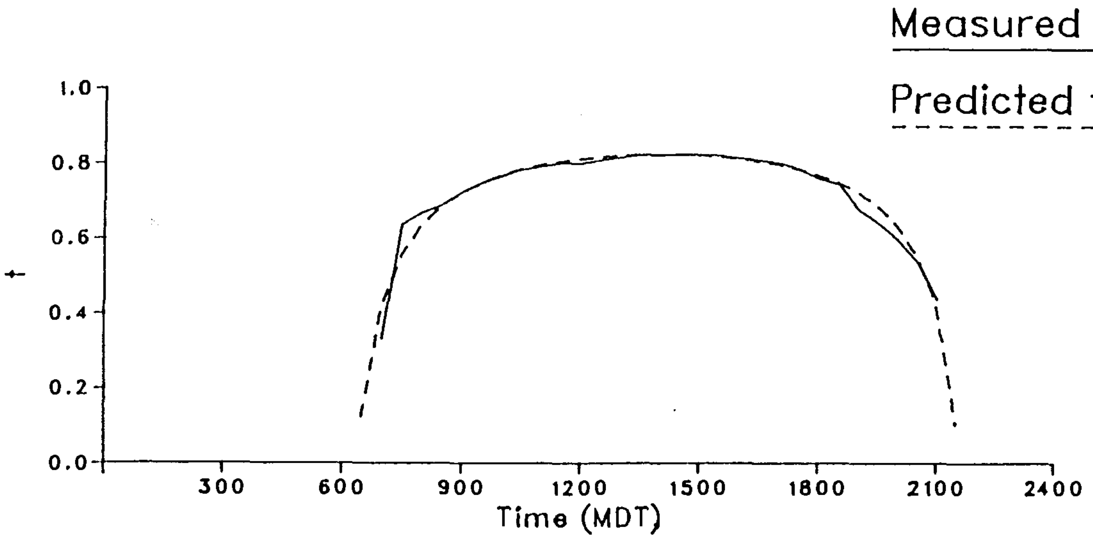

Figure 4.13. Comparison of predicted (Lowry expression) and observed half-hourly transmissivity at Plateau Mountain, July 25, 1985.

4.3.3 Albedo

In contrast to *t*, the daily *a* was near constant throughout the experiment. The average daily *a* for the experiment was 0.172 (std. dev. 0.051) .

The highest daily *a* (0.211) was measured on July 17 and can be attributed to the snow cover on the morning of that day. The decrease in *a* as the snow melted is seen in Figure 4.5. The lowest daily average (0.159) occurred on July 16, and may be a function of the darkening of the bare soil surfaces as a result of wetting from precipitation. As Figure 4.2 shows, the increase in *a* on July 17 was the only significant fluctuation in daily *a* over the course of the experiment. Excluding the data for July 17, the average daily *a* for the experiment becomes 0.170, with a standard deviation of less then 0.005. In the absence of snowcover, daily *a* is considered to be essentially constant at this site. Despite phenological changes in vegetation there was little effect on daily *a*. Rouse (1984) also found little change in the average daily *a* of a sub-arctic tundra site over the summer season. The value of 0.170 is quite similar to published values for daily summer albedos of arctic and sub-arctic tundra sites (Davies 1963; Petzold and Rencz 1975; Lewis and Callaghan 1976; Rouse 1984).

Half-hourly *a* showed a characteristic diurnal pattern, with the maximum albedos occurring just after sunrise and before sunset, and the minimums occuring around solar noon. This pattern is primarily attributable to the increase in *a* associated with increases in Z. This relationship has been observed by others over both agricultural and tundra surfaces (Davies and Idso 1969; Nkemdirim 1972; Greenland and Clothier 1975; Rouse 1984) The relationship between half-hour *a* and Z at Plateau Mountain on the five selected days is presented in Figures 4.14 - 4.18 . Figure 4.16 shows that the snowcover on the morning of July 17 resulted in a substantial deviation from the characteristic diurnal pattern.

Theory suggests that the variation of a with Z will be greatest at sites where the ratio of direct solar radiation to diffuse solar radiation is high (Monteith 1973). Rouse (1984) reports no variation in a with Z at a tundra site on overcast days. Interestingly, the Plateau Mountain data shows an increase in afternoon a even on the afternoon of July 10, when the sky was completely obscured by smoke, and presumably the ratio of direct solar radiation to diffuse was low.

At Plateau Mountain the relationship between a and Z was not constant throughout the day, afternoon a being consistently higher than morning a. The lack of symmetry is probably a result of a combination of various factors. The high relative elevation of the site and the slight slope of the surface may have resulted in the $K\uparrow$ sensor "seeing" a small portion of the sky above the western horizon. There were also probable differences between the relative amounts of direct and diffuse radiation in the afternoon and morning $K\downarrow$, and differences in the spectral composition of afternoon and morning $K\downarrow$. These factors would occur as a result of differences in the amounts of aerosols, water vapour and other atmospheric constituents in the air mass west of the site, as compared to the air mass east of the site. The possibility of a systematic sensor error was investigated and ruled out. However, it is noteworthy that the greatest differences were measured between the early morning and late afternoon albedos. At these times both $K\downarrow$ and $K\uparrow$ are low in magnitude, and small errors in the measurement of either parameter will result in large errors in the determined a.

The overall impact of the differences between afternoon and morning a on the radiation balance at Plateau Mountain is considered to be negligible. The largest differences occur when the radiative fluxes are small, and for most of the daylight period the half-hourly a values fell in the range of 0.15 - 0.18.

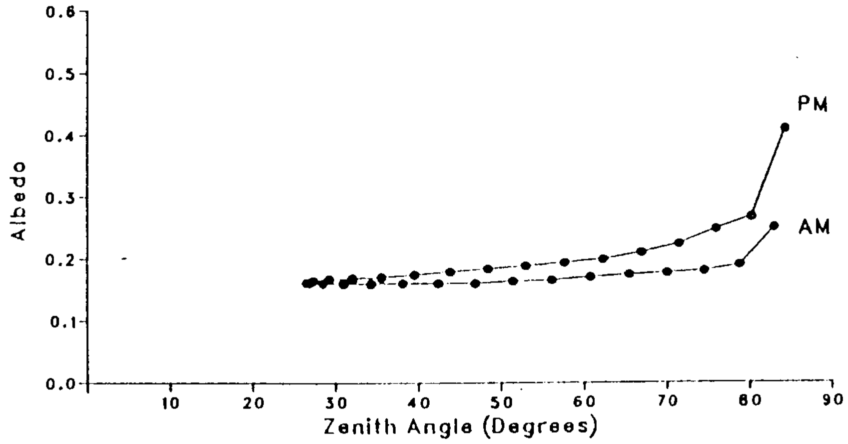

Figure 4.14. Half-hourly albedo vs. zenith angle, June 26, 1985.

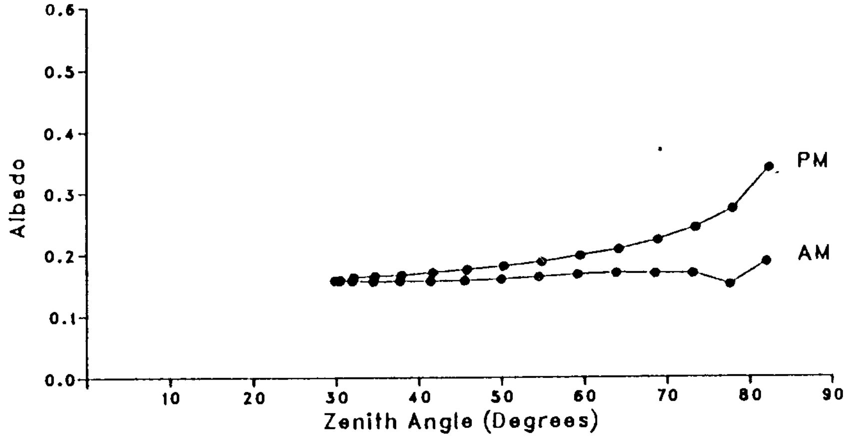

Figure 4.15. Half-hourly albedo vs. zenith angle, July 25, 1985.

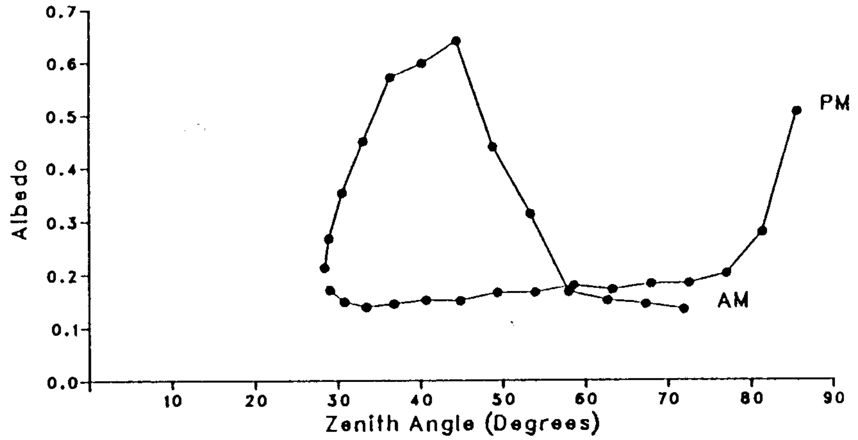

Figure 4.16. Half-hourly albedo vs. zenith angle, July 17, 1985.

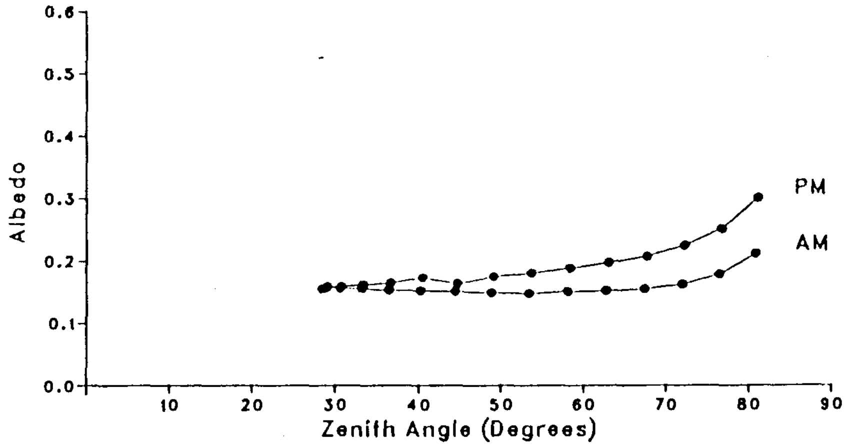

Figure 4.17. Half-hourly albedo vs. zenith angle, July 18, 1985.

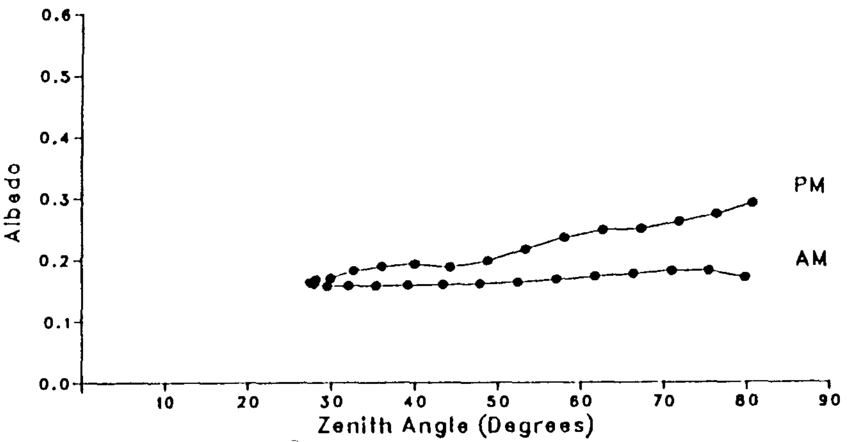

Figure 4.18. Half-hourly albedo vs. zenith angle, July 10, 1985.

4.4 Discussion of Longwave Radiation Flux Densities

Figure 4.1 shows that the daily $L\uparrow$ and $L\downarrow$ varied only slightly from their mean values during the experiment. The average daily values of $L\downarrow$ and $L\uparrow$ were 20.9 MJ m^{-2} (std. dev. 1.7 MJ m^{-2}) and 30.1 MJ m^{-2} (std. dev. 1.4 MJ m^{-2}) respectively. Daylight period $L\downarrow$ and $L\uparrow$ were similarly constant, averaging 14.4 MJ m^{-2} (std. dev. 1.3 MJ m^{-2}) and 21.7 MJ m^{-2} (std. dev. 1.3 MJ m^{-2}) respectively. Night period values were more variable but smaller in magnitude. Night $L\downarrow$ and $L\uparrow$ averaged 6.5 MJ m^{-2} (std. dev. 0.7 MJ m^{-2}) and 8.4 MJ m^{-2} (std. dev. 3.3 MJ m^{-2}) respectively.

The tendency of L^* totals to approach 0 MJ m^{-2} at night, as $L\downarrow$ and $L\uparrow$ values became similar, is shown by the low magnitude of the average night period L^* (−1.9 MJ m^{-2}). Daylight values were larger in magnitude, approximately −9.0 MJ m^{-2} on days with small amounts of cloud cover. Heavy cloud cover resulted in daylight L^* totals approaching 0 MJ m^{-2}. The effect of cloud cover on daylight L^* totals is illustrated by the small magnitude of the daylight L^* value on July 17 (−1.8 MJ m^{-2}). Figure 4.5 shows the similarity of the half-hourly $L\uparrow$ and $L\downarrow$ during the period of extensive cloud on the morning of July 17.

As noted in Chapter 3, there was a general increase in surface temperatures during the experiment, which resulted in a general increase in $L\uparrow$. The mean surface temperature for the period of the experiment, 15.6°C, is very similar to the radiative surface temperatures measured at an arctic tundra surface during the summer by Rouse (1984). On the half-hour basis, $L\uparrow$ being a function of T_0, which is strongly dependent on Q^*, tended to follow the trend of the half-hourly Q^*. The strong dependence of Q^* on $K\downarrow$, discussed in a subsequent section, resulted in $L\uparrow$ tending to reach its maximum coincident with $K\downarrow$.

$L\downarrow$ appeared to be relatively independent of the solar radiation fluxes, and most of its variation can be attributed to variations in cloud cover. For example, the decreasing trend of $L\downarrow$ throughout July 17 is attributed to the change from the heavy cloud cover and fog of the morning to the scattered cloud cover of the afternoon, to the clear skies of that night. Similarly the small increase in $L\downarrow$ just before sunrise on July 10, is attributed to the passage of a small thunderstorm at this time.

The large potential error associated with the $L\downarrow$ measurements did not support the comparison of the $L\downarrow$ data with the results from atmospheric emittance models. The $L\downarrow$ data does reflect the elevational influence, with the values being less than summer values reported for lower elevation mid-latitude sites, but greater than those reported by LeDrew (1975b) at the 64 kPa level.

4.5 Discussion of Net Radiation Flux Densities

Daily and daytime Q^* averages over the experiment were 12.2 MJ m^{-2} (std. dev. 2.8) and 14.1 MJ m^{-2} (std. dev. 3.3), respectively. Although direct intercomparisons are difficult, these daily Q^* values are not unlike summer measurements from other mid-latitude sites at lower elevations, with similar albedos (Ripley and Redman 1976, Oke 1978, Rouse 1984). The similarity of the daily Q^* values measured at Plateau Mountain, with those measured on fine days at lower elevation sites, does suggest that during this experiment high daily K^* values were to some extent compensated for by small L^* values.

As would be expected from the nature of the solar and longwave radiation regimes, Q^* was largely dependent on $K\downarrow$, both on a daily and half-hourly basis. As shown in Figure 4.1, daily Q^* closely tracked daily $K\downarrow$, and the coefficient of variation for Q^* is similar to that for daily t. Similarly, half-hourly Q^* closely tracked half-hourly $K\downarrow$, and the maximums of

Table 4.3. Average daily and daylight period values for Q^*/K^*, Q^*/L^* and $Q^*/K\downarrow$, Plateau Mountain, June 26 - July 26, 1985.

		Q^*/K^*	Q^*/L^*	$Q^*/K\downarrow$
Daily	Mean	0.576	−1.404	0.477
	Std. Dev.	0.056	0.359	0.046
Daylight	Mean	0.665	−2.033	0.550
	Std. Dev.	0.042	0.437	0.034

half-hour Q^* and $K\downarrow$ were always coincident.

In Table 4.3 average daily values for Q^*/K^*, $Q^*/K\downarrow$ and Q^*/L^* are presented. The small standard deviations for the Q^*/K^* and $Q^*/K\downarrow$ ratios illustrate the constant nature of the relationship between solar and net radiation at this site. The larger magnitude of the Q^*/L^* ratio indicates the relatively smaller significance of the longwave component to the daily net radiation balance.

4.6 Relationships Between Solar and Net Radiation

A simple linear relationship between the daylight period Q^* and $K\downarrow$ measured at Plateau Mountain is presented in Figure 4.19. This relationship, based on 29 cases, has the form

$$Q^* = 0.512\ K\downarrow + 1.038\ (\mathrm{MJ\ m^{-2}}) \qquad (4.1)$$

with $r^2 = 0.946$ and a standard error of 0.719 MJ $\mathrm{m^{-2}}$. The Davies (1967) relationship, based on Q^* and $K\downarrow$ values from 14 stations around the world, is included for comparison.

Davies' (1967) relationship is based on some surfaces similar to the surface at Plateau Mountain. All the stations used by Davies had albedos comparable to that of Plateau Mountain, and 3 of the stations were located in the Canadian arctic and sub-arctic. All 14 stations were at or near sea level. The range of Q^* values considered was similar to that measured at Plateau Mountain. The slightly steeper slope of the Davies curve, as compared to the Plateau Mountain curve, suggests that the ratio of the daylight Q^* total to $K\downarrow$ was generaly smaller at Plateau Mountain, as compared to the 14 other stations. The difference between the Plateau mountain data and the data from the 14 lower elevation sites could be interpreted as supporting the suggestion that increases in solar radiation resulting from increases in elevation, are to some extent, compensated for by an increasingly negative L^*.

It has been noted (Idso 1971) that relationships between the daily values of $K\downarrow$ and Q^* are marred by a lack of data points around the origin. This weakness is apparent in Figure 4.19. Davies and Idso (1979) suggest that a relationship based on shorter term data may be more reliable for the purpose of estimating daylight Q^*. This approach would involve the substitution of measured mean short-term $K\downarrow$ values into the relationship to predict mean short-term Q^*, then multiplying that value by the length of the daylight period.

In Figure 4.20 the relationship between the measured half-hourly $K\downarrow$ and Q^* is presented. This relationship, based on 929 cases, has the form

$$Q^* = 0.680\ K\downarrow - 57.07\ (\mathrm{W\ m^{-2}}) \tag{4.2}$$

with $r^2 = 0.966$ and a standard error of 38.72 W m^{-2}. The slope of this relationship is greater than both the Davies relationship, and that of the relationship developed using the daylight values from Plateau Mountain. This relationship is quite similar to those presented by Nkemdirim (1973) for a wide variety of cropped surfaces near Calgary, Alberta, at approximately 1000 m asl. Nkemdirim (1973) used hourly data collected on cloudless days to develop his relationships. The empirical expression based on the daylight period data, the expression based on the half-hourly data and the Davies expression were evaluated in terms of their performance as predictors of daylight Q^* at Plateau Mountain for the period of the experiment. The results of the comparisons are presented in Table 4.4.

The tabulated results indicate that there was only a small difference between the performance of the site specific empirical expressions, and the more general Davies expression. The average relative error of the three expressions ranged from ±3% to ±7% . This is not considered a significant

Table 4.4. Comparison of the measured daylight period Q^* with Q^* values predicted from three empirical relationships between Q^* and $K\downarrow$, Plateau Mountain, June 26 - July 26, 1985.

	Linear regression coefficients[1]					Measures of difference[2]			
	N[3]	r^2	Std. error	a	b	MBE	RMSE	Std. dev. of differences	d
			MJ m^{-2}	MJ m^{-2}		MJ m^{-2}	MJ m^{-2}	MJ m^{-2}	
$Q^*(A)$[4]	29	0.946	0.700	0.780	0.946	0.00	0.69	0.71	0.986
$Q^*(B)$[5]	29	0.946	0.929	-3.53	1.257	0.20	1.20	1.20	0.969
$Q^*(C)$[6]	29	0.946	0.843	-1.32	1.141	0.73	1.17	0.93	0.968

[1] The linear regression coefficents are based on the regression of the predicted Q^* on the measured Q^*. a is the Y axis intercept, b is the slope of the regression line. In all cases, t test scores indicated a greater than 99.9% probability that $b \neq 0$.

[2] The measures of difference are based on the differences between the model predicted Q^* and the measured Q^*, as described by Fox (1981) and Willmot (1982). MBE is the mean bias error, RMSE is the root mean square error and d is the index of agreement.

[3] N refers to the number of daylight periods for which data was available.

[4] $Q^*(A)$ is the predicted Q^* from the equation based on the linear regression of the measured daylight period Q^* on the measured daylight period $K\downarrow$, $Q^* = 0.512\ K\downarrow + 1.038$ MJ $m^{-2}\ d^{-1}$.

[5] $Q^*(B)$ is the predicted Q^* from the equation based on the linear regression of the measured half-hourly Q^* on the measured half-hourly $K\downarrow$, $Q^* = 0.680\ K\downarrow - 3.184$ MJ $m^{-2}\ d^{-1}$.

[6] $Q^*(C)$ is the predicted Q^* from the empirical relationship proposed by Davies (1967), $Q^* = 0.617\ K\downarrow - 1.01$ MJ $m^{-2}\ d^{-1}$.

difference, as measurements of Q* are generally considered to have a relative errror of ±7% (Davies and Idso 1979) . Thus, it is concluded that for this site the Davies empirical expression could have been used with a high degree of confidence as a means of estimating daylight period Q*. The measured daylight Q* values are compared with values predicted using the Davies expression in Figure 4.21.

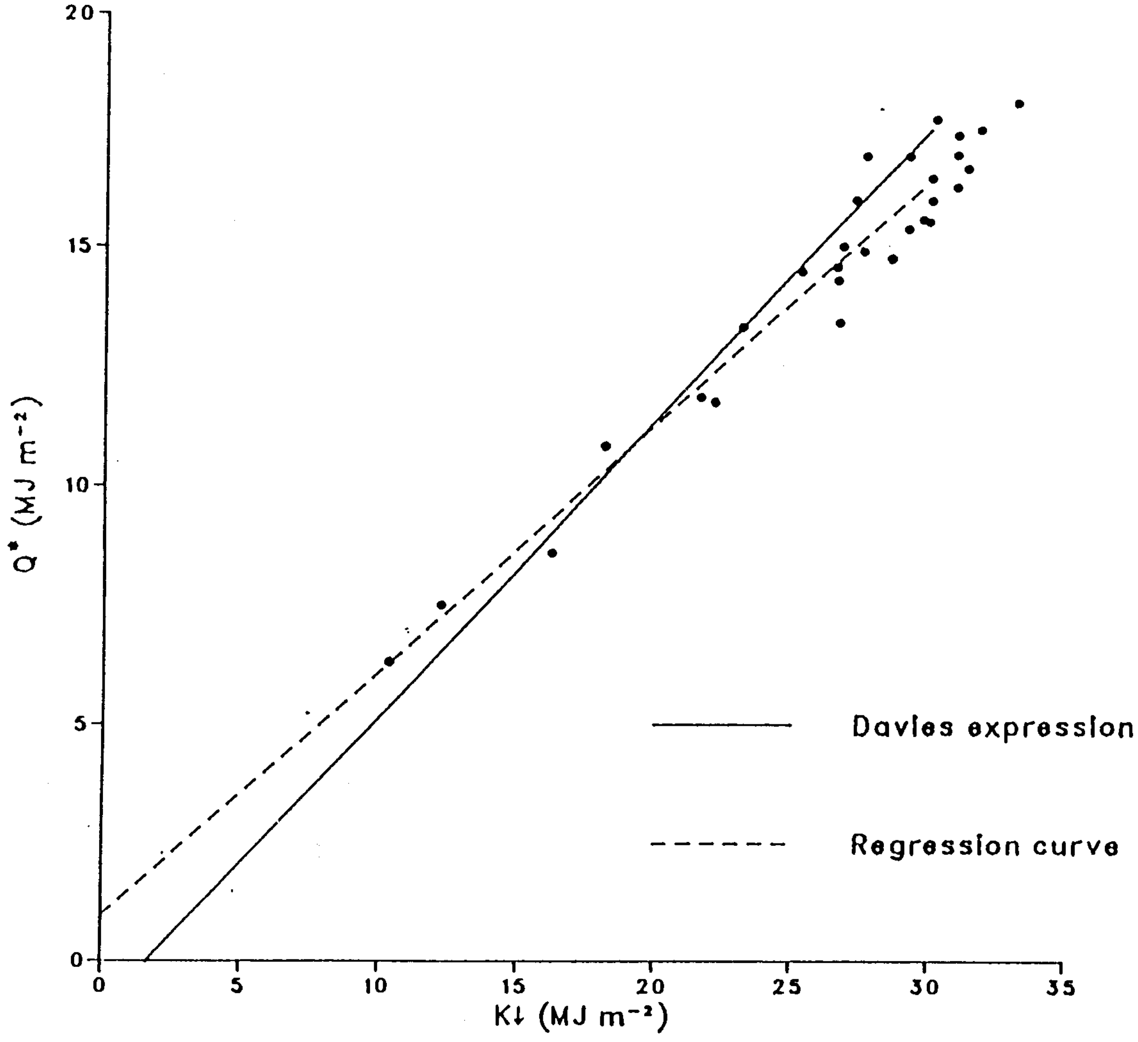

Figure 4.19. Measured daylight period Q* vs. daylight period K↓, Plateau Mountain, June 26 - July 26, 1985.

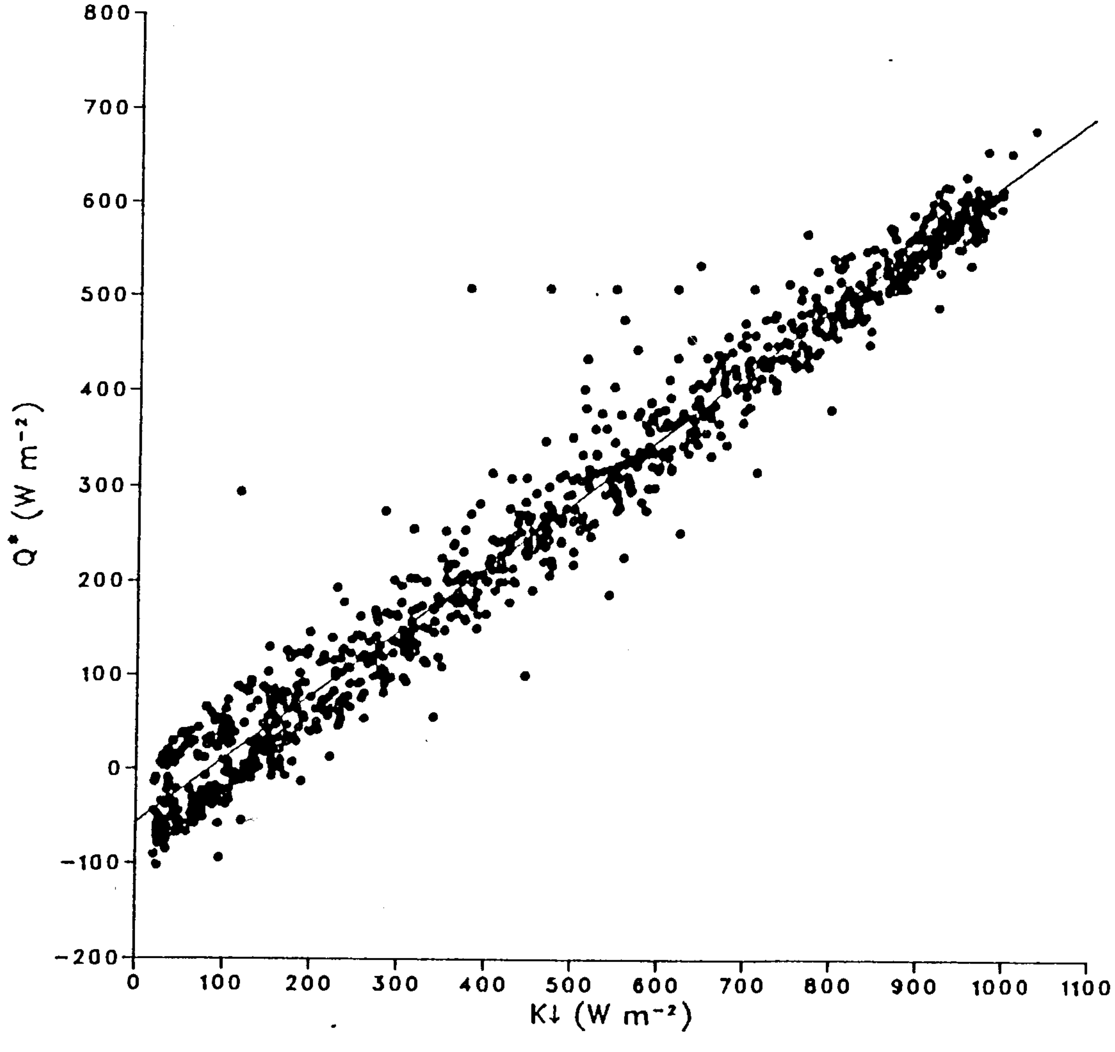

Figure 4.20. Measured half-hour daylight Q* vs. half-hour K↓, Plateau Mountain, June 26 - July 26, 1985.

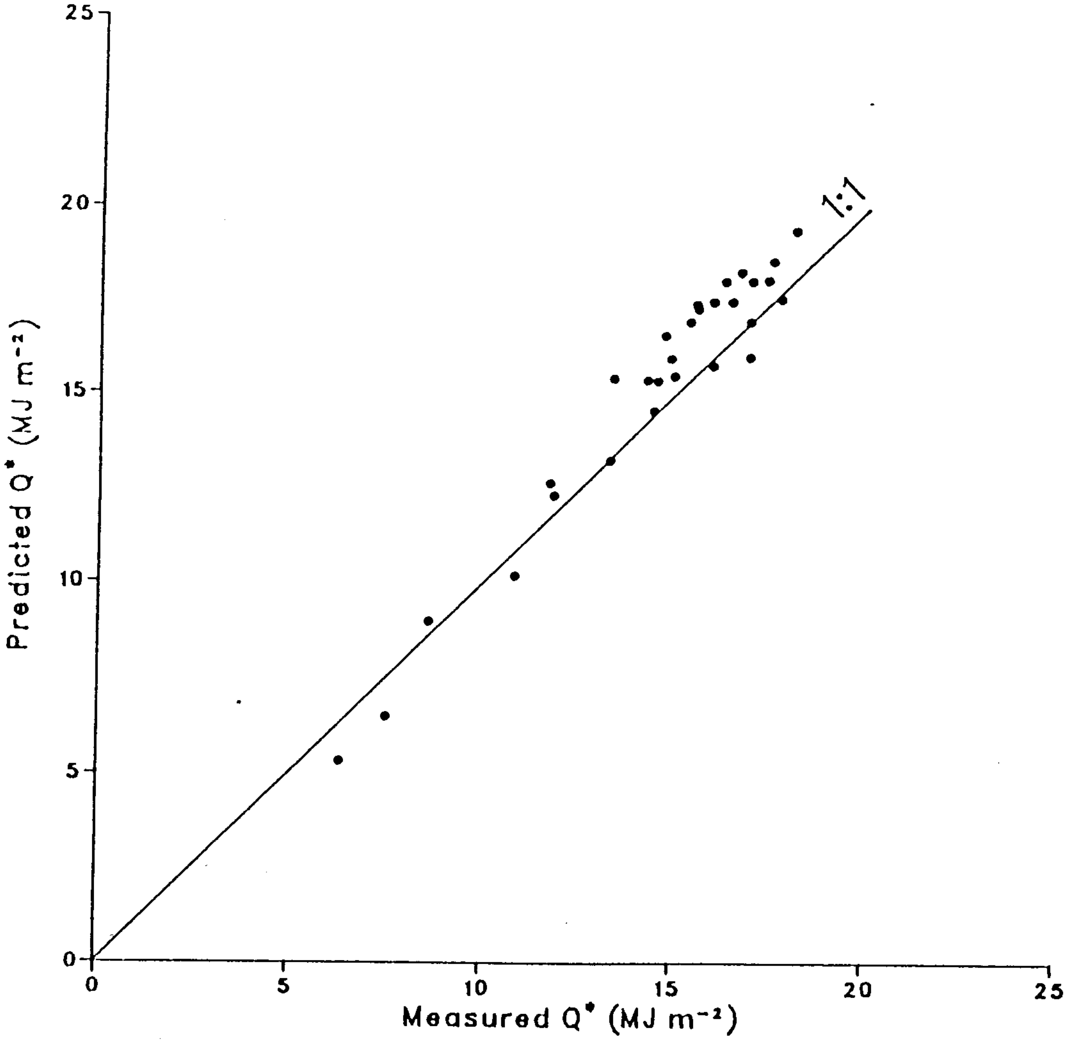

Figure 4.21. Predicted daylight period Q^* (Davies expression) vs. measured daylight period Q^*, Plateau Mountain, June 26 - July 26, 1985.

CHAPTER 5

SURFACE ENERGY BALANCE MEASUREMENTS AND MODELLING - RESULTS AND DISCUSSION

5.1 Introduction

In this chapter the results from the surface energy balance measurements made at Plateau Mountain are presented and discussed. First, the daily and half-hourly measurements made using the BREB approach are presented and discussed. Emphasis is placed on the discussion of surface effects on the energy balance. Then the Q_H measurements made using the eddy correlation approach, and the Q_H estimates made using the Ohm's law approach, are compared with the measurements made using the BREB approach. Finally, the results of using an equilibrium based approach to model daily Q_E, and a combination energy balance-Ohm's law approach to model half-hourly Q_E, are presented and discussed.

5.2 Description of the Surface Energy Balance Regime During the Experiment

5.2.1 Introduction

In this section, the nature of the surface energy balance regime at Plateau Mountain during the experiment is described. The energy balance is first described in terms of the daily and daylight values of the energy balance components. Half-hourly data for selected days is presented to provide more detail. The resultant surface and near surface zone thermal regimes are discussed, as is the behavior of the surface with regard to the movement of water from the tundra surface to the atmosphere. Finally, the surface energy balance regime over the course of the experiment is described.

All the measured daily, daylight and night period values for the energy balance components are presented in Appendix 4, along with the average β

and α values. The energy balance data from Appendix 4 is summarized in Table 5.1.

As specified in Appendix 4, some of the missing values in Table 5.1 are due to the problems with instrumentation and data recording. Other missing data is due to meteorological conditions which prevented the use of the BREB approach for determining convective fluxes. These latter problems are discussed more fully in subsequent sections.

The general summary of the energy balance regime presented in Table 5.1 shows that Q_G tended to be proportional to Q^*, and most of the variance in daily Q_G can be explained by the variance in daily Q^*. Daily Q_G was on average 8.4% of daily Q^*, and daylight Q_G was 13.6% of the daylight Q^*. The relationship between Q_G and Q^* is discussed more fully in Section 5.2.5.

Table 5.1 also shows that the energy balance was generally characterized by high Q_H values, and relatively small Q_E values. The average daily β was 1.89, the average daylight period β was 2.53. Previous energy balance studies conducted over the summer, in alpine environments, have reported lower average β values (LeDrew 1975; Staudinger and Rott 1981). This suggests that the Plateau Mountain site had a drier surface than other alpine sites which have been the subject of energy balance investigations. The highest daily Q_E value recorded during the experiment was equivalent to an evaporation rate of 4.2 mm per day and the lowest was equivalent to an evaporation rate of 0.6 mm per day. Addison and Bliss (1980) measured a similar range of daily evaporation rates at an arctic tundra fellfield site during the snow-free season.

In general,. the night period values for all the energy balance components were low in magnitude. Given the (1) similarity of the daylight and daily values, (2) more dynamic nature of the daylight period energy balance regime as compared to the night regime and (3) the larger error associated with the

Table 5.1. Summary of daily, daylight and night period energy balance data, Plateau Mountain, June 26 – July 26, 1985.

	N	Minimum	Maximum	Mean	Std. Dev.	Coeff. of Var.
$K\downarrow$	31	10.3	33.1	25.9	5.96	0.230
Q^*						
(daily)	30	5.3	15.7	12.2	2.76	0.226
(daylight)	29	6.3	17.5	14.1	3.23	0.229
(night)	29	−2.9	−0.4	−2.0	0.66	0.329
Q_H						
(daily)	22	2.2	11.8	6.3	2.59	0.411
(daylight)	22	3.7	13.8	8.0	2.54	0.318
(night)	22	−4.0	−1.1	−1.7	0.61	0.360
Q_E						
(daily)	22	1.4	10.5	5.1	2.50	0.490
(daylight)	22	1.4	8.7	4.8	2.27	0.472
(night)	22	−0.5	2.4	0.3	0.52	1.730
Q_G						
(daily)	28	−0.5	2.0	1.1	0.67	0.608
(daylight)	28	0.2	2.9	1.9	0.71	0.373
(night)	28	−1.1	−0.6	−0.8	0.15	0.185

N refers to the number of periods for which values were available. All other values are in MJ m^{-2}, except the coefficients of variation which are dimensionless.

determination of the night period values, as compared to the daylight period values, the remainder of the discussion will refer only to the daylight period energy balance values.

To facilitate the description of the energy balance regime, the days were categorized into three groups on the basis of the daylight period net radiation values and average β. This categorization enables the comparison of days which had similar magnitudes of available energy. This categorization is also useful for illustrating the effect of the availability of surface moisture on the daily energy balance regime. Surface moisture availability being a major factor in determining the partitioning of the available net radiative energy at the surface into Q_H and Q_E. The criteria for categorization were selected solely for the purpose of description. The three categories were as follows:

(a) Low Q^* days. These days had low to moderate Q^* values, generally less than 10 MJ m^{-2}. Four days fell into this category: July 12–13 and July 16–17.

The remaining days were then divided into two groups on the basis of the daylight period β:

(b) High Q^* and low β days. These days had high to moderate Q^* values, greater than 10 MJ m^{-2}, and a β of less than unity. Seven days fell into this category: June 30, July 1, July 18, July 20–21 and July 23–24;

(c) High Q^* and high β days. These days had high to moderate Q^* values, greater than 10 MJ m^{-2}, and a β of greater than unity. Into this category fell: June 27–29, July 4–8, July 10, July 16, July 19, July 22 and July 25–26.

July 2–3, July 9 and July 11 could not be categorized, although they had high Q^* values. On those days periods of missing data prevented the determination of an average β value for the entire daylight period.

Table 5.2 summarizes the daylight period energy balance component values for each category of day, as well as the soil moisture, daily mean windspeed, air temperature and α (data presented in Table 5.2 is discussed in

Table 5.2. Summary of mean daylight period energy balance flux densities, β, α, volumetric soil moisture (0-50 mm), air temperature and windspeed for categorized days, Plateau Mountain, June 26 - July 26, 1985.

	High Q^* and high β days.					High Q^* and low β days.					Low Q^* days.				
	N	Min.	Max.	Mean	Std. Dev.	N	Min.	Max.	Mean	Std. Dev.	N	Min.	Max.	Mean	Std. Dev.
Q^*	14	11.73	17.39	15.04	1.77	7	10.83	17.52	15.21	2.31	4	6.32	8.61	7.36	0.96
Q_H	14	5.81	13.79	9.17	2.21	7	3.67	7.94	6.03	1.35	1	--	--	4.32	-
Q_E	14	1.42	6.51	3.75	1.69	7	6.05	8.68	7.18	0.91	1	--	--	1.85	--
Q_G	14	1.40	2.89	2.12	0.46	7	0.59	2.54	2.05	0.69	4	0.23	0.88	0.65	0.29
β	14	1.12	9.11	3.38	2.58	7	0.56	1.09	0.86	0.19	1	--	--	2.34	-
α	14	0.15	0.71	0.45	0.20	7	0.74	1.09	0.85	0.13	1	--	--	0.48	-
X_w	14	9.5	24.1	14.7	4.0	7	11.7	28.2	18.9	5.2	4	7.8	21.7	13.7	6.3
T	14	8.7	15.8	12.1	2.6	7	7.4	15.7	11.1	2.9	4	2.5	10.2	5.9	3.3
u	14	3.2	7.7	5.1	1.4	7	3.7	5.8	4.3	0.8	4	2.6	4.1	3.4	0.7

N is the number of daylight periods.
Q^*, Q_H, Q_E and Q_G are in MJ m^{-2}.
β and α are dimensionless.
X_w, volumetric soil moisture (0-50 mm), is a percentage.
T is in °C.
u in m s^{-1}.

subsequent sections).

5.2.2 Low Q^* Days

The low mean Q^* for these four days, 7.4 MJ m^{-2}, was a consequence of cloud cover reducing t and the daily $K\downarrow$. The average daily t for the low Q^* days was only 0.330 .

The clouds on the low Q^* days were generally associated with precipitation. Over 26 mm of precipitation fell on the low Q^* days, approximately 70% of the total precipitation recorded during the experiment. During the periods of precipitation the air mass near the surface tended to be isothermal. These conditions resulted in the vertical differences in temperature and vapour pressure being less than the resolution of the differential psychrometer system. As a result, the partitioning of the available energy into Q_H and Q_E, using the BREB approach, for portions of July 13 and July 16-17 was not possible. The possibility of precipitation induced instrument damage prevented the use of the eddy correlation equipment on these days.

In general, it is assumed that daily Q_E was low (less than 3.0 MJ m^{-2}) on the low Q^* days. The main reasons for this assumption are the low amounts of available energy, and the small vapour pressure deficit (VPD) on these days. The VPD is a measure of the strength of the atmospheric sink for water vapour. It is the difference between the saturation vapour pressure and the actual vapour pressure as measured at a given height above the surface.

5.2.3 High Q^* days

As discussed in Chapter 4, high daylight Q^* values were associated with the generally fine weather and low amounts of cloud cover. These conditions were the norm for the experiment.

Table 5.2 shows that, apart from the categorization created differences in their Q_E and Q_H regimes, the meteorological conditions on both types of high Q^* day were quite similar. Both categories of days had similar Q^* and Q_G values, showing that the amount of available energy at the surface was the same for both categories of day. Windspeeds and air temperatures were slightly higher on the high β days. Statistical analysis of the data (Mann–Whitney U Test) supported the hypothesis that there was not a significant difference between the means of the daylight Q^*, Q_G, daily windspeeds and daily air temperatures for the two categories of high Q^* day.

The difference in the Q_E regimes for the two categories of high Q^* day, despite the similar amounts of available energy, air temperatures and windspeeds, is attributed to differences in the availability of surface moisture. The statistical analysis showed a high probability that volumetric soil moisture measurements from the 0–50 mm layer were higher on the low β days, as compared to the high β days. Further evidence for the limiting effect of surface moisture availability is found in the timing of the occurrence of the high Q^* and low β days. These days only occurred immediately after precipitation events.

Analysis of the energy balance regimes on individual days more clearly illustrates the effect of surface moisture availability on the Q_E regime.

5.2.4 Half-hourly Data for Selected Days

Five individual days were selected to illustrate the characteristics of the surface energy balance regime in more detail. The days are intentionally the same as those discussed in Chapter 4, with two exceptions. This facilitates the description of the relationships between the surface radiation and energy balances on these days. The days are June 27, July 25, July 6 and July 17–18. June 27 is discussed, rather than June 26, as a complete set of energy balance measurements was not made on June 26. July 6 is discussed, rather than July 10, because the data for July 6 is more representative of the energy balance regime during the dry conditions of the middle part of the experiment. The half-hour energy balance data for these days is presented in Figures 5.1 through 5.5. The half-hour daylight period r_a and VPD at 1.0 m above the surface are also presented in the figures. The VPD and r_a are included to illustrate the strength of the atmospheric sink for water vapour and the effectiveness of the turbulent exchange process on these days.

The energy balance regimes on June 27 and July 25 are considered typical of days with high daylight Q^* and relatively moist surface conditions. The half-hourly energy balance data for these days are presented in Figures 5.1 and 5.2. Both days fall into the high Q^* and high β category, with June 27 having a daylight Q^* value of 17.4 MJ m^{-2} and a β of 1.37. The respective values on July 25 were 16.0 MJ m^{-2} and 1.12.

The surface radiation regimes on June 27 and July 25 were similar. The weather was generally fine for both days and both days had a high daily t. The slightly higher Q^* total on June 27 is due to its slightly longer daylight period. Daily t was actually higher on July 25. June 27 was a predominantly cloudless day, with some cumulus clouds developing in the late afternoon, and a squally thunderstorm in the late afternoon and evening. The effect of the afternoon cloud on June 27 is well demonstrated in the period from 15:30 MDT to 17:30 MDT. Passing cloud in this period caused t to go from 0.796 to 0.461, then t returned to 0.784. As a result Q^* dropped from 500 W m^{-2} to 200 W m^{-2}, then increased to 450 W m^{-2}. The diurnal radiation regime on July 25 is described in Chapter 4.

The VPD and r_a regimes on both days are similar, with minor differences as a result of the thunderstorm on the afternoon of June 27, and the period of low windspeeds on the morning of July 25. As on other days, with small amounts of cloud cover, the VPD showed a steady increase through the morning, reaching a maximum in the early afternoon. The maximum VPD being associated with the maximum air temperatures. On

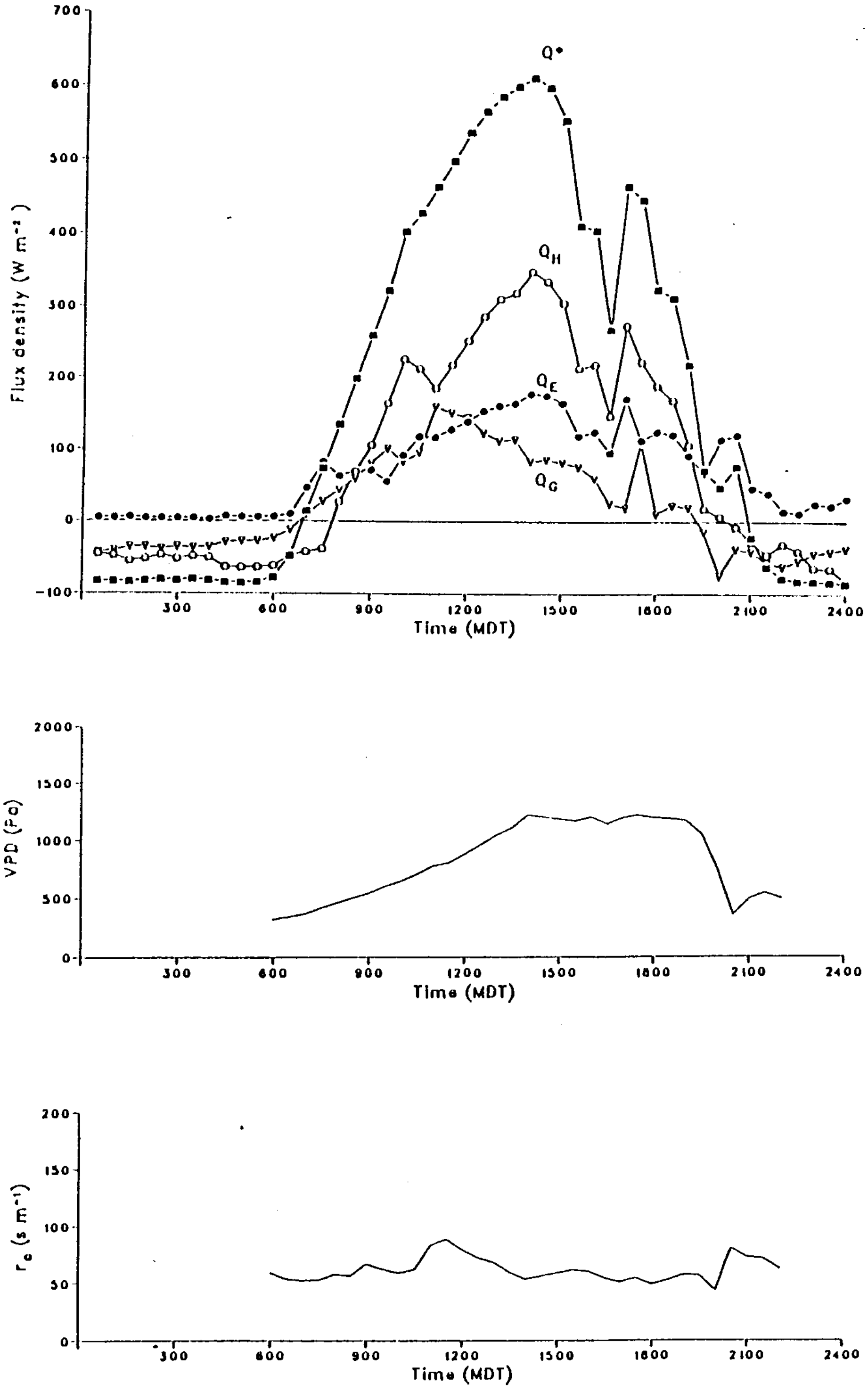

Figure 5.1. Half-hourly energy flux densities, VPD and r_a for a high Q* day on which the surface was relatively wet, June 27, 1985, Plateau Mountain.

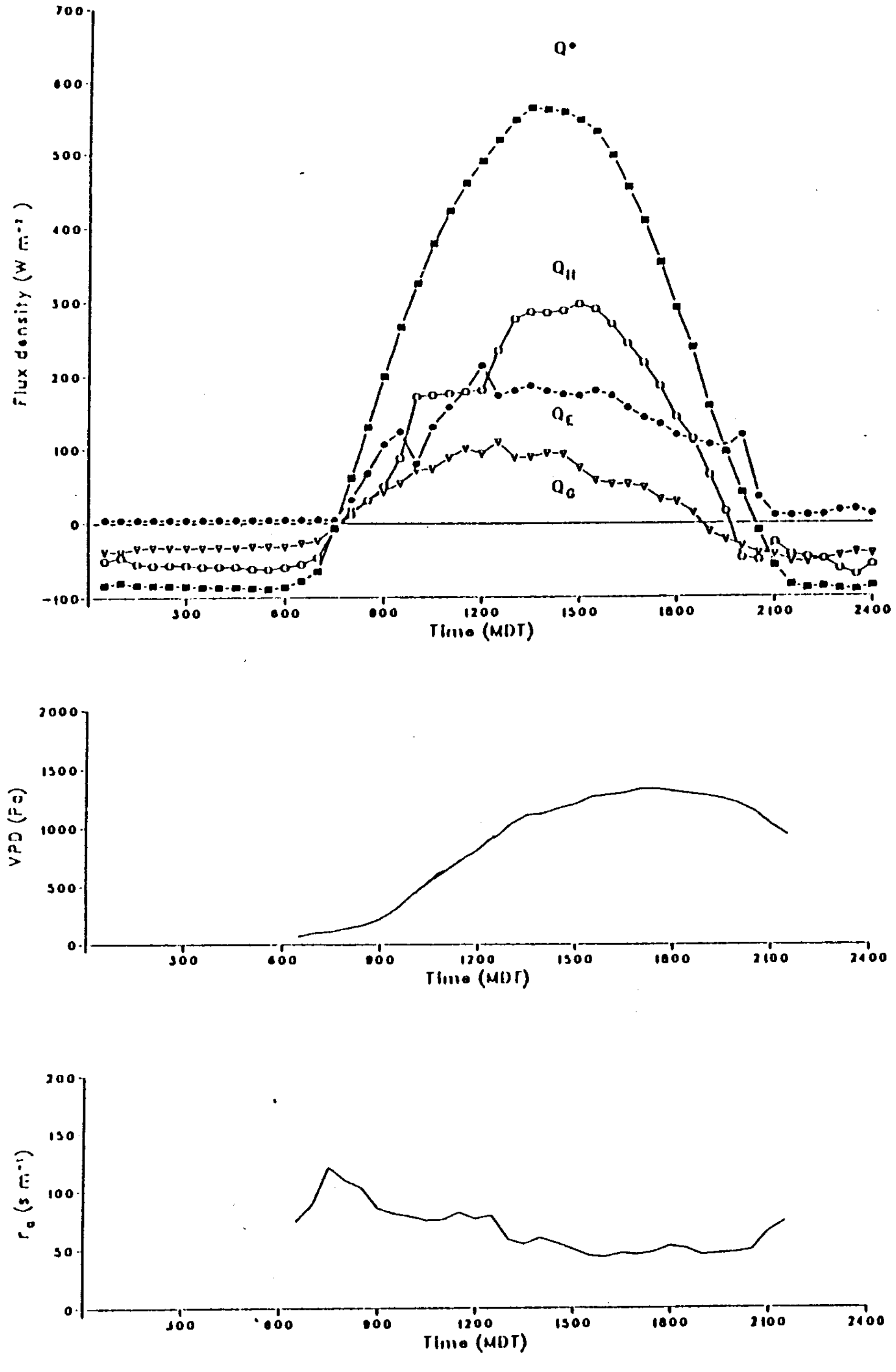

Figure 5.2. Half-hourly energy flux densities, VPD and r_a for a high Q* day on which the surface was relatively wet, July 25, 1985, Plateau Mountain.

June 27 the surface was still drying from the preceding precipitation and snowmelt. On July 25 the surface was still drying from the precipitation that fell on July 22-23.

The night period values illustrated in Figure 5.1 and 5.2 are typical of night period energy balance values during the experiment. As previously discussed, the night period energy balance fluxes showed little variation throughout the experiment, and were consistently small in magnitude.

On both days the morning increase in both Q_G and Q_E occurred coincidentally with the increase in Q^*. Q_H lagged behind, not showing a significant increase until an hour after Q^* became positive. This lag reflects the time required to reverse the nocturnal temperature inversion. After it began to increase, Q_H quickly outpaced the other components, tracking Q^* and reaching a maximum of 300–350 W m^{-2} at the same time that Q^* peaked at nearly 600 W m^{-2}. The Q_E curve has a flatter peak of less than 200 W m^{-2}. The larger amount of cloud cover on June 27 results in more fluctuations in the energy balance regime when compared to July 25. Figure 5.1 shows the characteristic lag in the response of Q_G to these cloud induced fluctuations in *t*.

The tendency of Q_E to experience a decline in it's rate of increase in the late morning, while Q^* and Q_H were still increasing rapidly, was a general characteristic of the energy balance regimes for most of the high Q^* days. There was considerable variation in this trend. Figure 5.2 shows Q_E approaching its maximum value before either the available energy maximum or the maximum VPD is achieved. This suggests that surface moisture availability had become the limiting control on Q_E. This "flattening" of the Q_E curve may reflect some physiological control by the surface vegetation over the movement of water to the surface, as suggested by Hatfield and Wanjura (1985). It probably also reflects an increase in the surface resistance, r_s, caused by the drying of the top few millimetres of the bare soil surface.

The thunderstorm between 19:30 MDT and 20:30 MDT on June 27 produced a small amount of rain and hail. The small increase in Q_E during this period is likely a result of this precipitation wetting the surface. However, it should be noted that in this evening period vertical temperature and vapour pressure gradients were very small, and the BREB approach was susceptible to large errors.

The energy balance regime on July 6, shown in Figure 5.3, is characteristic of a high Q^* and high β day during the middle part of the experiment. The daylight Q^* value on July 6 was 16.3 MJ m^{-2}, the daylight β was 4.04. This period was characterized by fine weather with no precipitation, and the site's surface was quite dry. Figure 3.11 shows that volumetric soil moisture measurements in the 0–50 mm layer were consistently less than 10% at this time.

July 6 was a nearly cloudless day, daily t was 0.750, and Figure 5.3 shows the characteristic Q^* curve expected on such a day. The curve is similar to those observed on June 26 and July 25. Q^* reached a maximum of over 600 W m^{-2} at solar noon on July 6.

In comparison to June 27 and July 25, Figure 5.3 shows that there was little lag in the response of Q_H to the increase in Q^* on the morning of July 6. The nocturnal temperature inversion was reversed more quickly than on the morning of those other days. Q_H tracked Q^* to reach a maximum of approximately 450 W m^{-2} at solar noon. Typically, during this dry period, Q_E was low. Figure 5.3 shows that for most of the daylight period of July 6, Q_E did not exceed Q_G. The characteristic "flattening" of the Q_E curve is very pronounced. Q_E increased slowly, reaching a flat topped peak of approximately 100 W m^{-2} before solar noon, then decreasing to near its nocturnal minimum by 16:30 MDT.

Surface moisture availability is clearly a limiting factor on the Q_E regime on July 6. Despite increasing amounts of available energy, a

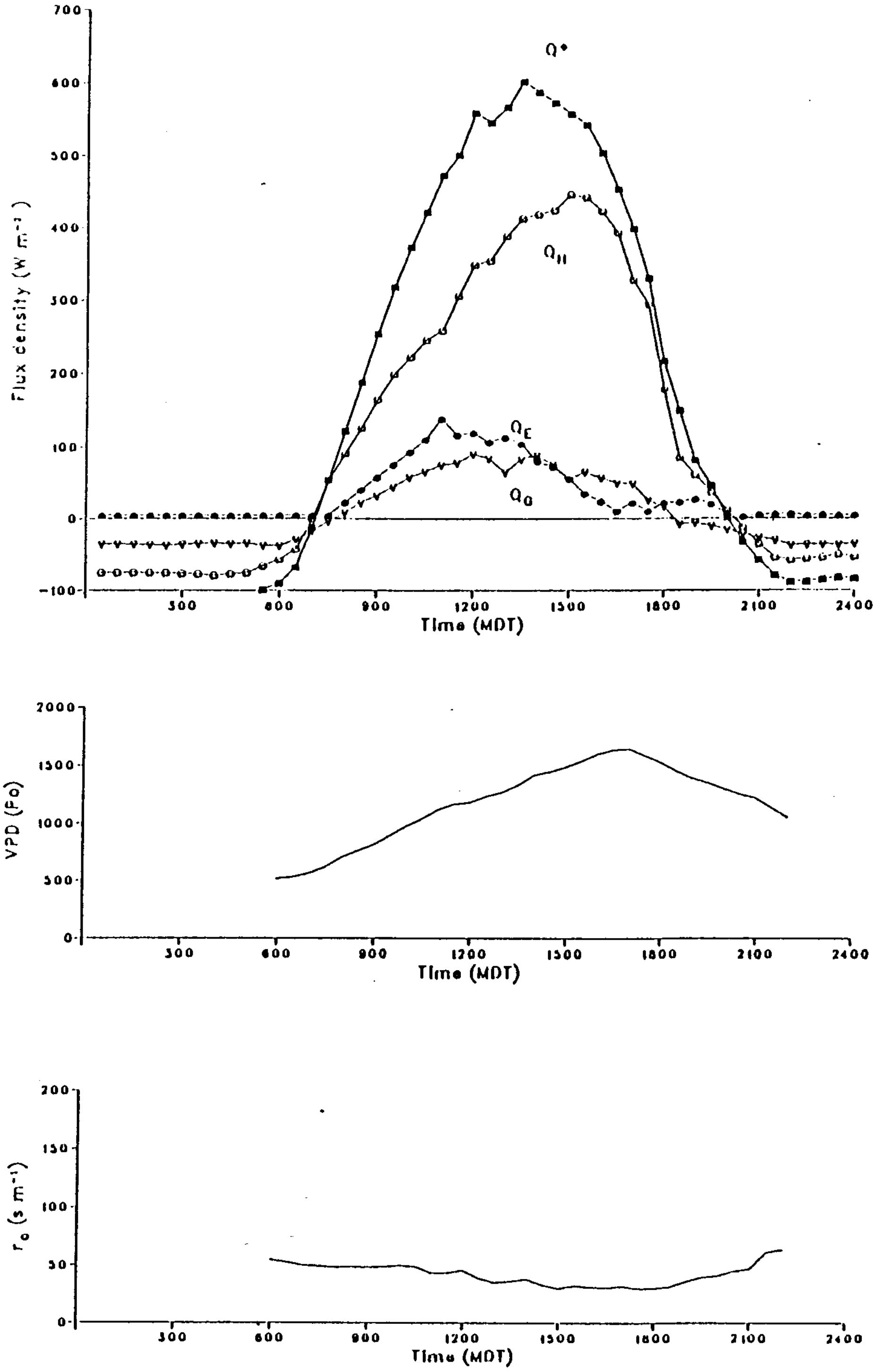

Figure 5.3. Half-hourly energy flux densities, VPD and r_a for a high Q* day on which the surface was dry, July 6, 1985, Plateau Mountain.

pronounced VPD, and low r_a, Q_E decreased throughout the late morning and afternoon.

The energy balance data for July 17-18, presented in Figures 5.4 and 5.5, illustrates the conditions during the latter part of the rain and snowstorm that occurred on July 17, and on the subsequent fine day, July 18. The energy balance regime on July 17 is an example of a low Q^* day, the daylight Q^* value was 6.3 MJ m^{-2}. The surface energy balance regime on July 18 is an example of a high Q^* day (16.9 MJ m^{-2}) with a low daylight β of 0.678.

As noted in Chapter 4, the heavy cloud cover on the morning and early afternoon of July 17 reduced *t* and resulted in low Q^* values for most of the day. Q^* did not exceed 150 W m^{-2} until after 15:00 MDT, when clearing skies resulted in cloudy-bright conditions and Q^* fluctuated widely. The low Q^* values and the snowcover on the morning reduced surface heating, and Q_G did not become positive until 12:30 MDT. The isothermal nature of the airmass near the surface, and snow induced instrumentation problems, made it impossible to determine Q_H and Q_E using the BREB approach on the morning and early afternoon of July 17. For the latter part of the afternoon and evening, it was possible to use the BREB approach. Figure 5.4 shows that in this late afternoon period Q_E generally exceeded Q_H.

Figure 5.4 shows that there was no VPD at 1 m above the surface until 16:00 MDT . The lack of an atmospheric sink for water vapour would have minimized any evaporation up until this time.

The cloudless morning of July 18 saw a rapid increase in Q^* shortly after sunrise. As on June 27 and July 25, Q_E and Q_G increased coincidentally with Q^*, while Q_H lagged behind the other components. Unlike those other days, Q_E was greater than Q_H for almost all the daylight period. Q_H peaked at approximately 260 W m^{-2} between 12:30 MDT and 13:00 MDT, and Q_E peaked at approximately 270 W m^{-2} at the same time. Q_H, Q_E and Q_G all

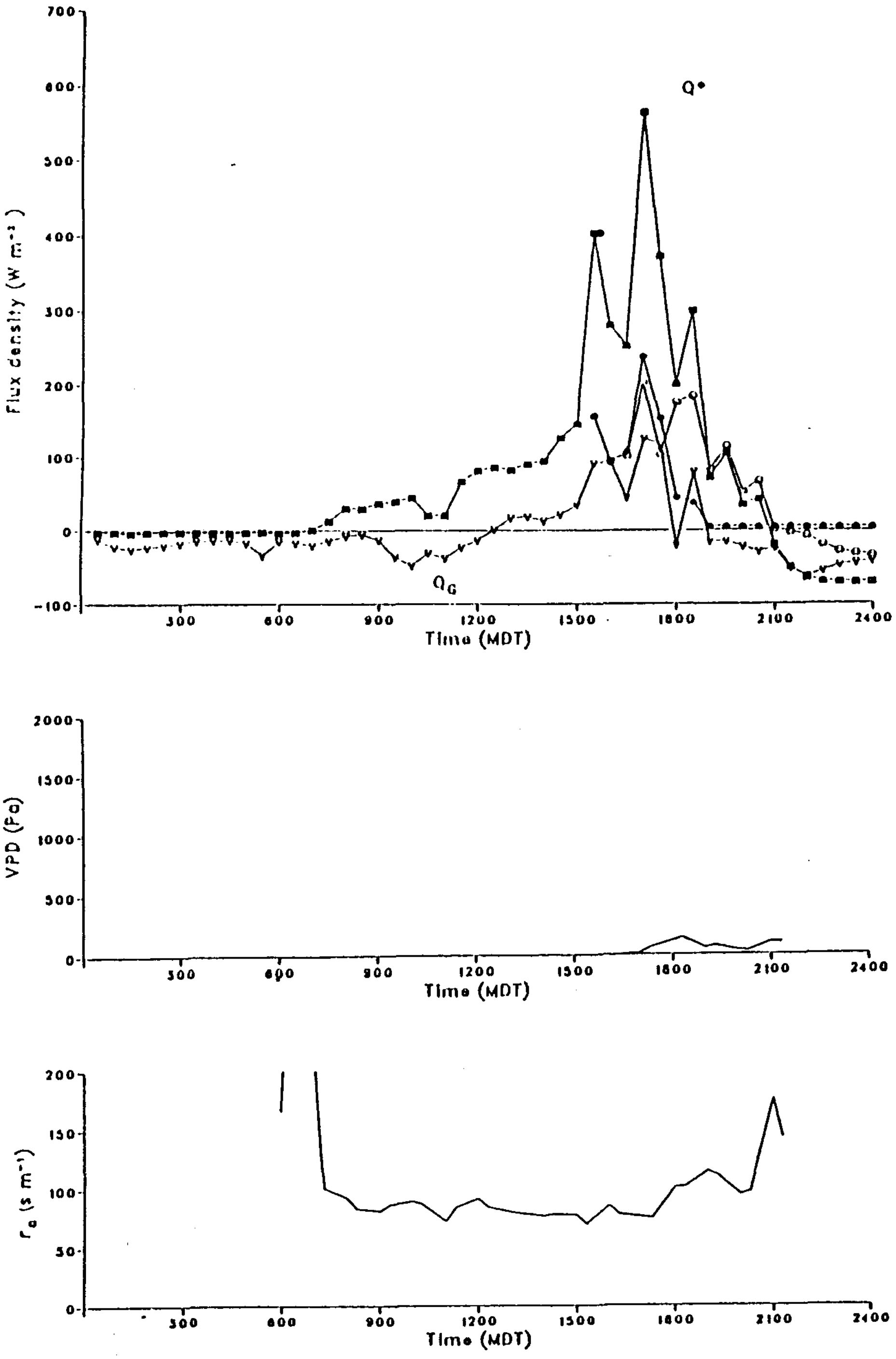

Figure 5.4. Half-hourly energy flux densities, VPD and r_a during the latter part of snowstorm and subsequent clearing conditions on July 17, 1985, Plateau Mountain.

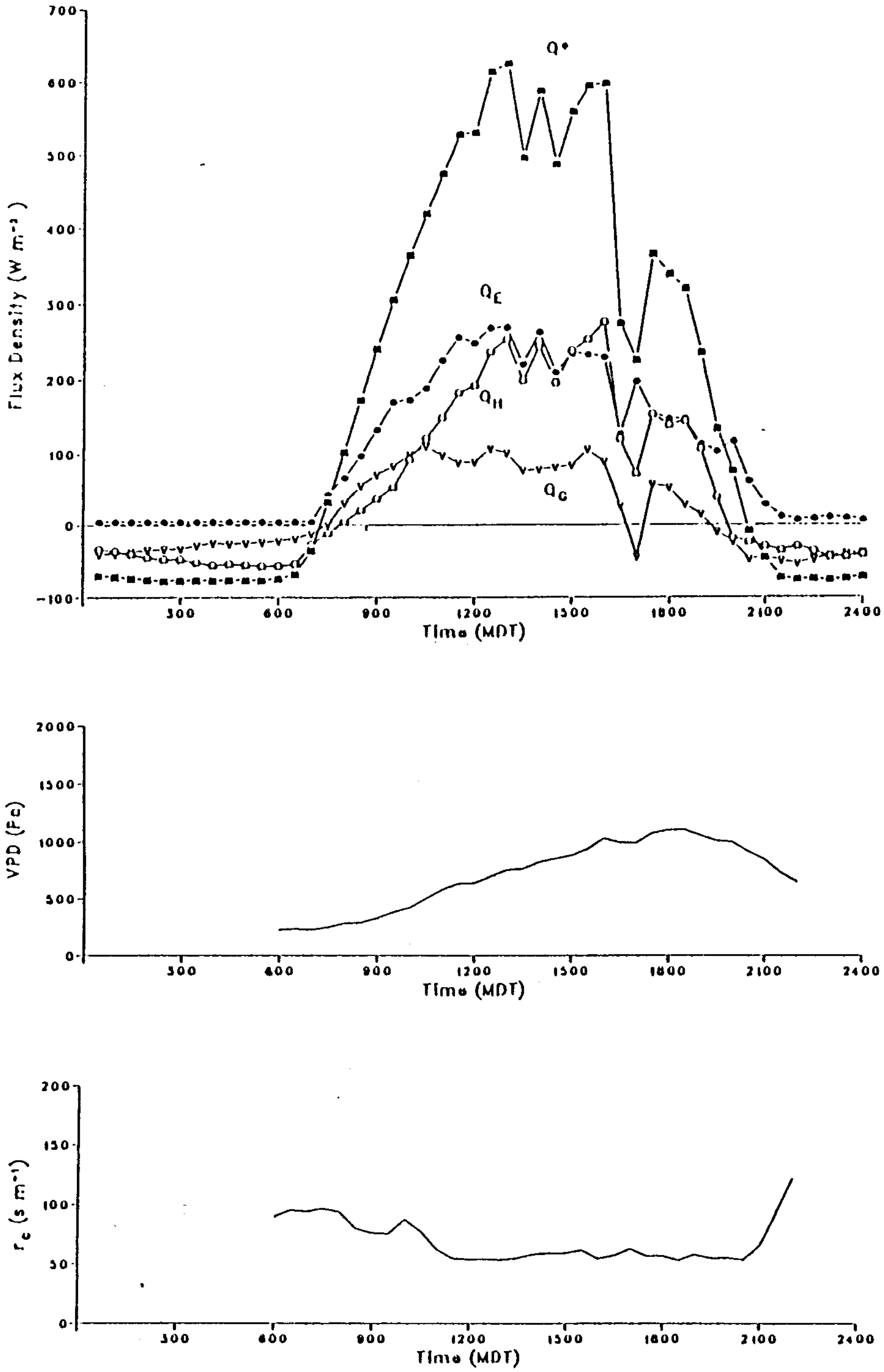

Figure 5.5. Half-hourly energy flux densities, VPD and r_a for a high Q* day on which the surface was wet, July 18, 1985, Plateau Mountain.

show fluctuations as a result of the increase in cloud cover between 12:00 MDT and 18:00 MDT . The particulary large decreases between 16:00 MDT and 17:00 MDT are the result of the decrease in t caused by cloud cover.

In Figure 5.5 there is little evidence of Q_E being limited by the availability of surface moisture, and Q_E closely tracks Q^* over the entire daylight period. Interestingly, the daylight period α for July 18 was only 0.96, considerably less than the α_{PT} value of 1.26. The failure of α to approach α_{PT} indicates that evaporation did not occur at its potential rate on July 18. This is somewhat surprising, given that July 18 was preceded by several days with significant precipitation. The value of 0.96 was the highest daylight period α recorded during the period of the experiment. In contrast, α for the daylight period on July 6 was 0.30.

5.2.5 Soil Heat Flux and the Temperature Regime at the Surface and in the Near Surface Zone

Daylight period Q_G was consistently between 10–15% of the daylight Q^*. Figures 5.1 through 5.5 show that this relationship held true for the half-hourly values, with Q_G closely tracking Q^*.

In Figure 5.6 all half-hourly (daylight and night) Q_G values are plotted against the coincident Q^* values. Figure 5.6 confirms that Q_G was essentially a constant proportion of Q^*. This is attributed to a lack of variation in the soil thermal conductivity over the course of the experiment. As discussed in Section 3.3.8, soil thermal conductivity will vary primarily due to changes in soil moisture content. The limited range of soil moisture conditions in the 0–50 mm layer during the experiment resulted in small variations in soil thermal conductivity.

Figure 5.6 also confirms that Q_G was consistently low in magnitude, with almost all the half-hourly

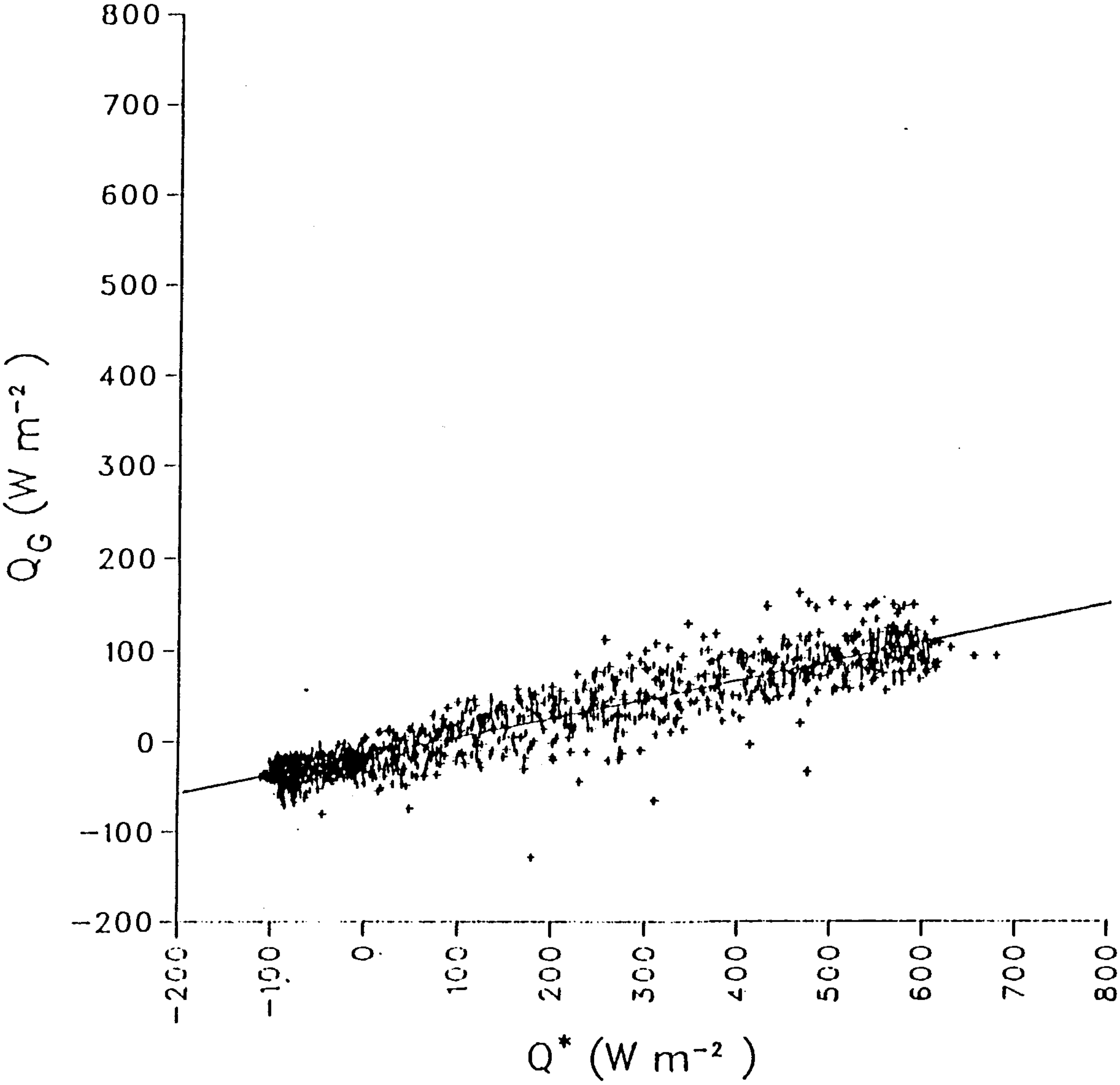

Figure 5.6. Half-hourly Q^* vs. Q_G, June 26 – July 26, 1985, Plateau Mountain.

Q_G values lying between 100 W m^{-2} and -100 W m^{-2}.

The generally positive daily Q_G values resulted in an increase in soil temperatures throughout the experiment. The mean temperature at 0.5 m below the surface was approximately 2° C on June 26, and on July 26 it was 8° C. The amplitude of the diurnal fluctuation of soil temperature was almost totally dampened at 0.5 m below the surface. The mean surface temperature data presented in Table 3.3 shows a similar slightly increasing trend for the experiment period, as does the mean air temperature at 1.0 m above the surface.

The slight increase in the mean temperature of the near surface air and soil was greatly exceeded by the diurnal range of temperatures in the near surface zone.

In Figures 5.7 and 5.8 the soil and air temperature profile data for July 25 are presented. July 25 was selected as an example because cloudless conditions eliminated the temperature fluctuations that ocurred when *t* fluctuated. The data in the Figures 5.7 and 5.8 is typical of a fine day during the experiment. Earlier in the experiment temperatures would have been slightly lower, and the curves in the figures would have been shifted slightly lower.

The soil temperature data shows the characteristic increase in the amplitude of the diurnal fluctuation of soil temperature at decreasing soil depths. At 0.50 m below the surface the amplitude of the diurnal fluctuation is almost totally dampened. The fluctuation is greatest at the surface. At the surface temperatures ranged from an early morning low of 3° C, to a mid-day high of 33° C.

The large diurnal fluctuations in the temperature of the top 0.05 m of the soil were an important consideration in the determination of Q_G. Typically, in the morning and evening over 50% of Q_G consisted of the

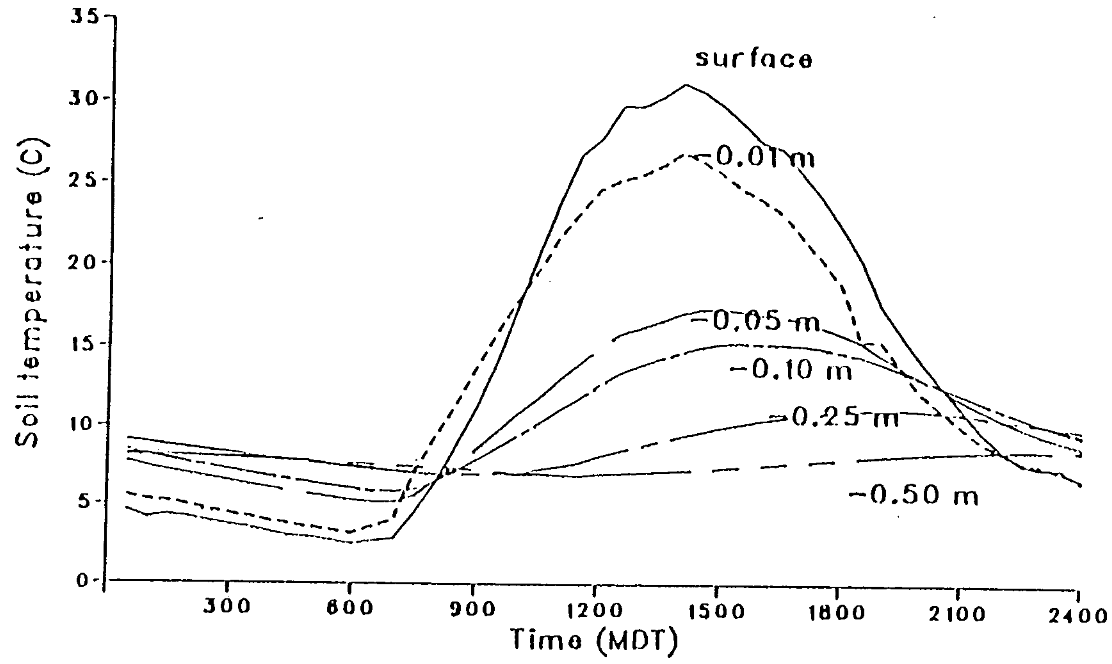

Figure 5.7. Soil temperatures at the surface, 0.01, 0.05, 0.10, 0.25 and 0.50 m below the surface, July 25, 1985, Plateau Mountain.

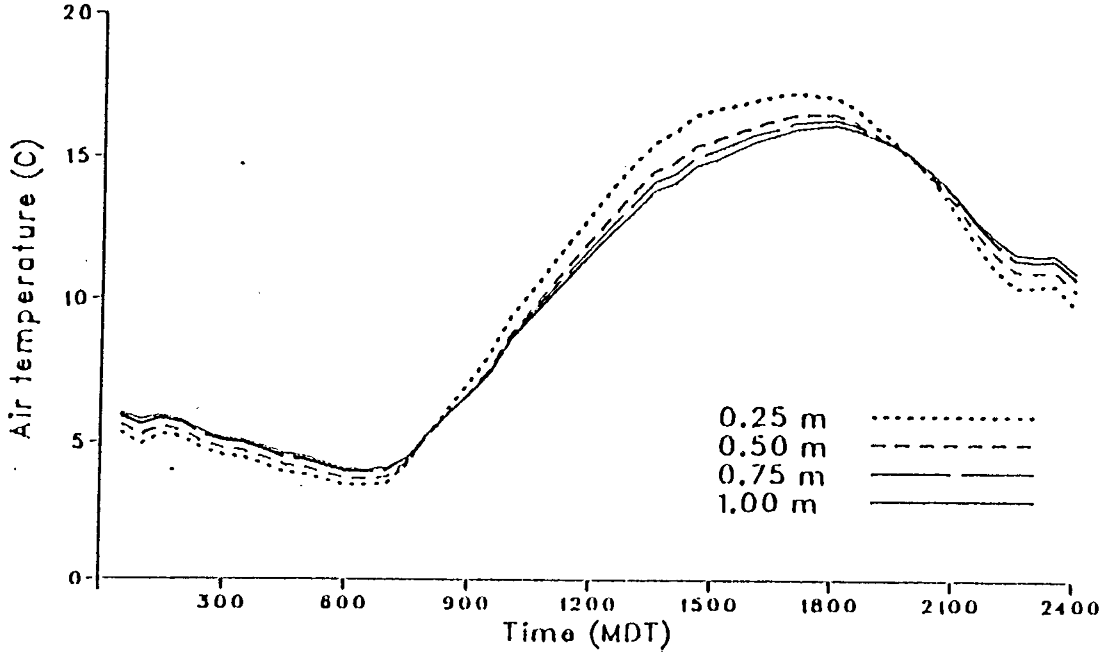

Figure 5.8. Air temperatures at 0.25, 0.50, 0.75 and 1.00 m above the surface, July 25, 1985, Plateau Mountain.

energy being used to raise or lower the temperature of the top 0.05 m layer of soil. In terms of equation 2.11, in the morning and evening Q_{Gz} was often equalled or exceeded by the surface heat flux divergence term. Failure to account for temperature changes in the top 0.05 m of soil would have resulted in considerable error in the determination of Q_G.

Figure 5.8 shows that air temperatures also underwent considerable diurnal variation, with air temperatures at 0.25 m ranging from 5° C in the early morning to 17° C in the mid-afternoon. Larger diurnal variations in air temperatures must have occurred between the surface and 0.25 m. The small vertical temperature gradients that occurred in the morning and evening are also apparent in the Figure 5.8.

5.2.6 Surface Resistance

Given the persistently large amounts of moisture in the soil at depths greater than 0.20 m, and the observed limiting influence of surface moisture on Q_E on most days, it is suggested that the surface and top layer of soil at this site restricted the movement of water from the sub-surface to the atmosphere. Several factors are believed to be responsible. First, for the non-vegetated portions of the surface the very porous non-consolidated nature of the alpine soils limits the capillary movement of water from the sub-surface to the surface. At the same time this soil type is very effective at moving liquid water from the surface to the sub-surface. Second, the strong thermal gradients in the soil during the daylight period would result in a strong water vapour flux, within the soil pores, away from the surface Third, for much of the vegetated portion of the surface, mat plants provide a barrier between the sub-surface and the atmosphere, exerting both a physical and a physiological control over the movement of water to the atmosphere. This latter factor is supported by the observed dampness under the mat plants during the dry period in the middle of the experiment. It is hypothesized that this combination of factors resulted in a general surface resistance to the movement of water from the soil to the atmosphere, and that this resistance became greater as conditions became drier.

As noted in Section 2.8.1, the combination model can be used as a diagnostic tool to quantitatively describe surface resistance. Half-hourly surface resistance, r_s, values were calculated using the half-hour Q_E values determined using the BREB approach, the measured Q^* and Q_G, the T and e values at 1 m above the surface, and the calculated r_a values.

The hypothesis that surface resistance at this site increased as the surface became drier was supported by the calculations of r_s. Mid-afternoon half-hourly r_s values ranged from 200 - 500 s m^{-1}. The higher values were observed on the days when the surface was dry. This range of values was similar to that observed by Ripley and Redmann (1976) at a semi-arid grassland site during the summer in Saskatchewan, Canada.

The trends of half-hourly r_s over the daylight periods of June 27, July 25, July 6 and July 18 are shown in Figures 5.9 - 5.12. In all four figures the difficulty of determining r_s in the early morning and late evening is apparent. This difficulty is primarily attributable to the difficulty in using a residual approach to determine r_s, when Q^*, Q_G and Q_E are small. In the following discussion of the figures the large fluctuations in r_s prior to 08:00 MDT and after 20:00 MDT are disregarded. On the moderately wet-surface days, June 27 and July 25 (Figures 5.9 and 5.10), and the wet-surface day, July 18 (Figure 5.12), r_s was low in the morning and increased to a maximum value in the mid-afternoon. Similar trends have been observed in the calculated canopy resistances of forest and agricultural crops (Szeicz and Long 1969; Tan and Black 1976; Gash and Stewart 1975; Bailey and Davies 1981b). In the agricultural and forest environments the increase in surface resistance throughout the daylight period has been related to the physiological response of vegetation to environmental parameters eg. VPD and solar irradiance. For this alpine tundra site there also appears to be a large

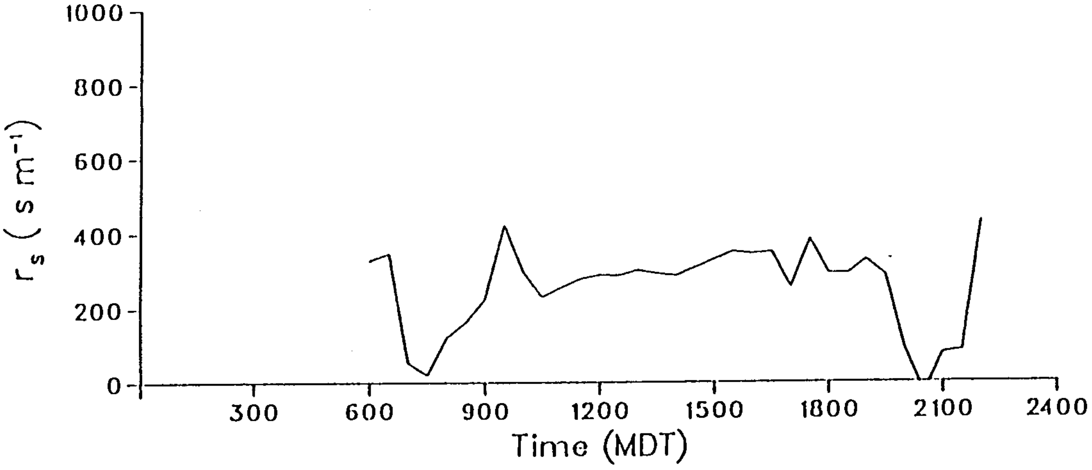

Figure 5.9. Calculated half-hourly r_s for June 27, 1985, Plateau Mountain.

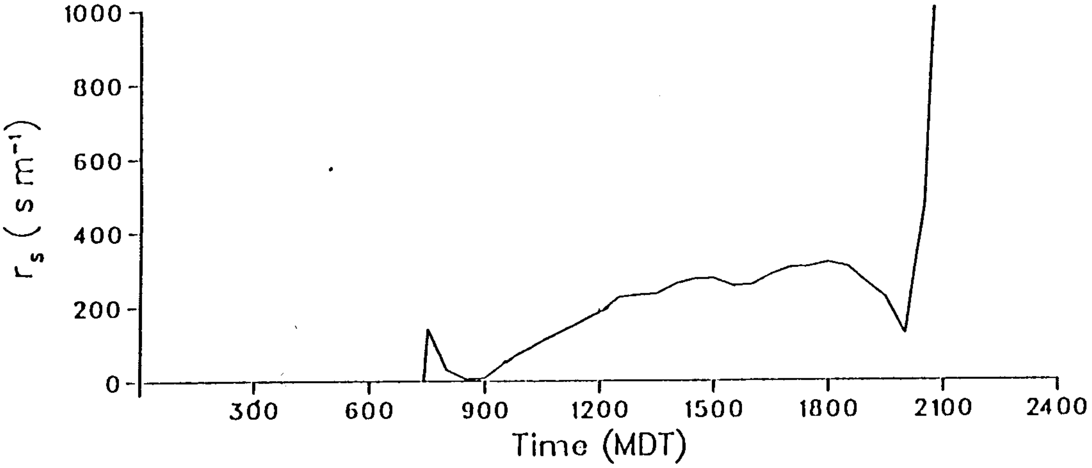

Figure 5.10. Calculated half-hourly r_s for July 25, 1985, Plateau Mountain.

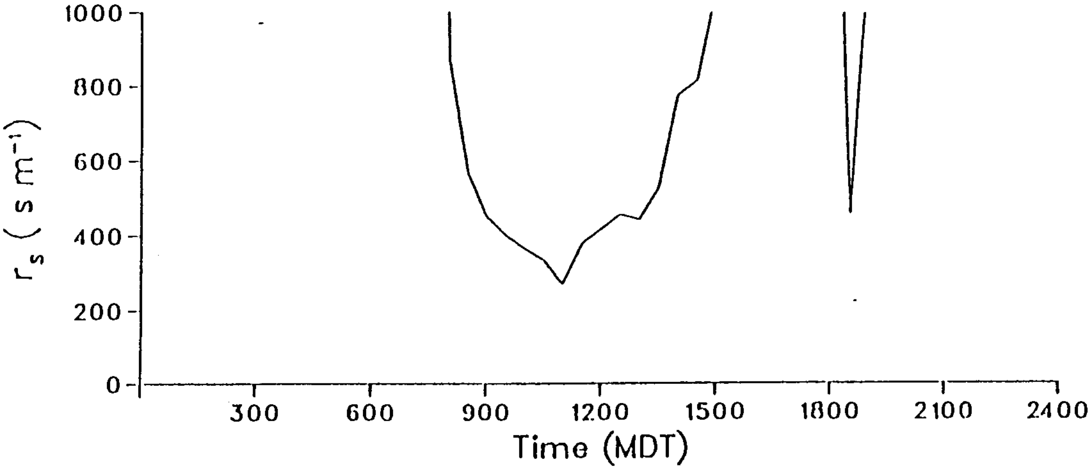

Figure 5.11. Calculated half-hourly r_s for July 6, 1985, Plateau Mountain.

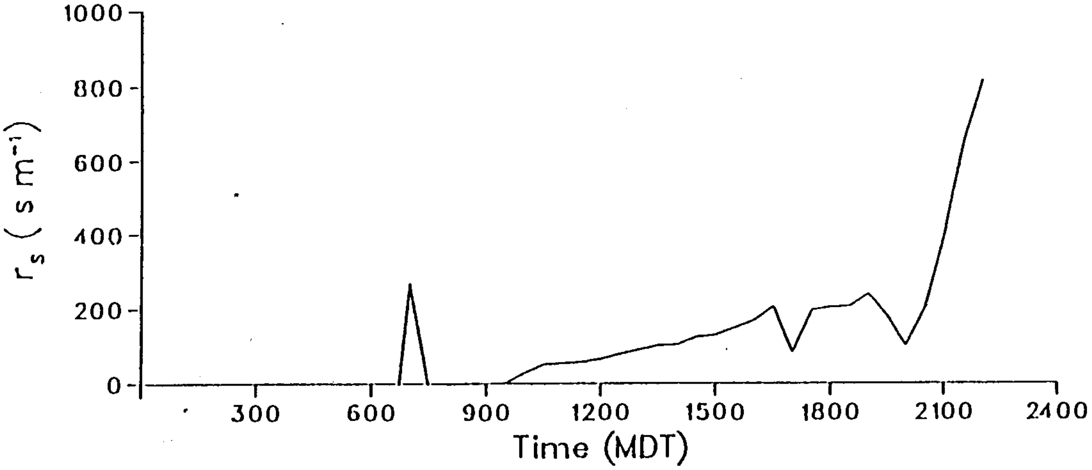

Figure 5.12. Calculated half-hourly r_s for July 18, 1985, Plateau Mountain.

physiological element in the surface resistance. Direct measurement of the stomatal resistance of the surface vegetation would be necessary to demonstrate this conclusively. Ripley and Redmann (1976) suggest that low surface resistances in the morning may be partially attributable to the re-evaporation of condensation. This may be the case with the data from Plateau Mountain, and would explain the very low surface resistances on the morning of July 18.

The trend of r_S on the dry-surface day, July 6 (Figure 5.11), is different from the other days. r_S decreases from a morning high of >1000 s m^{-1} to a mid-morning low of approximately 500 s m^{-1}, and then increases to greater than 1000 s m^{-1} by early afternoon. Ripley and Redmann (1976) present similar data for a dry surface day at their grassland site. Oke (1978) suggests that "U" shaped surface resistance curves will occur when there is no condensation in the morning and the surface resistance is primarily a function of the physiologic response of vegetation to increasing light intensity.

It is apparent from the results, for both the wet and dry-surface days, that the tundra surface at Plateau Mountain exercised a dynamic and variable control over the movement of water to the atmosphere. It seems that a large element of this surface control was physiological in origin.

5.2.7 Summary of .the Daily Energy Balance Regime

The daylight period energy balance values for the experiment are presented in Figure 5.13. From Chapter 4 and the preceding sections, it is apparent that the major controls on the energy balance at Plateau Mountain were the amount of available radiative energy at the surface, and the availabilty of surface moisture, which affected the partitioning of the available energy into Q_E and Q_H. The following discussion reviews the daily surface energy balance regime during the experiment in terms of these factors.

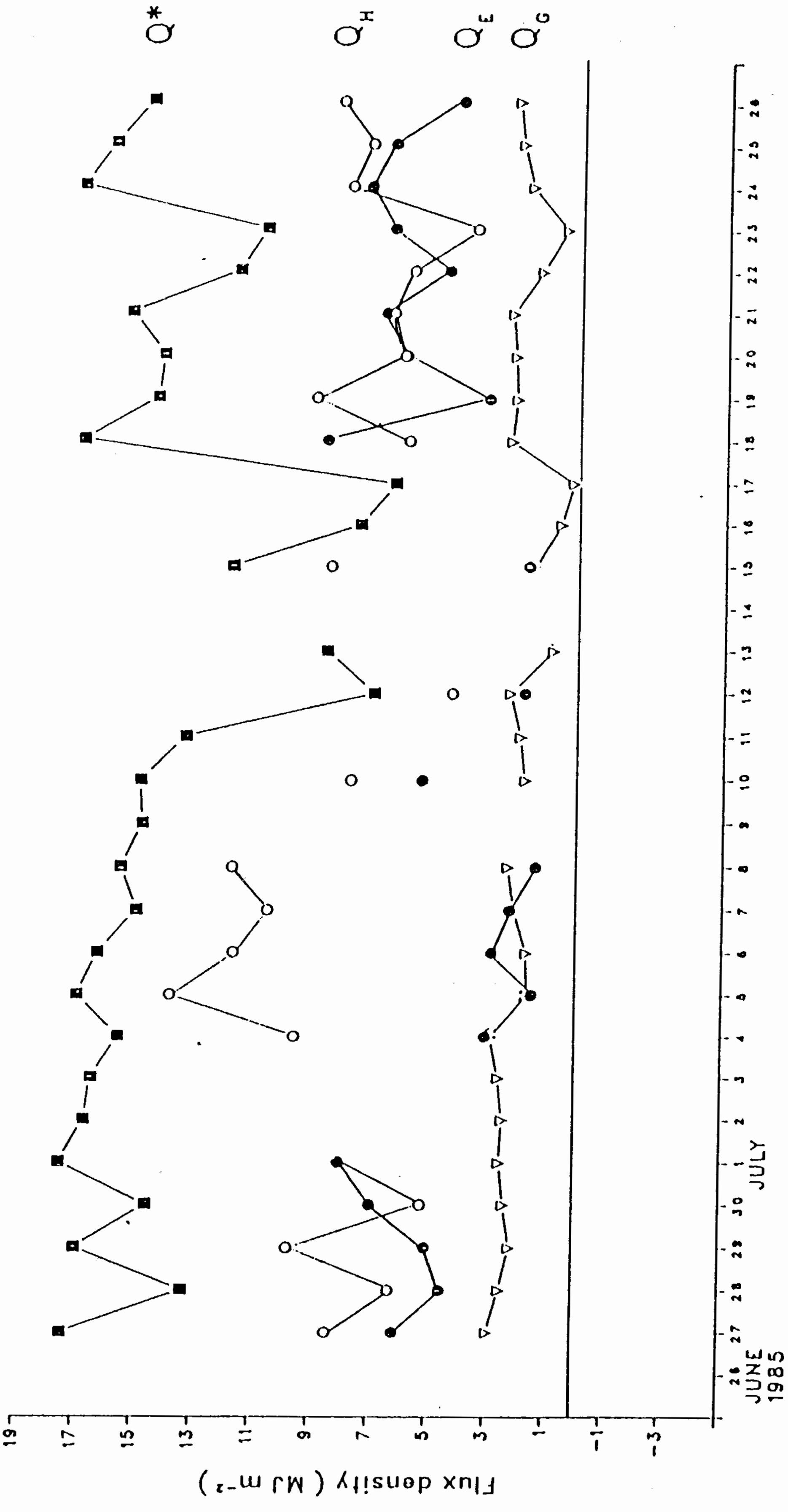

Figure 5.13 Daily energy balance component flux densities, Plateau Mountain, June 26 - July 26, 1985.

The period June 26 – July 1 was a drying period, with the surface still wet from previous precipitation and snowmelt. The measured daily Q_E in this period translated to evaporation rates of 2–4 mm per day. Daylight α values ranged from 0.54 to 0.87. Surface drying during this period was slowed by some recharge from the afternoon and evening thunderstorms. The 0.8 mm of precipitation recorded on June 30 fell between 15:00–15:30 MDT and the rest of the afternoon was characterized by cloudy-bright conditions. This precipitation on the afternoon of June 30 resulted in a relatively wet surface, and low β values for that afternoon and the morning of July 1.

Instrumentation difficulties prevented the partitioning of the available energy on July 2–3. These were high Q^* days, and it is assumed that dry surface conditions resulted in low Q_E values on these days, similar to those recorded on July 4.

The period from July 2 – 15 was characterized by fine weather, on only two occasions did Q^* fall below 10.0 MJ m^{-2}, and only a trace of precipitation was recorded. Figure 3.11 shows that volumetric soil moisture in the 0–50 mm layer was quite consistently at 10% throughout this period. The energy balance regime on July 6 was typical of the high Q^* days during this period. Surface moisture availability clearly limited Q_E and evaporation rates seldom exceeded 1.0 mm per day. The vertical differences in vapour pressure became very small in this period causing difficulties in the use of the BREB approach. Values of less than 0.20 were consistently observed for α during this period. The small amounts of precipitation on July 10 and July 13 did not wet the surface enough to significantly alter the surface energy balance regime.

A storm began on the night of July 15, and continued through July 16–17 resulting in heavy cloud cover and precipitation. July 18 was clear, particularly in the morning, resulting in a high Q^* total for the day. The surface was wet from the previous day's precipitation and snowmelt, resulting in a low β value for the day. The second highest daylight α value during the experiment (0.96) was observed on July 18. The Q_E total on July 18 translated to an evaporation rate of nearly 4 mm per day.

July 18–21 appears to be a drying period, after the storm. The low Q_E values on July 19 are surprising, and can not be explained in terms of available energy or surface moisture. The mean windspeed on July 19 (3.2 m s^{-1}) was below the experiment average, and the wind blew primarily from the east, as opposed to the more characteristic southwest. These factors may have resulted in an unusually large advective element in the energy balance regime on July 19.

Cloud cover reduced daily t on July 22–23, although the daylight period values remained slightly greater then 10 MJ m^{-2}. On these two days 6.5 mm of precipitation fell. These days were followed by nearly cloudless sky conditions. for July 24–27. This was another drying period, as shown by the steadily increasing β.

5.3 Comparison of Sensible Heat Flux Densities Determined Using the Eddy Correlation and Ohm's Law Approaches with Those Measured Using the BREB Approach

5.3.1 Introduction

In this section the values from the two other approaches used to determine Q_H during the experiment, the eddy correlation and the Ohm's law approaches, are compared with the Q_H values measured using the BREB approach. To simplify the discussion, Q_H as determined by the eddy correlation and Ohm's law approaches will be referred to respectively as Q_H(EC) and Q_H(OL). The BREB determined values will continue to be referred to simply as Q_H.

As discussed in Chapter 2, there is an element of uncertainty in accounting for bluff-body effects, surface roughness and atmospheric stability effects in the Ohm's law approach. The sensitivity of the approach to errors in the estimation of these elements is discussed in this section.

5.3.2 Eddy Correlation Determined Sensible Heat Flux Densities

In Figure 5.14 the 303 half-hourly daylight period Q_H(EC) values are plotted against the concurrently determined Q_H values. A statistical comparison of the measurements is presented in Table 5.3.

Figure 5.14 and the high index of agreement (d = 0.944) presented in Table 5.3 show that there was extremely good agreement between the two techniques. The good agreement between these two independent measurement techniques, for the portions of the experiment during which they were operated concurrently, supports a high degree of confidence in the Q_H measurements made over the course of the entire experiment.

For the 303 cases the average difference between Q_H and Q_H(EC) was ±51.0 W m^{-2}. If analysis is restricted to the 250 cases for which Q_H exceeded 25 W m^{-2}, the average difference between Q_H and Q_H(EC) was ±33.2% of Q_H. This difference is not much larger than the relative measurement error associated with Q_H, as measured using the BREB approach (measurement error associated with the BREB approach is discussed in Appendix 2). For smaller Q_H values, the average magnitude of the relative differences between Q_H and Q_H(EC) was considerably larger. The larger magnitude of the relative differences is considered to be primarily a function of the difficulty of determining Q_H, when Q_H is small.

The apparent tendency of Q_H(EC) to be greater than Q_H values is shown by the positive mean bias error (MBE) of 33.1 W m^{-2}. Figure 5.14 suggests that this tendency was more pronounced when Q_H was large. Given the probable error of the BREB approach, it would be difficult to determine if

Table 5.3. Comparison of daylight period half-hourly Q_H values determined using eddy correlation and Ohm's law approaches with those determined using the BREB approach, Plateau Mountain, June 26 - July 26, 1985.

		Linear regression coefficients[1]				Measures of difference[2]			
	N[3]	r^2	Std. error ($W\ m^{-2}$)	a ($W\ m^{-2}$)	b	MBE ($W\ m^{-2}$)	RMSE ($W\ m^{-2}$)	Std. dev. of differences ($W\ m^{-2}$)	d
Q_H(EC)	303	0.873	55.1	9.3	1.136	33.1	66.4	57.7	0.944
Q_H(OL)	804	0.876	46.0	-4.96	0.852	-25.0	56.4	50.6	0.957
	(303)	(0.848)	(50.2)	(-8.7)	(0.933)	(-20.3)	(54.6)	(50.8)	(0.955)
Q_H(OL)	804	0.876	51.2	-5.5	0.951	-12.2	53.1	51.7	0.965
z_0 plus 50%.	(303)	(0.849)	(55.9)	(-9.6)	(1.041)	(-2.5)	(56.0)	(56.1)	(0.959)
Q_H(OL)	804	0.876	38.8	-4.2	0.719	-43.3	70.1	55.9	0.925
z_0 minus 50%.	(303)	(0.848)	(42.4)	(-7.3)	(0.788)	(-44.3)	(66.9)	(56.2)	(0.919)
Q_H(OL)	804	0.877	46.0	-4.6	0.855	-24.3	55.9	50.4	0.958
No stability correction.	(303)	(0.851)	(50.0)	(-8.5)	(0.938)	(-19.3)	(54.0)	(50.6)	(0.956)
Q_H(OL)	804	0.873	61.1	-7.2	1.120	8.5	63.8	63.3	0.958
r_{am} substituted for r_a.	(303)	(0.841)	(67.2)	(-12.0)	(1.217)	(25.8)	(76.9)	(72.6)	(0.937)
Q_H(OL)	804	0.874	61.1	-6.8	1.120	9.6	64.1	63.4	0.957
r_{am} substituted for r_a. No stability correction.	(303)	(0.844)	(66.9)	(-11.8)	(1.225)	(27.4)	(77.5)	(72.7)	(0.937)

[1] The linear regression coefficents are based on the regression of the model predicted Q_H on the measured Q_H. a is the Y axis intercept, b is the slope of the regression line. In all cases, t test scores indicated a greater than 99.9% probability that $b \neq 0$.

[2] The measures of difference, as described by Fox (1981) and Willmot (1982), are based on the differences between the model predicted Q_H and the measured Q_H. MBE is the mean bias error, RMSE is the root mean square error and d is the index of agreement.

[3] N refers to the number of half-hour periods for which values were available. Comparisons are based on both the total available daylight period data set (804 cases) and the data set for the period when the eddy correlation equipment was operated (303 cases).

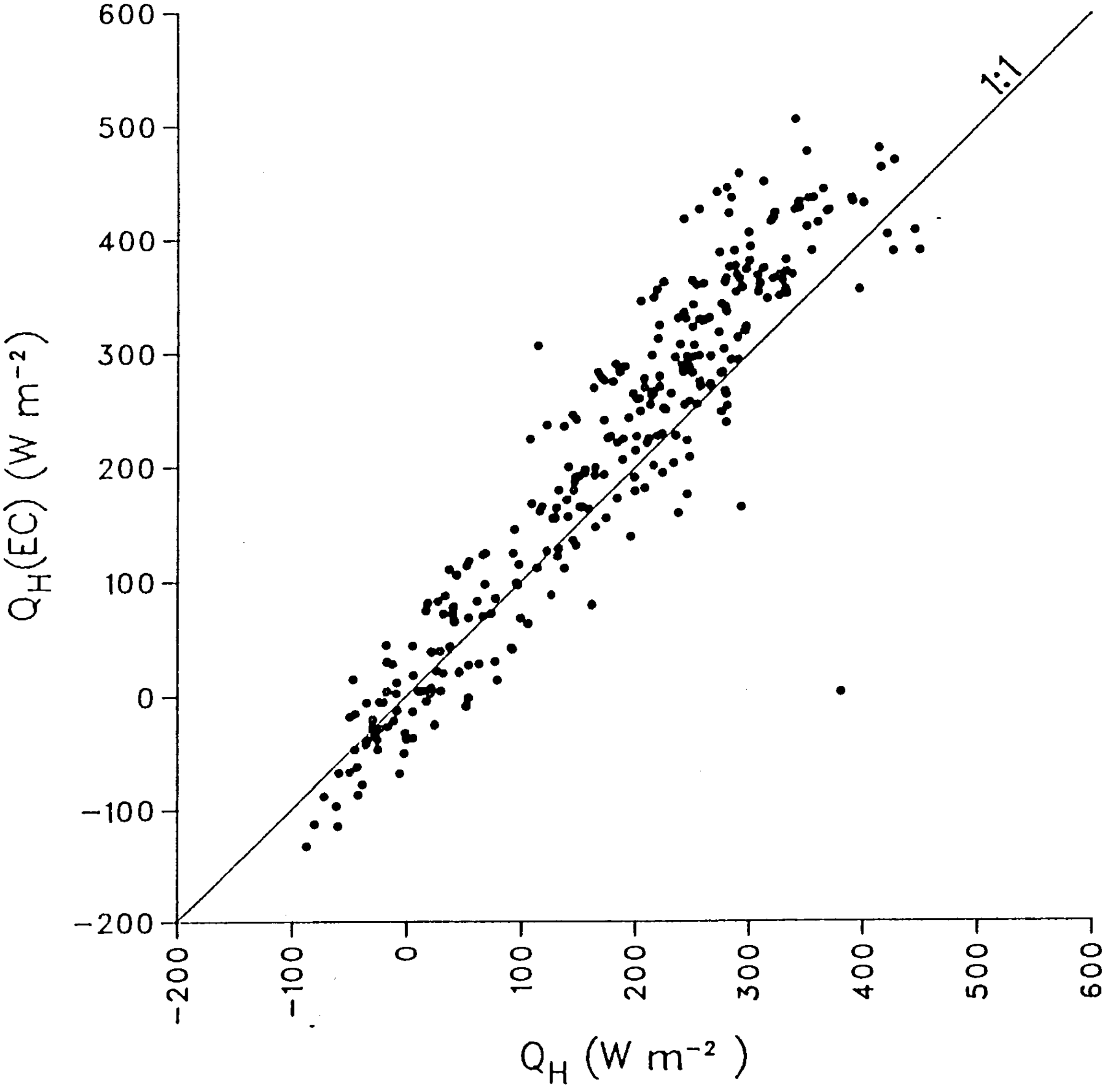

Figure 5.14. Comparison of half-hourly measurements of Q_H made using the eddy correlation approach with those measured using the BREB approach, June 26 – July 26, 1985, Plateau Mountain.

this bias truly represents a systematic difference between the approaches.

In Figures 5.15 and 5.16 the daylight period half-hourly Q_H and Q_H(EC) values for the dry surface day, July 6, and the wet surface day, July 18, are presented. The eddy correlation equipment was not operated after 16:00 MDT on July 6. The figurés illustrate the good agreement between the two measurement techniques throughout both daylight periods. The apparent tendency of Q_H(EC) to be slightly greater then Q_H is seen in both figures.

5.3.3 Ohm's Law Approach Determined Sensible Heat Flux Densities

In Figure 5.17 the 804 concurrent daylight period half-hour Q_H and Q_H(OL) values are compared. A statistical comparison of the results is presented in Table 5.3.

Figure 5.17, and the index of agreement (d = 0.957) presented in Table 5.3, show that there was excellent agreement between the two approaches. The average difference between Q_H and Q_H(OL) for the 804 cases was ±40.1 W m^{-2}. If analysis is restricted to the 573 cases for which Q_H exceeded 25 W m^{-2}, the average difference between Q_H and Q_H(OL) was ±31.1% of Q_H. As with the Q_H(EC) values, the relative difference was considerably larger for smaller values of Q_H.

The MBE of −25.0 W m^{-2} shows that there was a slight tendency for Q_H(OL) to be less than Q_H. Figure 5.17 shows that this tendency prevailed over the entire range of Q_H values, and was not more pronounced at greater or lower values. As with the Q_H(EC) values, this apparent bias fell within the range of error associated with the BREB approach so that it would be difficult to determine if this truly represents a systematic difference.

Table 5.3 shows that if analysis is restricted to the 303 cases where concurrent Q_H, Q_H(EC) and Q_H(OL) values are available, Q_H(OL) continues to display good agreement with Q_H. The MBE and RMSE and index of agreement remain essentially the same as for the larger data set. This similarity

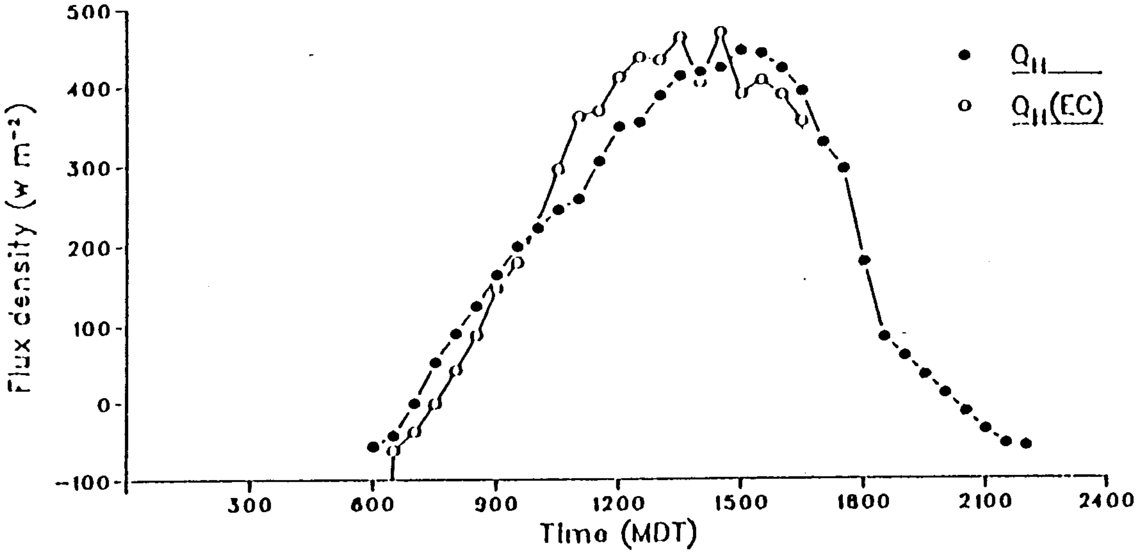

Figure 5.15. Half-hourly daylight Q_H and Q_H(EC), July 6, 1985, Plateau Mountain.

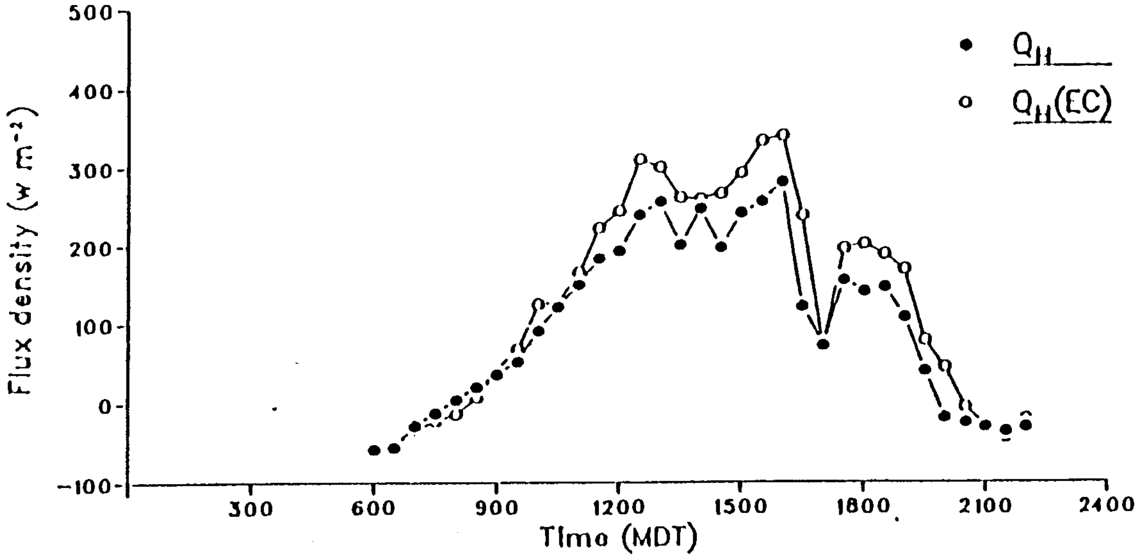

Figure 5.16. Half-hourly daylight Q_H and Q_H(EC), July 18, 1985, Plateau Mountain.

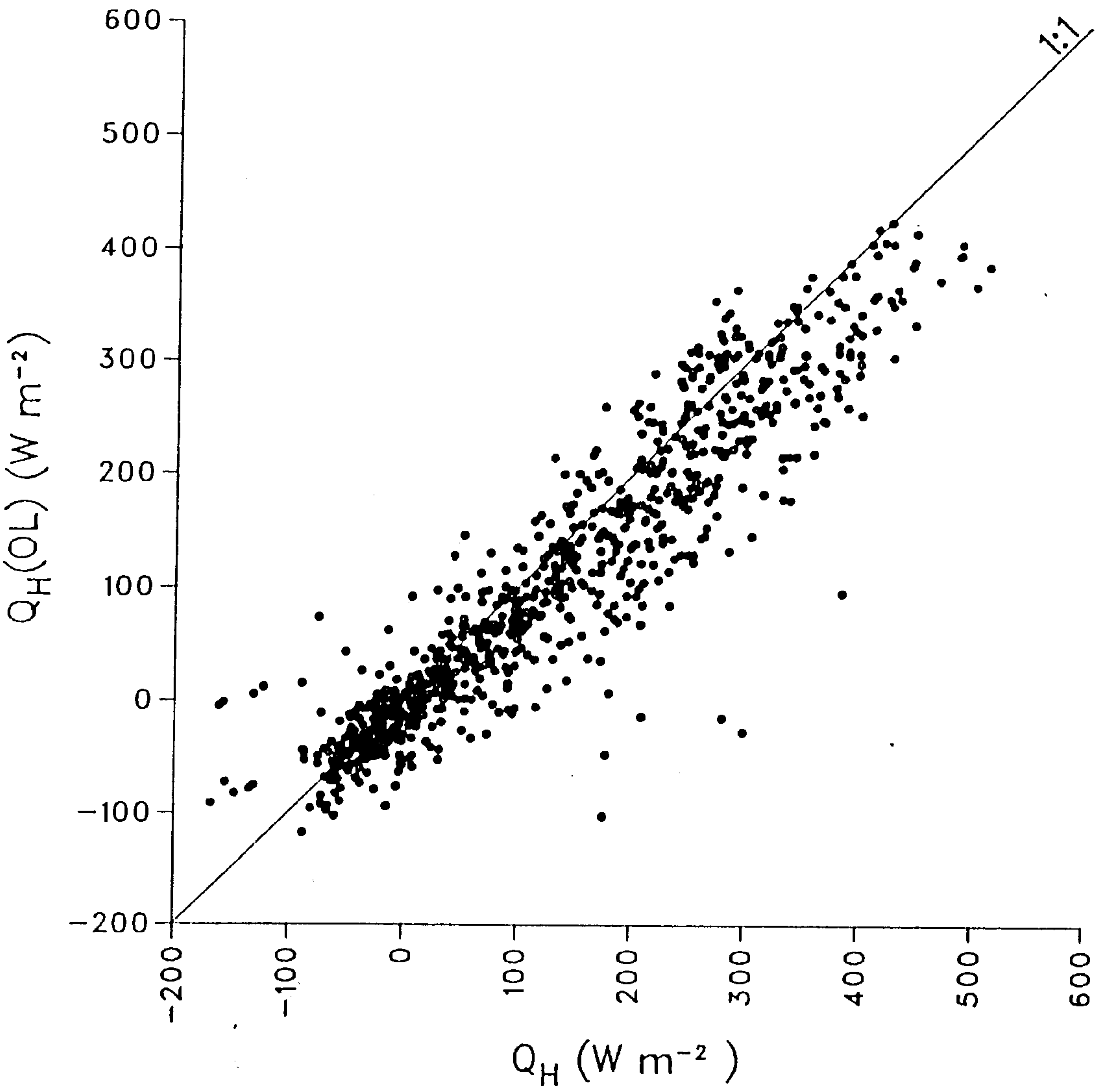

Figure 5.17. Comparison of half-hourly values of Q_H determined using the Ohm's law approach with those measured using the BREB approach, June 26 – July 26, 1985, Plateau Mountain.

confirms that the differences in agreement between Q_H and Q_H(EC), and Q_H and Q_H(OL), are the result of differences in the measurement approaches, rather than the conditions that prevailed during the periods when the different measurement techniques were being employed.

In Figures 5.18 and 5.19 the daylight period half-hourly Q_H and Q_H(OL) values for the dry surface day, July 6, and the wet surface day, July 18, are presented. On both days the agreement between the two approaches is excellent, with the slight tendency of Q_H(OL) to be less then Q_H apparent in both figures.

5.3.4 Sensitivity of the Ohms' Law Approach to Uncertainty in the Estimation of z_0 , r_b and ϕ_M

The Ohm's law approach for determining Q_H is not only susceptible to errors arising from the measurement of T_0, but is also affected by uncertainty regarding the parameterization of surface roughness, bluff-body effects and the effects of atmospheric stability. If small errors in the estimation of these parameters can be shown to result in large errors in the determination of r_a, it can be argued that the reliance of the approach on the empirical determination of important parameters reduces its general applicability. Alternatively, if the procedure is relatively insensitive to errors in these parameters, its value as both a measurement technique, and as a basis for modelling Q_E is enhanced. In the following discussion the effect of uncertainty regarding z_0, r_b and ϕ_M on r_a, and Q_H(OL) is discussed.

In Figure 5.20 r_a, as determined using z_0 = 2.1 mm, is plotted against u at 1.0 m. In addition the r_a values resulting from an error of ±50% in z_0 are plotted. The figure shows that the effect of the ±50% error generally resulted in a ±10% error in r_a. The figure further shows that the sensitivity of r_a to uncertainty in z_0 decreases as u increases.

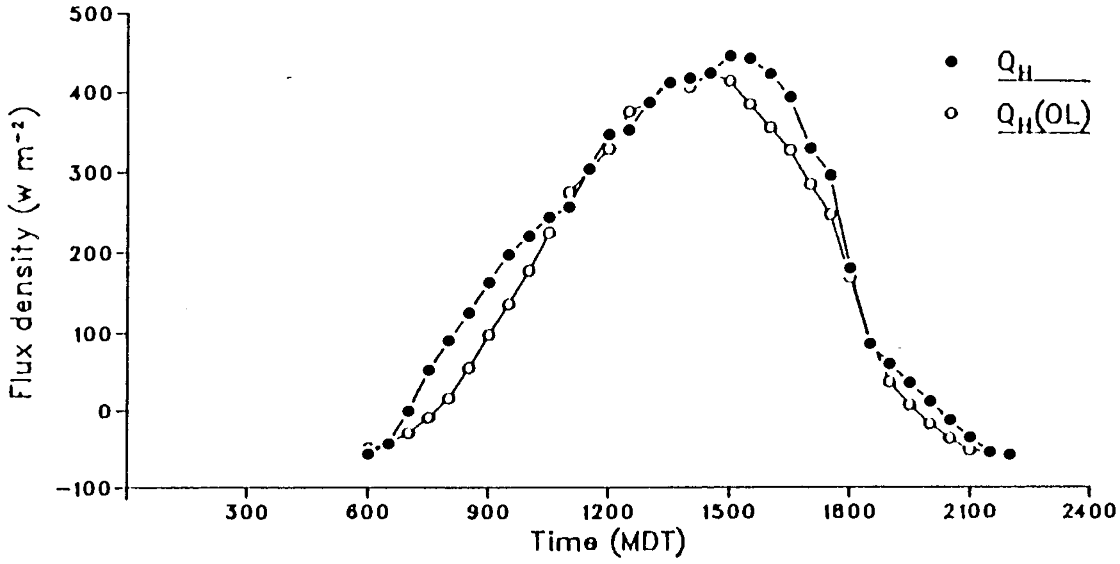

Figure 5.18. Half-hourly daylight Q_H and $Q_H(OL)$, July 6, 1985, Plateau Mountain.

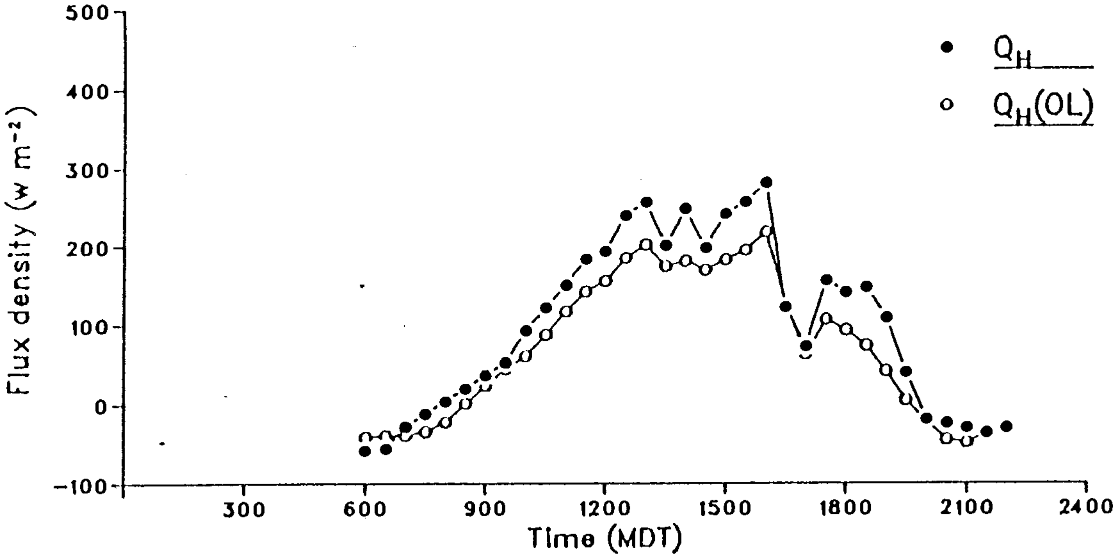

Figure 5.19. Half-hourly daylight Q_H and $Q_H(OL)$, July 18, 1985, Plateau Mountain.

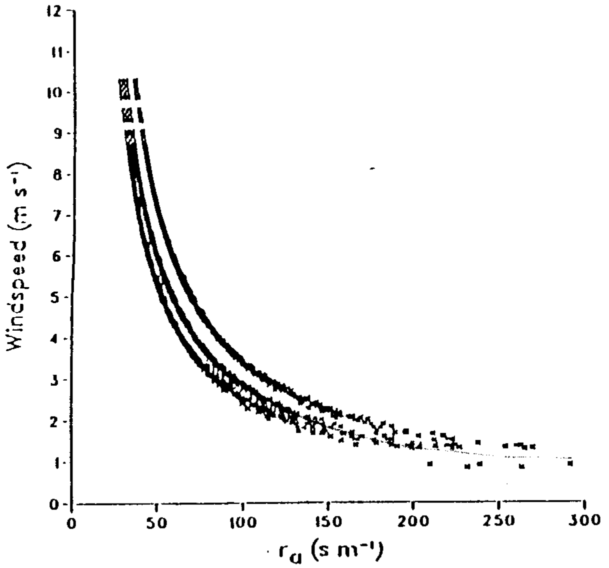

Figure 6.20.

Half-hourly r_a vs. windspeed, June 26 – July 26, 1985, Plateau Mountain. r_a values were calculated assuming the determined z_o value of 2.1 mm, and assuming an error of ±50% in z_r.

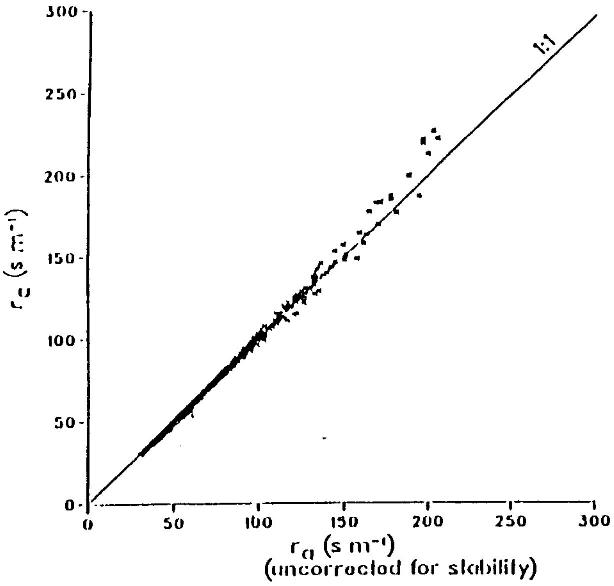

Figure 6.21.

Half-hourly r_a vs. non-stability corrected r_a, June 26 – July 26, 1985, Plateau Mountain

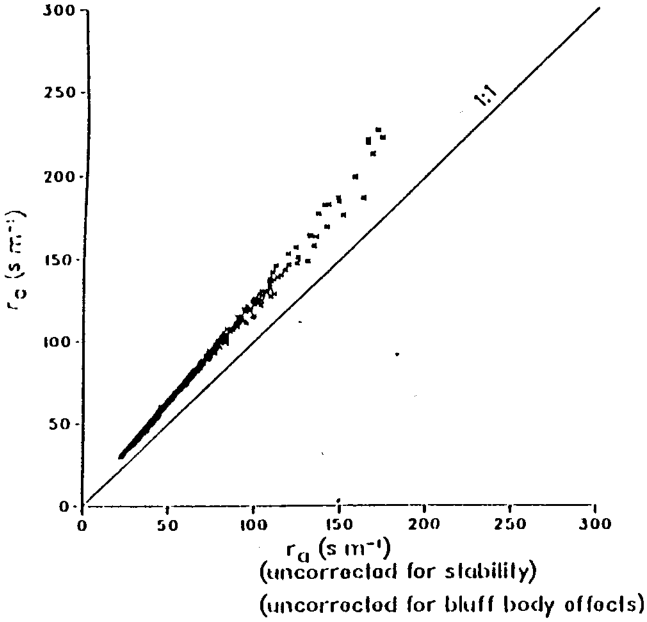

Figure 6.22.

Half-hourly r_a vs. r_{am}, June 26 – July 26, 1985, Plateau Mountain

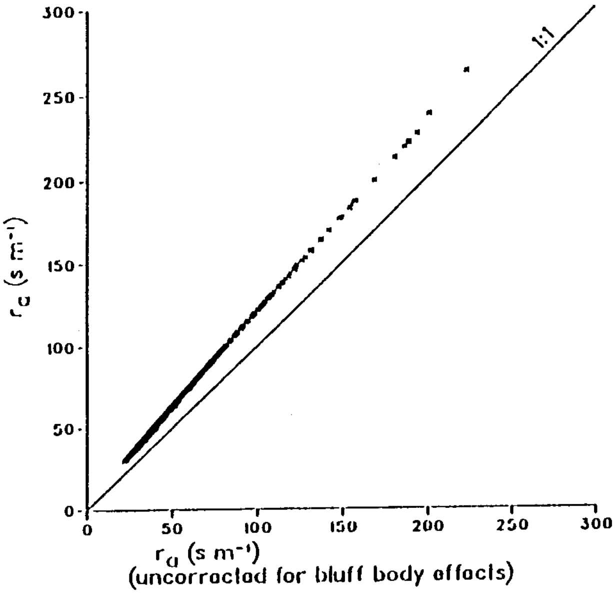

Figure 5.23.

Half-hourly r_a vs. non-stability corrected r_{am}, June 26 – July 26, 1985, Plateau Mountain

Table 5.3 summarizes the effect the ±50% error in z_0 would have on the the determination of Q_H(OL), as compared to Q_H. The high z_0 value actually counters the previously noted tendency of Q_H(OL) to be less then Q_H, while the low z_0 value accentuates this apparent bias. In both cases the resultant Q_H(OL) values are on average within 70 W m^{-2}, or 10% of the Q_H values.

In Figure 5.21, r_a is compared with a calculated aerodynamic resistance value which was determined without accounting for atmsopheric stability effects (non-stability corrected r_a). In Figure 5.22, r_a is compared with a calculated aerodynamic resistance value which was determined without accounting for bluff-body effects (r_{am}). In Figure 5.23, r_a is compared with a calculated aerodynamic resistance which was determined without accounting for either atmospheric stability or bluff-body effects (non-stability corrected r_{am}). The results of using these three values, non-stability corrected r_a, r_{am} and non-stability corrected r_{am}, as substitutes for r_a in the determiniation of Q_H(OL), as compared to Q_H, are summarized in Table 5.3.

Failure to account for atmospheric stability clearly has only a slight effect on the determination of r_a and r_{am}, and the resultant Q_H(OL) values. As was noted in Section 2.7.2, Bradley (1972), has shown that this is to be expected for unstable conditions, when the measurements of air temperature and windspeed are made close to the surface. Failure to account for bluff-body effects in the determination of Q_H(OL) counters the tendency of Q_H(OL) to be less than Q_H. In all cases, the average difference between Q_H and Q_H(OL) is approximately 50 W m^{-2}, and within the probable range of error associated with the BREB approach.

In general, the aerodynamically smooth nature of the tundra surface, the high windspeeds, and the ability to make windspeed and air temperature measurements close to the surface at this site reduced the sensitivity of the Ohm's law approach to errors in z_0, r_b and ϕ_M. As these conditions are likely to exist at other alpine tundra locations, the Ohm's law approach seems well suited for the measurement of Q_H at such locations.

5.4 Approaches for Modelling Latent Heat Flux Density

5.4.1 Introduction

In this section, the results of using a combination of the energy balance and the Ohm's law approach (equation 2.42) for modelling half-hourly Q_E, and the potential for using an equilibrium evaporation based approach (equation 2.47) to model daylight period Q_E are discussed. These models were investigated primarily to test the concept of applying these techniques to the alpine tundra environment. Obviously the lack of a comparable data set for a similar alpine location precludes the possibility of testing the robustness and general transferability of these models.

5.4.2 Estimation of Available Energy at the Surface

Both models require an estimate of the available energy at the surface, as described by $(Q^* - Q_G)$. As such information is not often readily available, it is desirable to incorporate a means for estimating $(Q^* - Q_G)$ into the models. For this thesis, an objective and independent method of determining $(Q^* - Q_G)$ has the added benefit of making the model results more independent of the test data set.

To develop an expression for predicting daylight period $(Q^* - Q_G)$ two assumptions were made. Firstly, it was assumed that the empirical expression suggested by Davies (1967), and discussed in Chapter 4, could be used as a predictor of Q^*. Secondly, on the basis of the measurements made at Plateau Mountain and those reported elsewhere, it was assumed that daylight period Q_G could be reasonably estimated as 10% of Q^*. This resulted in the following expression for daylight period $(Q^* - Q_G)$

$$Q(\text{model}) = 0.553\ K\downarrow - 1.11\ (\text{MJ m}^{-2}\ \text{d}^{-1}), \tag{5.1}$$

where Q(model) is the estimated ($Q^* - Q_G$).

An expression for half-hourly values was developed by assuming that the Davies expression could be extended to half-hourly data. This was done by reversing the procedure suggested by Davies and Idso (1979) for converting relationships based on hourly or half-hourly data to be used as predictors for longer periods (this procedure was discussed in Section 2.3). Assuming a mean daylight period length of 15.5 hours, and that half-hourly Q_G was 10% of Q^*, this resulted in

$$Q(\text{model}) = 0.553\ K\downarrow - 19.9\ (\text{W m}^{-2}). \tag{5.2}$$

5.4.3 An Energy Balance - Ohm's Law Approach for Modelling Half-hourly Latent Heat Flux Densities

The measured half-hourly T_0, measured half-hourly T at 1 m above the surface, the stability corrected r_a used to determine Q_H(OL), and estimated Q(model) term were used as input for equation 2.42 to produce half-hourly estimates of Q_E, which will be referred to as Q_E(EBOL). In Figure 5.24 the half-hourly Q_E(EBOL) are compared with the daylight period half-hourly Q_E. Estimates were also made using the model with measured Q^* and Q_G, and substituting a non-stability corrected r_{am} value for r_a. A statistical comparison of the Q_E(EBOL) values with the BREB measured Q_E values is presented in Table 5.4. In Figures 5.25 - 5.28 the daylight period half-hourly values of Q_E and Q_E(EBOL) for the selected individual days June 27, July 6, July 18 and July 25 are presented. Data for July 17 was not plotted due to the limited amount of Q_E data available for that day.

The performance of the EBOL model as a predictor of Q_E is closely related to the performance of the Ohm's law approach for determining

Table 5.4. Comparison of half-hourly Q_E values measured using the BREB approach with Q_E values determined using the energy balance-Ohm's law model, Plateau Mountain, June 26 - July 26, 1985.

	Linear regression coefficients[1]					Measures of difference[2]			
	N[3]	r^2	Std. error W m^{-2}	a W m^{-2}	b	MBE W m^{-2}	RMSE W m^{-2}	Std. dev. of differences W m^{-2}	d
Q_E(EBOL)	804	0.505	51.2	65.2	0.752	45.9	71.5	54.8	0.761
Q_E(EBOL) Measured Q* and Q_G.	804	0.587	48.6	36.8	0.843	24.7	56.4	50.7	0.844
Q_E(EBOL) r_{am} substituted for r_a. No stability correction.	804	0.255	56.5	52.0	0.481	11.2	68.6	67.7	0.701

[1] The linear regression coefficents are based on the regression of the model predicted Q_E on the measured Q_E. a is the Y axis intercept, and b is the slope of the regression line. In all cases, t test scores indicated a greater than 99.9% probability that b ≠ 0.

[2] The measures of difference, as described by Fox (1981) and Willmot (1982), are based on the differences between the model predicted Q_E and the measured Q_E. MBE is the mean bias error, RMSE is the root mean square error and d is the index of agreement.

[3] N refers to the number of half-hour periods for which values were available.

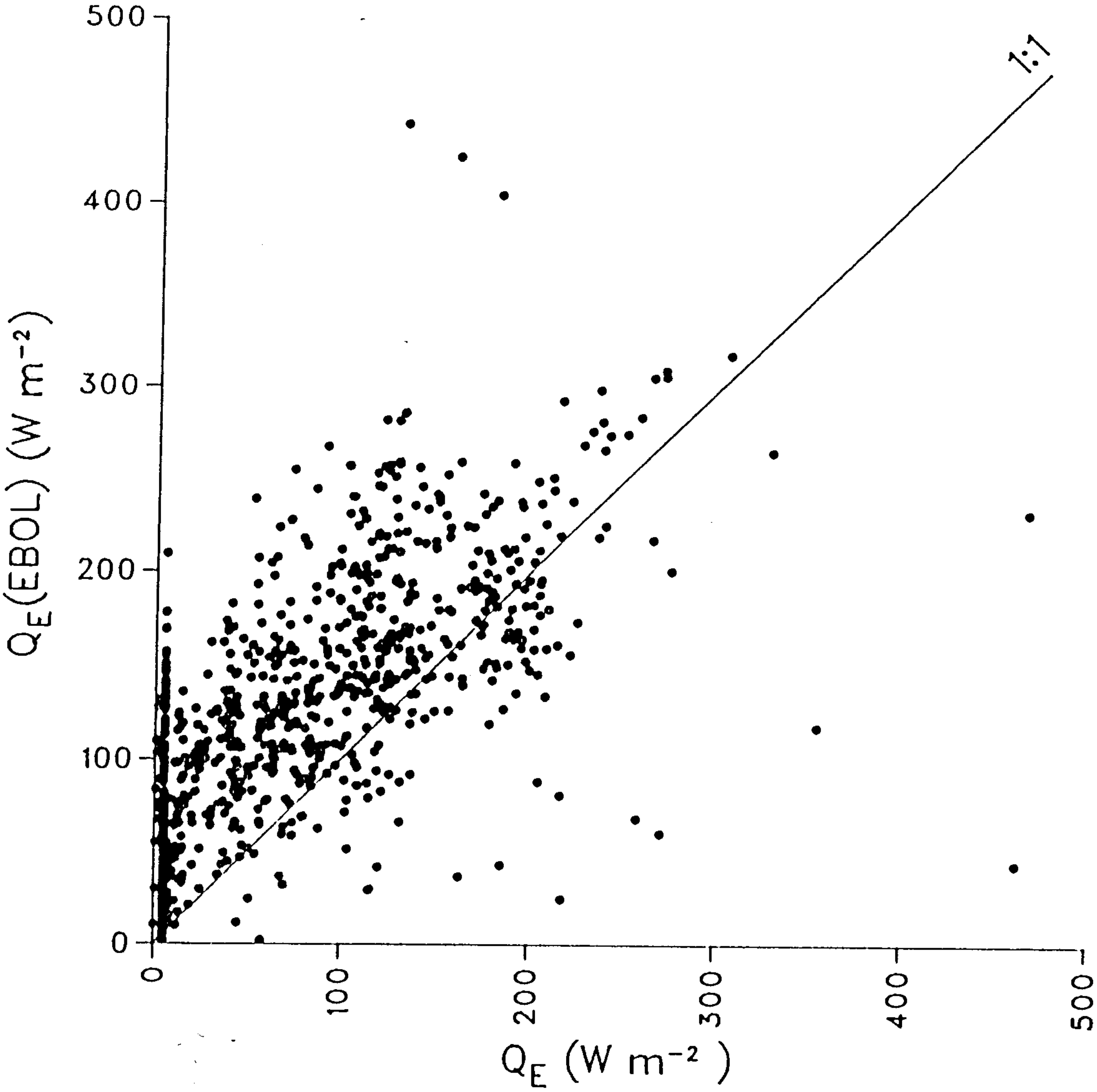

Figure 5.24. Comparison of half-hourly Q_E(EBOL) with Q_E measured using the BREB approach, June 26 - July 26, 1985, Plateau Mountain.

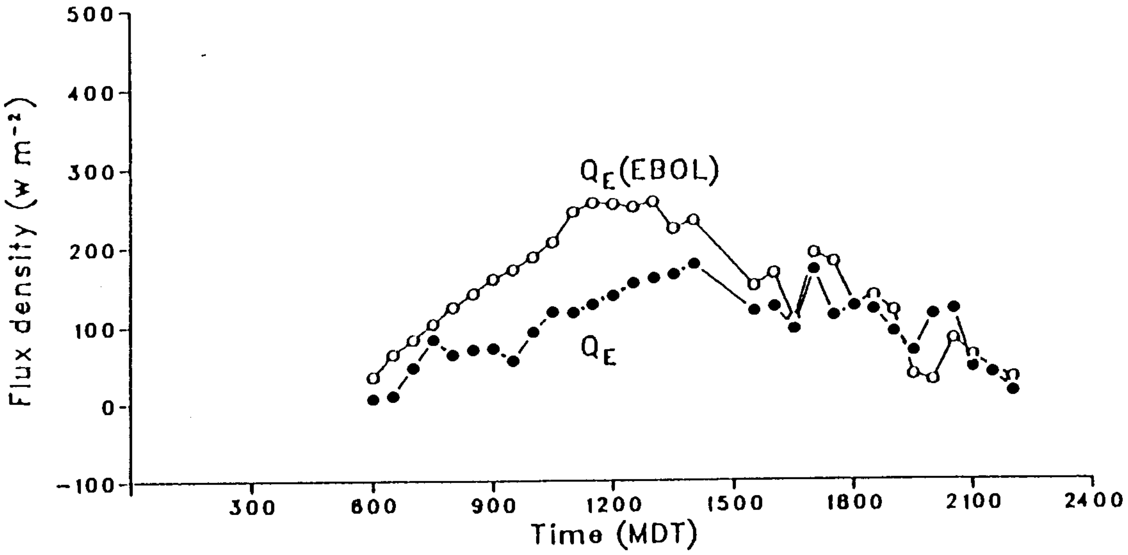

Figure 5.25. Half-hourly Q_E and Q_E(EBOL), June 27, 1985, Plateau Mountain.

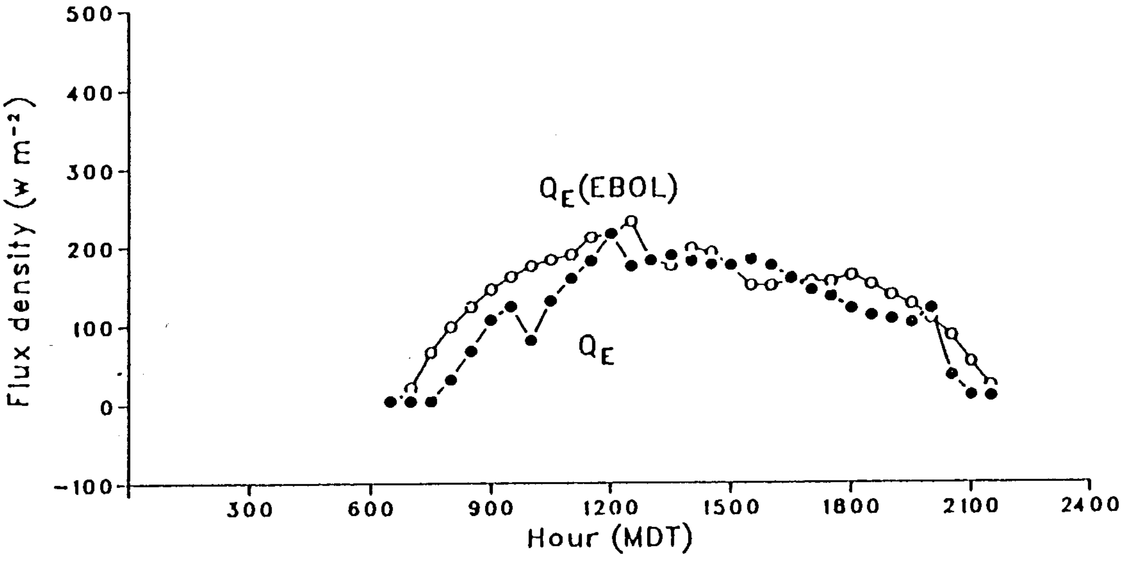

Figure 5.26. Half-hourly Q_E and Q_E(EBOL), July 26, 1985, Plateau Mountain.

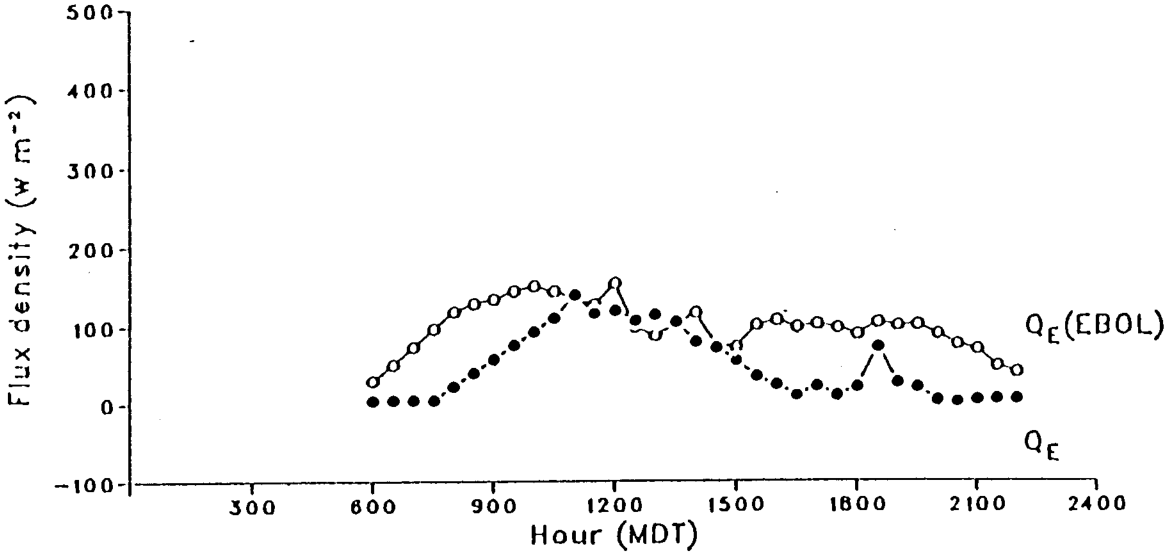

Figure 5.27. Half-hourly Q_E and Q_E(EBOL), July 6, 1985, Plateau Mountain.

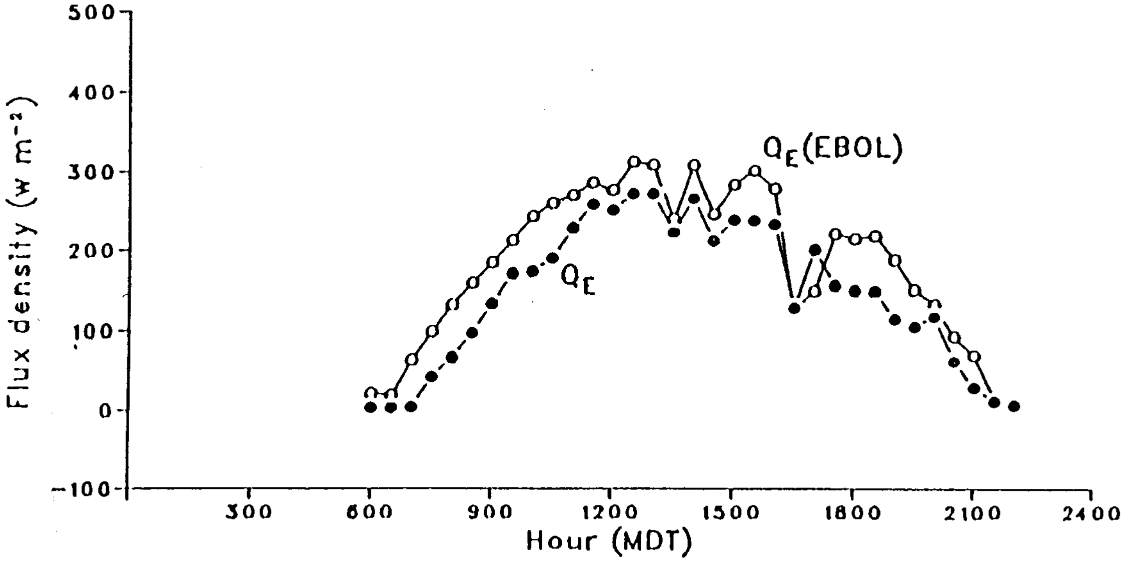

Figure 5.28. Half-hourly Q_E and Q_E(EBOL), July 18, 1985, Plateau Mountain.

Q_H. The MBE for the Q_E(EBOL) values that were determinued using the measured Q* and Q_G is the inverse of the MBE for Q_H(OL) presented in Table 5.3. As well, the RMSE and the standard deviation of the differences between the predicted and measured Q_E values are the same as those for the predicted and measured Q_H values. The generally smaller magnitude of the Q_E values means that these differences translate to a larger relative error, and the index of agreement for Q_E and Q_E(EBOL), determined with measured Q* and Q_G, is smaller than that for Q_H and Q_H(OL).

Incorporating Q(model) into the approach has the effect of increasing the RMSE by approximately 15.1 W m^{-2}, and lowering the index of agreement from 0.844 to 0.761. The empirical estimate of (Q* - Q_G) accentuates the tendency of Q_E(EBOL) to exceed Q_E, increasing the MBE by approximately 20 W m^{-2}.

The overall performance of the EBOL model as a means of estimating Q_E deteriorates further when a non-stability corrected r_{am} value is substituted for r_a. The RMSE approaches ±70 W m^{-2} and the index of agreement falls to 0.701.

Given the probable error associated with the half-hourly measurements of Q_E (errors associated with the Q_E measurements are discussed in Appendix 2) the performance of the EBOL model is considered to be good. If analysis is restricted to the 553 cases for which Q_E exceeded 25 W m^{-2} the average relative error of the model, using the measured Q* and Q_G, is 49.3% (std. dev. 55.3%). Using the empirically estimated (Q* - Q_G) the average relative error increases to ±73.2% (std. dev. 77.4%). If analysis is restricted to the 470 cases where Q_E exceeded 50 W m^{-2} the respective mean relative errors decrease to ±38.2% and ±54.2%. In both cases, using either the measured values or the empirical estimates, the relative error is considerably larger if Q_E values of less than 25 W m^{-2} are considered. However, the relative error in the BREB measured Q_E also becomes very large when Q_E is less than 25 W m^{-2}.

Figures 5.25 - 5.28 show that the EBOL model generally does a good job of tracking half-hourly Q_E. Particularly satisfying is the close agreement of the Q_E(EBOL) and Q_E during periods of fluctuating Q^* values. This is seen in the late afternoon of June 27, and during the middle part of the day on July 18.

The model's performance appears to be better when the surface is wet or moderately wet. On the dry-surface day, July 6, the model overestimates half-hourly Q_E throughout the day. On the wet-surface day, July 18, agreement between the predicted and observed Q_E values is particularly good. The most probable cause of the differences is the residual nature of the model. This means that when the surface is dry and Q_H is large, small errors in estimating Q_H and Q_G will result in large relative errors in the modelled Q_E. However, the apparent improvement in performance of the model may also reflect the better performance of the BREB approach when surface conditions are moist.

5.4.4 Equilibrium Based Modelling of Daylight Period Latent Heat Flux Densities

As discussed in Section 2.8.2, the success of an equilibrium based modelling approach for estimating daily or daylight Q_E will primarily depend on the successful estimation of α. In situations where α can be shown to be constant, or accurately predictable from commonly measured parameters, an equilibrium based model will be applicable.

The α values presented in Appendix 4 and summarized in Table 5.2 were calculated by dividing the BREB determined daylight period Q_E values by the Q_{eq} values determined from equation 2.46. The daylight period means of Q^*, Q_G and S were used as the input for equation 2.46. The calculated Q_{eq} values ranged from 3.1 to 10.5 MJ m^{-2}, with an average value of 7.9 MJ m^{-2}

(std. dev. 2.1 MJ m^{-2}).

The average daylight period α value for the 22 days that Q_E values were available was 0.581 (std. dev. 0.258). The largest daylight period α value (1.093) was measured on July 23, the lowest value (0.145) was measured on July 5.

The failure of α to approach 1.26 during the experiment suggests that actual evaporation never equalled potential evaporation, as defined by the Priestley Taylor expression (equation 2.47), for a full daylight period. Half-hourly α values approaching 1.26 did occur for brief periods, on the afternoon of July 17, the morning of July 18, July 23, and the morning of July 24. Half-hourly values in excess of 1.26 were rarely observed.

The behavior of α at this site matches that noted by Wilson and Rouse (1972) and Bailey (1983) for other sites with extensive bare soil surfaces. When the daylight period includes a period where the surface is wet, water can be readily evaporated and α approaches 1.26. However the surface quickly dries, retarding the efflux of water, and α decreases. The result is an α value approaching unity for the daylight period, as seen by the average α value of 0.85 on the high Q^* and low β days. For daylight periods which did not include the wet surface regime, soil moisture limitations and surface control restrict the movement of water to the surface throughout the daylight period. This results in α being considerably less then unity, as seen by the average value of 0.45 for the high Q^* and high β days.

The variable nature of α during the experiment suggests that there is little physical basis for a daily evaporation model based on the assumption of a constant α at this alpine tundra site. Models of this type have been proposed for arctic tundra sites (Rouse and Stewart 1972;Stewart and Rouse 1976). However, it may be possible that other exposed alpine tundra surfaces will consistently behave in a fashion similar to that observed at Plateau Mountain. If the regime of alpine tundra surfaces quickly becoming resistant to the movement of water after precipitation events, and daily summer α trending towards a mean value of 0.6 - 0.8 is characteristic of such sites, then an equilibrium based model, which assumed a fixed α value, would perform well at predicting seasonal Q_E. Such a model would overestimate Q_E on dry surface days and underestimate it on wet surface days, but provide good seasonal estimates. Further research for several seasons, at a range of sites, would be necessary to confirm the seasonal behavior of α at alpine tundra sites.

For several agricultural and some arctic tundra sites, empirical relationships between soil moisture measurements or other indices of soil wetness and α have been proposed. These relationships are proposed as a means of dealing with the problem of equilibrium based modelling of Q_E, when α is variable. Although soil moisture measurements are not commonly available for alpine tundra surfaces, it was felt that if such a relationship could be shown for Plateau Mountain site it would indicate a direction for future research. A strong relationship between α and soil moisture would indicate that equilibrium based models, using a variable α, might have a potential as a means of estimating daily or longer term Q_E in alpine tundra environments.

In Figure 5.29 the 22 daylight period α values are plotted against the volumetric soil moisture measurements from the 0-50 mm layer. The obvious outlier in the upper left corner of Figure 5.29 is the data from July 23. On this day soil moisture measurements were made in the morning, prior to the rain that occurred during the daylight period. This data was not used in the development of the best-fit curve. The best-fit curve, determined by linear regression, is shown in Figure 5.29. This equation for the best-fit curve has the form

$$\alpha = 0.346 \; X_W \tag{5.3}$$

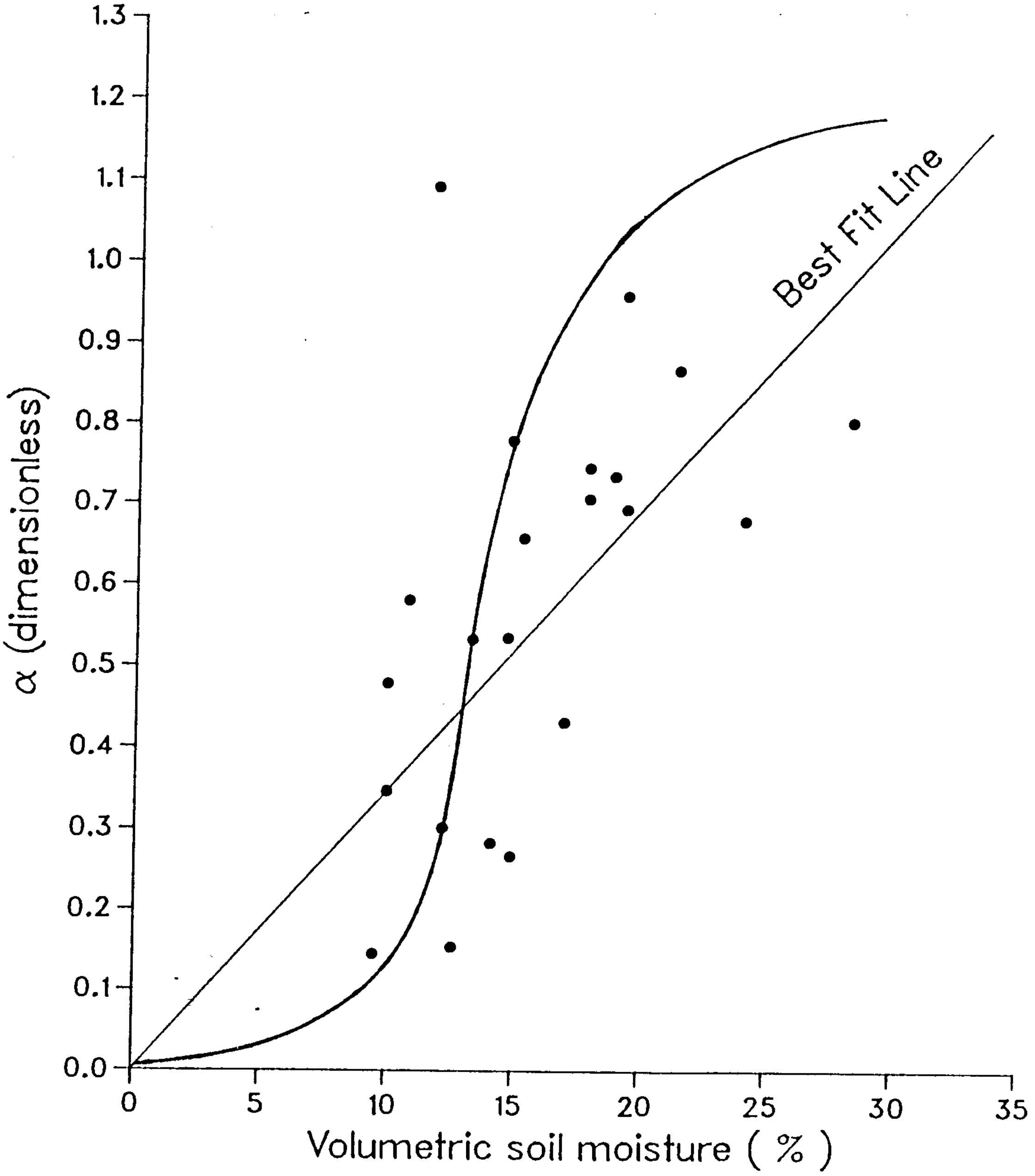

Figure 5.29. Daylight period α vs. volumetric soil moisture (0-50 mm), June 26 - July 26, 1985, Plateau Mountain

with $r^2 = 0.471$ and a standard error of 0.173. The t-test score for the slope coefficient was 15.36, indicating that there is more than a 99.9% probability that the relationship is significant. Attempts to improve upon this relationship by including a Y axis intercept, or using a polynomial to fit a non-linear curve to the data did not prove to be statistically significant. These results indicate that there is clearly a strong relationship between the α values and the volumetric soil moisture measurements from the 0-50 mm layer. However, the low r^2 value for equation 5.3 indicates that as a means of describing the relationship between α and soil moisture, it would have limited predictive or explanatory value.

Previous researchers (Davies and Allen 1973; Rouse et. al. 1977; Marsh et. al. 1981; Mawdsley and Ali 1985) have found that the relationship between α and soil moisture was best described by a non-linear expression. In particular, curves bases on logistical functions have commonly been used. In Figure 5.29 a non-linear curve, with the shape of a logistical function, has been hand fitted to the data.

The data appears to agree well with the middle segment of the curve. The agreement between the data and the lower and upper portions of the curve is less apparent. The difficulty in describing the upper segement of the curve may be due to the limited nature of the Plateau Mountain data set. The dry surface conditons meant that soil moisture was generally a limiting factor on evaporation. To determine a logistical function describing the relationship between α and soil moisture it would be necessary to collect data when soil moisture was not a limiting factor. It would be desirable for future investigations into equilibrium based modelling of evaporation in alpine tundra environments to consider a wide range of surface conditions.

Furthermore, it is worth recalling the errors associated with the volumetric soil moisture measurements when considering Figure 5.29. High quality surface moisture parameterization would be another important component of future investigations into the potential of equilibrium based evaporation models for alpine tundra environments.

CHAPTER 6

CONCLUSIONS

6.1 Introduction

In this chapter, the general conclusions regarding the radiation and energy balance measurements, and the evaporation modelling are summarized. Some suggestions regarding future work are also presented.

6.2 Radiation Balance Measurements

Radiatively, the snowfree alpine tundra surface at Plateau Mountain behaved in a similar fashion to lower elevation tundra surfaces. The surface reflectivity characteristics, on both a daily and half-hourly basis, at Plateau Mountain were quite similar to those that have been reported for lower elevation agricultural and tundra sites. The nearly constant mean daily *a* of 0.17 at Plateau Mountain was similar to that observed for snowfree arctic and sub-arctic tundra sites. The diurnal trend of half-hourly *a* also matches that observed at arctic tundra sites. Although there is a limited amount of comparable data, the range of daily L↑ values measured at Plateau Mountain (26 - 32 MJ m^{-2}) was also comparable to daily summer values for lower elevation arctic tundra sites. This suggests that both the emissivity and surface temperature regimes of arctic and alpine tundra sites are similar in the summer.

An important attribute of an alpine tundra is that the surface may be snow covered on any given day of the year. The effects of a summer snowstorm, large increases in *a*, and large decreases in L↑, are well demonstrated in the July 17, 1985 data from Plateau Mountain. To accurately describe the surface radiative characteristics of an alpine tundra surface in the summer the possibility of snowcover during portions of the summer must be acknowledged.

The largest difference between the radiation balance of the Plateau Mountain site, and that of lower elevation tundra sites, resulted from the greater atmospheric transmissivity at Plateau Mountain. Maximum half-hourly transmissivities approaching 0.85, and daily transmissivities in excess of 0.70, were common. For cloudless days, atmospheric transmissivity at Plateau Mountain, both half-hourly and daily, was well represented by Lowry's (1980) empirical expression.

The high atmospheric transmissivity resulted in predictably large daily $K\downarrow$ values at Plateau Mountain on both cloudless and partly cloudy days. Average daily $K\downarrow$ values were generally greater than 25 MJ m^{-2}. Variations in atmospheric transmissivity on partly cloudy days resulted in large fluctuations in the half-hourly $K\downarrow$ values, but daily values remained high for those days. Only when the sky was completely obscured by heavy low level cloud did daily $K\downarrow$ values become low.

Elevation effects on $L\downarrow$ were less obvious. Qualitatively, the theoretical decrease in cloudless sky $L\downarrow$ associated with increases in elevation appeared to be largely overshadowed by the effects of cloud cover on $L\downarrow$. There does not appear to be a large difference between the $L\downarrow$ values observed at Plateau Mountain, and those of lower elevation sites. Unfortunately, due to instrumentation difficulties, the quality of the $L\downarrow$ data collected at Plateau Mountain was less than what was desired. Future work in this area, particularly better quality $L\downarrow$ measurements and the development of models for estimating $L\downarrow$ in alpine environments, which account for both cloud and elevation effects, would be of value.

Although direct intercomparisons are difficult, daily Q^* values at Plateau Mountain appeared to be only slightly higher than those recorded on fine days at lower elevation sites. Daily Q^* values ranged from 8.2 MJ m^{-2} to 15.8 MJ m^{-2}. The high daily $K\downarrow$ values, as compared to lower elevation sites, were not matched by comparably high Q^* values. This suggests that at Plateau Mountain, during the period of this experiment, the increase in K^* with elevation was compensated for by a more negative L^*.

The relationship between $K\downarrow$ and Q^* at Plateau Mountain was found to be quite comparable to that found by Davies (1967) for 14 lower elevation sites with similar albedos. At this 2475 m asl site, the shift in the relative magnitudes of $K\downarrow$ and $L\downarrow$ did not appear to result in a significantly different relationship between $K\downarrow$ and Q^*, as compared to relationships that have been observed at lower elevation sites. An interesting question for future work would be a comparative examination of relationships between $K\downarrow$ and Q^* at increasing elevations. Given the level of accuracy in the measurement of Q^*, it was concluded that the Davies (1967) relationship could be used to predict Q^* at Plateau Mountain with a reasonable degree of confidence, when half-hourly or daily $K\downarrow$ data was available.

6.3 Energy Balance Measurements

From the energy balance measurements at Plateau Mountain, it was concluded that the chief factors determining the nature of the energy balance regime at the site over the course of the experiment were radiative energy and surface moisture availability. The amount of radiative energy at the surface was largely determined by atmospheric transmissivity. The availability of surface moisture determined the nature of the partitioning of the available energy at the surface into Q_H and Q_E. Daily and half-hourly Q_G values were found to be an essentially constant proportion of Q^*, approximately 10-15% . An interesting subject for future investigation would be the areal variation of Q_G in the alpine tundra environment.

The limiting influence of surface moisture availability on the energy balance is evidenced by the general failure of daily Q_E to equal Q_{pe} during the experiment. The lack of available surface moisture meant that evaporation rates were low (1 - 4 mm per day), and the surface energy balance regime was dominated by Q_H at this site.

Previous summer energy balance studies in alpine environments have suggested environments with considerably wetter surfaces, and greater evaporation rates. The energy balance regime at Plateau Mountain, during the experiment, was quite similar to that postulated by Lewis and Callaghan (1976) for an arctic fellfield in the late summer.

Qualitative observations indicated that the sub-surface at Plateau Mountain (depths greater than 0.20 m) remained very moist throughout the experiment. There was very strong evidence, on both a daily and half-hourly basis, of a dynamic and active surface control over the movement of sub-surface moisture to the atmosphere. The combination model, although theoretically not suitable for modelling evaporation from a partially vegetated tundra surface, proved to be useful as a means of quantitatively describing this surface resistance. It is hypothesized that this surface control represents the net effect of both physical and physiological control by the tundra vegetation, and the drying of the top layers of the bare soil surface. A better parameterization of the soil and surface moisture regime of the alpine tundra would be necessary to address this question. An investigation into the spatial and temporal distribution of soil moisture in the alpine tundra environment would be a worthwhile, interesting and challenging study. Energy balance studies, coordinated with investigations into the physiological response of alpine plants to drying conditions would also be of considerable merit.

Determinations of half-hourly Q_H made using both the eddy correlation, and Ohm's law approaches, agreed very well with the Q_H measurements made using the BREB approach. The differences between the Q_H values determined by the approaches generally being not much larger than the error associated with the BREB measurement of Q_H. The good agreement between these three independent approaches suggests that a high degree of confidence can be expressed with regard to the energy balance measurements made at Plateau Mountain.

It is noteworthy that the eddy correlation instrumentation used in this experiment proved surprisingly robust. The instrumentation was operated when windspeeds were in excess of 10 m s^{-1} with no damage to the thermocouple.

The characteristics of the Plateau Mountain site, high windspeeds, an aerodynamically smooth surface lacking large roughness elements and generally neutral or unstable conditions, made it well suited to the application of the Ohm's law approach. The approach was relatively insensitive to errors in determining the surface roughness, the effects of bluff bodies and the effect of atmospheric stability on the turbulent transfer process.

The Ohm's law approach may be better suited for the determination of Q_H in alpine tundra environments than the BREB approach. As the BREB approach requires measurements of the vertical gradients of vapour pressure, its application in cold, dry, alpine environments can be problematic. As noted in Appendix 2, vapour pressure measurement can become a large source of error with the BREB approach. The success with which the BREB technique was used in this experiment can be partially attributed to the fine weather experienced during the experiment. The major measurement problem associated with the Ohm's law approach for determining Q_H is the measurement of T_0. This source of error only becomes significant when r_a is very small (less than 10 s m^{-1}), or the error in T_0 is large (greater than ±5° C). Measurement of T_0 to within ±5° C is not unrealistic, particularly with the increasing availability of infrared thermometers. For future investigations into the surface energy balance regimes of alpine sites, one approach might be to use an Ohm's law approach as a means to continuously determine Q_H, with the eddy correlation or the BREB approach being used coincidentally during periods of fine weather to confirm the results. Such an approach would have considerably simpler logistics than the Plateau Mountain experiment approach, where the BREB technique was used continuously. The data from the Plateau Mountain experiment suggests that such an approach would provide data of equivalent quality.

6.4 Evaporation Modelling

The proposed energy balance - Ohm's law model for half-hourly Q_E, which requires measurements of K↓, T_0, T_z, u_z and knowledge of z_0, was a reasonably good predictor of half-hourly Q_E at Plateau Mountain. For the 804 half-hour daylight cases considered, the model had a probable error of ±71.5 W m^{-2}. The generally low Q_E values measured during the experiment meant that a probable error of ±71.5 W m^{-2} represented a large relative error, greater than 100%. However, if analysis was restricted to the cases where Q_E values exceeded 50 W m^{-2}, then the relative error of the model was only ±54.2%. Some of this error arises from the use of the empirical expression to predict $(Q^* - Q_G)$ from K↓. When the measured Q^* and Q_G values were used in the model the probable error decreased to ±56.4 W m^{-2}. This would translate to a relative error of ±38.2% for the cases where Q_E exceeded 50 W m^{-2} A relative error of this magnitude is comparable to the measurement error associated with the BREB approach. It is concluded that this model would provide reasonable estimates of half-hourly Q_E at suitable alpine tundra sites, where the necessary data was available.

The site limitations of the model, extensive areas of flat and homogeneous surface are required, restrict the model's general applicability. The model, as presented, could not be used to estimate evaporation from extensive areas of non-homogeneous alpine tundra. The perceived chief use of this model would be as an alternative to the direct measurement of half-hourly or hourly Q_E. Such an application might be the estimation of evaporation in a portion of a well instrumented research watershed, or as a means of providing point data to help verify the estimates of areal evaporation from a more empirical model.

Future areas for investigation, with regard to the EBOL model, would include consideration of it's applicability at other alpine tundra locations. Particularily interesting would be the performance of the model at sites with wetter surfaces. Another area for investigation would be the possibility of including a surface temperature estimating component to the model. At present the most restrictive data requirement of the model are the surface temperature measurements. The model's general applicability would be extended if a means of estimating surface temperature from single level data could be successfully added to the model.

The observed dynamic nature of the alpine tundra surface at Plateau Mountain indicated that there may be difficulties in the development of an equilibrium based model for estimating daily evaporation at alpine tundra sites. As there was not a constant relationship between actual and equilibrium evaporation, an equilibrium based model which assumed a constant α value could not be used to predict daily evaporation at this site. Such a model may have potential as a predictor of seasonal evaporation at such sites.

An equilbrium based daily evaporation model, in which α is determined as a function of soil moisture appears to hold some promise. The Plateau Mountain data indicated that there was a relationship between soil moisture and α at this site, but the derived relationship had limited predictive value. More daily evaporation data from alpine tundra sites, for a variety of surface conditions, will be necessary to determine how consistent such relationships might be. As the measurement of soil moisture is likely to remain problematic in alpine tundra environments, future investigations might also consider the possibility of relating α to some other index of surface wetness, as was done for agricultural environments by Mawdsley and Ali (1985).

6.5 Summary

This application of microclimatological experimental method to an investigation of the surface radiation and energy regimes at the surface of an alpine tundra confirmed existing knowledge about such environments, and suggested directions for future investigation.

Like other alpine sites, Plateau Mountain experiences high solar irradiances. Interestingly, the high solar irradiances do not appear to result in equivalently high Q^* values. As at other lower elevation sites, a simple empirical relationship between $K\downarrow$ and Q^* was found to be a good predictor of Q^* at this site.

The nature of the partitioning of the available radiative energy at the surface into Q_H and Q_E indicated a dynamic and active surface control over the movement of soil moisture to the atmosphere. Such control has not been reported by other investigators working in alpine tundra environments. This type of surface behaviour raises questions about the nature of alpine tundra surfaces, and poses problems for those interested in modelling short-term evaporation from such surfaces.

The results from the Plateau Mountain experiment would suggest that physically based models, such as the proposed EBOL model, will work well as a means of estimating short-term evaporation from alpine tundra surfaces, when the site and data requirements are met. The equilibrium based models also appear to have potential as a simple means of estimating daily, or longer term evaporation in alpine tundra environments.

APPENDIX 1 - SYMBOLS

Symbol	Quantity	Units
Roman capital letters		
C	volumetric heat capacity of soil	MJ m^{-3} K^{-1}
C_a	volumetric heat capacity of dry air	MJ m^{-3} K^{-1}
C_m	volumetric heat capacity of soil minerals	MJ m^{-3} K^{-1}
C_o	volumetric heat capacity of soil organics	MJ m^{-3} K^{-1}
C_w	volumetric heat capacity of water	MJ m^{-3} K^{-1}
D	wet bulb depression	°C, K
D_z	wet bulb depression at height z	°C, K
D_0	wet bulb depression at the surface	°C, K
I_0	solar constant	W m^{-2}
K_0	extraterrestrial radiation flux density	W m^{-2}, MJ m^{-2}
$K\downarrow$	global solar radiation flux density	W m^{-2}, MJ m^{-2}
$K\uparrow$	reflected solar radiation flux density	W m^{-2}, MJ m^{-2}
K^*	net solar radiation flux density	W m^{-2}, MJ m^{-2}
K_h	eddy diffusivity for sensible heat	m^2 s^{-1}
K_m	eddy diffusivity for momentum	m^2 s^{-1}
K_v	eddy diffusivity for vapour	m^2 s^{-1}
$L\downarrow$	incoming longwave radiation flux density	W m^{-2}, MJ m^{-2}
$L\uparrow$	outgoing longwave radiation flux density	W m^{-2}, MJ m^{-2}
L^*	net longwave radiation flux density	W m^{-2}, MJ m^{-2}
M	optical air mass	dimensionless
P	atmospheric pressure	kPa
P_0	atmospheric pressure at sea level	kPa
Q^*	net radiation flux density	W m^{-2}, MJ m^{-2}
$Q\downarrow$	net incoming solar and longwave radiation flux density	W m^{-2}, MJ m^{-2}
		W m^{-2}, MJ m^{-2}
Q_{div}	energy flux density resulting from the net horizontal movement of sensible and latent heat	W m^{-2}, MJ m^{-2}
Q_E	latent heat flux density	W m^{-2}, MJ m^{-2}

Q_{Ediv}	energy flux density resulting from the net horizontal movement of latent heat	W m^{-2}, MJ m^{-2}
Q_{Est}	energy flux density resulting from the net storage of latent heat in the atmosphere	W m^{-2}, MJ m^{-2}
Q_{eq}	latent heat flux density resulting from equilibrium evaporation	W m^{-2}, MJ m^{-2}
Q_G	soil heat flux density	W m^{-2}, MJ m^{-2}
Q_H	sensible heat flux density	W m^{-2}, MJ m^{-2}
Q_{Hdiv}	energy flux density resulting from the net horizontal movement of sensible heat	W m^{-2}, MJ m^{-2}
Q_{Hst}	flux of energy resulting from storage of sensible heat in the atmosphere per unit surface area	W m^{-2}, MJ m^{-2}
Q(model)	empirically estimated ($Q^* - Q_G$)	W m^{-2}, MJ m^{-2}
Q_P	energy flux density resulting from photosynthesis	W m^{-2}, MJ m^{-2}
Q_{pe}	latent heat flux density resulting from potential evaporation	W m^{-2}, MJ m^{-2}
Q_{stor}	energy flux density resulting from the net storage of sensible and latent heat in the atmosphere	W m^{-2}, MJ m^{-2}
Q_V	energy flux density resulting from the net storage of sensible heat in the phytomass	W m^{-2}, MJ m^{-2}
Ri	Richardson number	dimensionless
RV	radius vector	dimensionless
S	slope of the saturation vapour pressure curve at T	Pa K^{-1}
S_W	slope of the saturation vapour pressure curve at T_W	Pa K^{-1}
T	air temperature	°C, K
T_0	surface temperature	°C, K
T_s	soil temperature	°C, K
T_W	wet bulb temperature	°C, K
T_z	air temperature at height z	°C, K
X_W	volumetric soil water content	%
X_o	percentage of organics in soil by volume	%
X_a	percentage of air in soil by volume	%

X_m	percentage of minerals in soil by volume	%
Z	solar zenith angle	degrees

Roman small letters

a	surface albedo ($K\uparrow/K\downarrow$)	dimensionless
c_p	specific heat of air at a constant pressure	J kg^{-1} K^{-1}
d	zero plane displacement height	m, mm
e	vapour pressure	Pa
e_0	surface vapour pressure	Pa
e_z	vapour pressure at height z	Pa
$e_s(T_0)$	saturation vapour pressure at T_0	Pa
$e_s(T_W)$	saturation vapour pressure at T_W	Pa
$e_s(T_z)$	saturation vapour pressure at T_z	Pa
g	acceleration of gravity	m s^{-2}
k	von Karman's constant	dimensionless
r_a	aerodynamic resistance to sensible and latent heat transfer	s m^{-1}
r_{am}	aerodynamic resistance to momentum transfer	s m^{-1}
r_s	surface resistance	s m^{-1}
r_{st}	stomatal or canopy resistance	s m^{-1}
t	transmissivity ($K\downarrow/K_0$)	dimensionless
u	horizontal windspeed	m s^{-1}
u_z	windspeed at height z	m s^{-1}
u_0	windspeed at z_0	m s^{-1}
u_*	eddy or friction velocity	m s^{-1}
w	vertical windspeed	m s^{-1}
x	horizontal distance	m, mm
z	vertical distance	m, mm
z_0	surface roughness length	mm

z_r	reference height above the surface	m

Greek capital letters

Φ_M	integrated stability function	dimensionless
Λ	Beckey-Fairley location index	km

Greek small letters

α	equilibrium coefficient (Q_E/Q_{eq})	dimensionless
β	Bowen ratio (Q_H/Q_E)	dimensionless
ρ	density of dry air	kg m^{-3}
γ	psychrometric constant	Pa K^{-1}
λ	latent heat of vapourization	MJ kg^{-1}
ϕ_M	stability function	dimensionless
σ	Stefan-Boltzmann constant	W m^{-2} K^{-4}
τ	shearing stress	Pa
ξ	ratio of the molecular weight of water to the mean molecular weight of dry air	dimensionless

APPENDIX 2 - ERROR ANALYSIS

Any value Y can be expressed as a function of a set of measurements X_1, X_2, ... X_n which have associated with them errors δX_1, δX_2, ... δX_n, so that

$$Y = f(X_1 \pm \delta X_1,\ X_2 \pm \delta X_2,\ ....\ X_n \pm \delta X_n) \ . \qquad (A2.1)$$

The total error in Y, δY, is given by

$$\delta Y = \frac{\partial Y}{\partial X_1}\ \delta X_1 + \frac{\partial Y}{\partial X_2}\ \delta X_2 + ...\ \frac{\partial Y}{\partial X_n}\ \delta X_n \ . \qquad (A2.2)$$

The probable absolute error in Y, δY_{rms}, will be less than the total error and is found by taking the root-mean-square of equation A2.1, so that

$$\delta Y_{rms} = [\ (\frac{\partial Y}{\partial X_1}\ \delta X_1)^2 + (\frac{\partial Y}{\partial X_2}\ \delta X_2)^2 + \ .....\ + (\frac{\partial Y}{\partial X_n}\ \delta X_n)^2\ ]^{0.5} \ . \qquad (A2.3)$$

The relative error is defined by $\delta Y_{rms}/\ Y$ and is expressed as a percentage.

Errors in Radiation Flux Density Measurements

Error Analysis for K↓, K↑ *and* Q*

The directly measured radiation flux densities, K↓, K↑ and Q*, are determined using the following expression

$$F = c\ m \qquad (A2.4)$$

where F is the flux density, c is the sensor calibration constant and m is the measured electrical signal from the sensor. The probable absolute error in the measured radiative flux density is thus given by

$$\delta F_{rms} = [(c \ \delta m)^2 + (m \ \delta c)^2]^{0.5} . \qquad (A2.5)$$

For the following analysis, Campbell Scientific's specification for the CR21 data system of $\delta m = \pm 5 \ \mu V$ was assumed.

Errors in radiation sensor calibration arise as a result of deviations from the theoretical linear response of the sensor to changes in radiative flux densities. An error free sensor will have a perfectly linear response to increases or decreases in radiative flux density. The calibration error associated with a particular radiation sensor is usually expressed as a percentage of the radiative flux density being measured. For the Middleton CN-1 pyrradiometer the calibration error was assumed to be ±7%, and for the Middleton CN7 Solarimeter the calibration error was assumed to be ±5% . For the Eppley PSP pyranometer the manufacturer's specification of ±0.5% was assumed. These are considered liberal estimates, and are similar to those assumed in other error analyses for comparable sensors.

The calculated probable absolute errors and relative errors for a range of radiation flux density values are presented in Table A2.1 . The tabulated results show that the error introduced by voltage measurement is only significant at low flux density magnitudes. When the directly measured flux densities are in excess of 100 W m^{-2}, the measurement error is primarily attributable to the sensor calibration.

Error Analysis for L↑

Differentiation of the Stefan-Boltzmann expression, equation 2.5, yields the following expression for the probable absolute error in L↑,

$$\delta L\uparrow_{rms} = [\ (\sigma T_0^4\ \delta\epsilon)^2 + (4\epsilon\sigma T_0^3\ \delta T_0)^2 + (\epsilon T_0^4\ \delta\sigma)^2\ ]^{0.5}\ . \qquad (A2.6)$$

For the purpose of this analysis, errors arising from uncertainty regarding the Stefan–Boltzmann constant can be ignored. The chief sources of error can be regarded as uncertainty in the estimate of surface emissivity, and the measurement of T_0. For this analysis the relative error in the estimated surface emissivity was assumed to be ±10% . This is considered a liberal estimate as it suggests that actual surface emissivity fell in the wide range of 0.81 - 0.99. Assessment of the error in the T_0 measurement is difficult. Errors not only arise from the temperature sensor calibration and the measurement of the sensor output, but are also related to the problem of determining representative areal surface temperatures from individual sensors placed on the surface. For this analysis, error analysis was done assuming a range of possible errors in T_0, ±1°C, ±5°C and ±10°C.

The results of the error analysis for L↑ over a range of surface temperaures are presented in Table A2.2.

Error Analysis for L↓

The residual approach used to determine L↓ accumulates the errors from the other measured radiation balance components in the calculated L↓ value. The probable error in the L↓ value is thus given by

$$\delta L\downarrow_{rms} = [(\delta Q^*_{rms})^2 + (\delta K\downarrow_{rms})^2 + (\delta K\uparrow_{rms})^2 + (\delta L\uparrow_{rms})^2\ ]^{0.5}\ . \quad (A2.7)$$

As the calculated L↓ value will not be associated with a unique set of values for the measured radiation flux densities, it is not possible to assign a specific error to a specific L↓ value. In Table A2.3 the probable absolute and relative errors for L↓, assuming, the mean daily, daylight and night values for the other radiation balance terms, are presented. The effect of a range of errors in the measurement of T_0 on $\delta L\downarrow$ is also shown in Table A2.3.

Table A2.1. Error analysis results for Q^*, $K\downarrow$ and $K\uparrow$ measurements.

Flux Density (W m^{-2})	δQ^*_{rms} (W m^{-2})	$\frac{\delta Q^*_{rms}}{Q^*}$ (%)	$\delta K\downarrow_{rms}$ (W m^{-2})	$\frac{\delta K\downarrow_{rms}}{K\downarrow}$ (%)	$\delta K\uparrow_{rms}$ (W m^{-2})	$\frac{\delta K\uparrow_{rms}}{K\uparrow}$ (%)
0	0.27	----	0.53	----	0.21	---
50	3.51	7.02	0.59	1.18	2.51	5.02
100	7.01	7.01	0.74	0.74	5.01	5.01
250	17.5	7.00	1.36	0.54	12.5	5.00
500	35.0	7.00	2.56	0.51	25.0	5.00
750	52.5	7.00	3.83	0.51	37.5	5.00
1000	70.0	7.00	5.03	0.50	50.0	5.00

Table A2.2. Error analysis results for $L\uparrow$.

T_o		$L\uparrow$	$\delta T_o = \pm 1^\circ C$		$\delta T_o = \pm 5^\circ C$		$\delta T_o = \pm 10^\circ C$	
			$\delta L\uparrow_{rms}$	$\delta L\uparrow_{rms} / L\uparrow$	$\delta L\uparrow_{rms}$	$\delta L\uparrow_{rms} / L\uparrow$	$\delta L\uparrow_{rms}$	$\delta L\uparrow_{rms} / L\uparrow$
(°C)	(K)	$(W\ m^{-2})$	$(W\ m^{-2})$	(%)	$(W\ m^{-2})$	(%)	$(W\ m^{-2})$	(%)
-5	268.2	264.0	29.6	11.2	35.3	13.4	49.1	18.6
0	273.2	284.3	31.9	11.2	37.8	13.3	52.3	18.4
10	283.2	328.2	36.8	11.2	43.2	13.2	59.0	18.0
20	293.2	377.1	42.2	11.2	49.2	13.0	66.4	17.6
30	303.2	431.3	48.3	11.2	55.7	12.9	74.4	17.3
40	313.2	491.0	54.9	11.2	62.9	12.8	83.1	16.9

Table A2.3. Error analysis results for $L\downarrow$.

	$K\downarrow$ (W m^{-2})	$\delta K\downarrow_{rms}$ (W m^{-2})	$K\uparrow$ (W m^{-2})	$\delta K\uparrow_{rms}$ (W m^{-2})	Q^* (W m^{-2})	δQ^*_{rms} (W m^{-2})	$L\uparrow$ (W m^{-2})	δT_o (°C)	$\delta L\uparrow_{rms}$ (W m^{-2})	$L\downarrow$ (W m^{-2})	$\delta L\downarrow_{rms}$ (W m^{-2})	$\delta L\downarrow_{rms} / L\downarrow$ (%)
daily mean	298.6	1.49	50.9	2.5	141.2	9.9	348.3	±1	39.0	242.9	40.3	16.6
								±5	45.3		46.5	19.1
								±10	62.0		62.9	25.9
daylight mean	434.3	2.17	74.1	3.71	237.4	16.6	365.3	±1	40.2	242.4	43.7	18.0
								±5	47.5		50.5	20.8
								±10	65.8		68.0	28.1
night mean	--	---	---	---	-70.4	4.9	311.1	±1	34.2	240.7	34.5	14.3
								±5	40.4		40.7	16.9
								±10	56.0		56.2	23.3

Errors in BREB Determination of Q_H and Q_E

For this analysis, the absolute and relative errors in temperature measurement were assessed. These were used to determine the errors in the calculated Bowen ratio. In turn, these errors were combined with the probable errors in the measurement of Q^* and Q_G to determine the errors associated with Q_H and Q_E, as measured using the BREB approach. This method of assessing errors is similar to that used by Fuchs and Tanner (1970).

Only quantifiable and objective sources of error are considered in this analysis. More subjective sources of error, such as improperly adjusted water feeds for the T_W sensors and radiative heating of the temperature sensors are not considered. Furthermore, the error analysis does not consider the error introduced by the horizontal divergence of sensible and latent heat.

Error Analysis for Temperature Measurement

Temperatures at each level, both wet and dry bulb, were determined by adding the measured differences between levels to the measured absolute temperatures at level 1. For example the dry bulb temperature at level 2, T_{z_2}, was determined from

$$T_{z_2} = T_{z_1} + \Delta T_{1\text{-}2} \tag{A2.8}$$

where $\Delta T_{1\text{-}2}$ is the difference in temperature between levels 1 and 2. Hence, the probable absolute error in T_{z_2} is given by

$$\delta T_{z_2,rms} = [(T_{z_1}\ \delta\Delta T_{1\text{-}2})^2 + (\Delta T_{1\text{-}2}\ \delta T_{z_1})^2\ ]^{0.5}. \tag{A2.9}$$

For a detailed analysis of the error associated with absolute temperature measurements using thermocouples and this data system, the reader is referred to the manual for the Campbell Scientific CR21X data system. For this analysis the following assumptions were made; (1) reference junction temperatures were measured to within ±0.3°C, (2) thermocouple generated voltages were measured to within $\pm 2.5 \mu V$, and (3) there was a 1% slope error in the thermocouple calibration. For temperature differences between the reference junction (data system) and the thermocouple junction (wet or dry bulb temperature) of 0 - 15 °C the probable error in absolute temperaure measurement ranges from ± 0.307 - 0.341 °C. The mean of these values, ±0.32 °C was assumed as the error associated with the absolute temperature measurements at level 1 of the differential psychrometer system.

Temperature differences between thermocouple junctions, ΔT, were determined from

$$\Delta T = c \ m \tag{A2.10}$$

where c is the calibration constant for the thermocouples, and m is the measured voltage generated by the difference in temperatures between the thermocouple junctions. The probable error in ΔT will thus be given by

$$\delta \Delta T_{rms} = [(c \ \delta m)^2 + (m \ \delta c)^2]^{0.5} \tag{A2.11}$$

Three junction copper-constantan thermocouples were used in the differential psychrometer system to measure temperature differences between levels. For these sensors $c = 8.503$ °C mV^{-1} and, assuming a 1% slope error in the thermocouple calibration, $\delta c = \pm 0.4418$ °C mV^{-1}. For the CR21X, over the range of voltage measurement used, $\delta m = \pm 2.5 \ \mu V$.

In Table A2.4 the probable absolute and relative errors for a range of ΔT values are presented. The tabulated data shows that small temperature differences between thermocouple junctions, ≤0.75 °C, can be measured to within ± 0.05 °C. This theoretical result was supported by the observed performance of the differential psychrometer system in the laboratory.

Errors associated with the absolute temperature measurements at levels 2, 3 and 4, assuming a range of ΔT values between the levels, are presented in Table A2.5. The tabulated results show that when temperature differences between levels were small, the error associated with their measurement introduced relatively small errors in the measurement of absolute temperatures. The largest contributer to the error in the measurement of absolute temperatures is the error associated with the measurement of the reference junction temperature.

On the basis of this analysis, a probable error of ±0.32 °C for absolute temperature measurements at all levels for both wet and dry bulb sensors was assumed.

Table A2.4. Error analysis results for ΔT measurements.

ΔT (°C)	m (mv)	$\delta\Delta T_{rms}$ (°C)	$\frac{\delta\Delta T_{rms}}{\Delta T}$ (%)
0	0	0.0213	----
0.010	0.0012	0.0213	213.0
0.050	0.0059	0.0214	42.8
0.100	0.0118	0.0219	21.9
0.250	0.0294	0.0249	9.96
0.500	0.0588	0.0336	6.72
0.750	0.0882	0.0444	5.92
1.000	0.1176	0.0561	5.61
2.000	0.2352	0.1060	5.30
5.000	0.5880	0.2606	5.21

Table A2.5. Error analysis results for absolute temperature measurements at levels 2, 3 and 4.

ΔT (°C)	$\delta T_{z_2 rms}$ (°C)	$\delta T_{z_3 rms}$ (°C)	$\delta T_{z_4 rms}$ (°C)
0	0.321	0.322	0.323
0.10	0.322	0.323	0.323
0.25	0.322	0.323	0.324
0.50	0.323	0.324	0.326
0.75	0.324	0.327	0.330
1.00	0.326	0.331	0.335

For this analysis ΔT was assumed to be same between levels, so $T_{z_2} = T_{z_1} + \Delta T$, $T_{z_3} = T_{z_1} + 2\Delta T$, and $T_{z_4} = T_{z_1} + 3\Delta T$.

Error Analysis for β

Combining equation 2.19 and equation 3.2, and assuming that ΔT_W is relatively small, the Bowen ratio, β, can be determined from

$$\beta = [\ (1 + S_W/\gamma)\ \frac{\Delta T}{\Delta T_W} - 1\ ]^{-1}. \qquad \text{(A2.12)}$$

This expression is useful for determing β with a differential psychrometer system as it reduces the need for extreme accuracy in absolute temperature measurement. Absolute measurements of T_W are only required to determine S_W, the slope of the saturation vapour pressure curve at T_W.

Fuchs and Tanner (1970) show that the relative error in β, can be expressed

$$\frac{\delta\beta}{\beta} = (\ 1 + \beta)\ [\frac{\delta\Delta T}{\Delta T} + \frac{\delta\Delta T_W}{\Delta T_W} + (\delta S_W/(S_W + \gamma))] \qquad \text{(A2.13)}$$

The relative errors in the measurement of ΔT and ΔT_W have already being discussed and presented (Table A2.4).

Assuming an atmospheric pressure of 75 KPa, and an error of ±0.32°C in the measurement of T_W, the $\delta S_W/(S_W + \gamma)$ term will range from 0.0096 at 0°C to 0.0134 at 25°C. Hence, in comparison to the measurement error associated with ΔT and ΔT_W, the contribution of this factor to the relative error in β will be small. This will be particularly true when ΔT and ΔT_W are small.

Error Analysis for Q_G

A probable relative error of ±10% was assumed for the Q_G measurements. This is considered a liberal estimate of the error associated with the measurement of soil heat flux density.

Error Analysis for Q_H and Q_E

Differentiating equations 2.20 and 2.21 results in the following expression for the relative error in Q_E and Q_H;

$$\frac{\delta Q_E}{Q_E} = \frac{\delta Q^* + \delta Q_G}{Q^* - Q_G} + \frac{\delta \beta}{(1 + \beta)} \tag{A2.14}$$

$$\frac{\delta Q_H}{Q_H} = \frac{\delta Q^* + \delta Q_G}{Q^* - Q_G} + \frac{\delta \beta}{\beta(1 + \beta)} \tag{A2.15}$$

In Table A2.6 a sample tabulation of the error associated with the BREB determined Q_H and Q_E, for a range of ΔT , ΔT_W and Q^* values is presented. These calculations were done assuming $T = 15°C$, $T_W = 10°C$ and Q_G is 15% of Q^* ($e = 978$ Pa, relative humidity = 57.4%).

The tabulated data clearly shows the difficulty of using the the BREB approach to determine Q_E and Q_H when Δe and ΔT are small. The results show that Δe must be greater than 15 Pa for the relative error in Q_E to be less than ±50%, and greater than 50 Pa for the relative error to be less than ±20%. The results also show that the relative error in Q_H does not ever fall below ±20%, and is considerable larger when ΔT is less than 0.1°C or Δe is less than 20 Pa. Fortunately the conditions which favour the largest relative measurement errors for both Q_H and Q_E occur when the fluxes themselves are small. Hence, even when $Q^* = 400$ W m^{-2}, absolute errors in Q_H and Q_E will only exceed ±50 W m^{-2} for very low values of ΔT_W and ΔT .

On the basis of preceding analysis, and considering the warm, dry conditions experienced during this experiment, a reasonable estimate of the relative measurement error for both Q_H and Q_E would be ±20%.

Table A2.6. Error analysis results for Q_H and Q_E

$Q^* = 50$ W m^{-2}

ΔT (°C)	ΔT_w (°C)	Δe (Pa)	Q_H (W m^{-2})	δQ_H (W m^{-2})	$\delta Q_H/Q_H$ (%)	Q_E (W m^{-2})	δQ_E (W m^{-2})	$\delta Q_E/Q_E$ (%)
0.05	0.05	9.4	8.90	8.64	97.0	33.60	11.11	33.1
0.05	0.15	33.3	2.97	2.06	69.3	39.53	5.71	14.4
0.05	0.25	57.2	1.78	1.14	64.1	40.72	5.04	12.4
0.05	0.35	81.0	1.27	0.79	62.2	41.23	4.79	11.6
0.05	0.45	104.9	0.99	0.61	61.2	41.51	4.66	11.2
0.05	0.55	128.8	0.81	0.49	60.7	41.69	4.58	11.0
0.05	0.65	152.6	0.68	0.41	60.3	41.82	4.53	10.8
0.05	0.75	176.5	0.59	0.36	60.1	41.91	4.49	10.7
0.05	0.85	200.4	0.52	0.31	59.9	41.98	4.46	10.6
0.05	0.95	224.2	0.47	0.28	59.8	42.03	4.44	10.6
0.10	0.05	6.9	17.81	13.54	76.1	24.69	14.23	57.6
0.10	0.15	30.8	5.94	2.87	48.3	36.56	5.93	16.2
0.10	0.25	54.7	3.56	1.54	43.2	38.94	5.08	13.0
0.10	0.35	78.5	2.54	1.05	41.2	39.96	4.79	12.0
0.10	0.45	102.4	1.98	0.80	40.2	40.52	4.65	11.5
0.10	0.55	126.3	1.62	0.64	39.7	40.88	4.57	11.2
0.10	0.65	150.1	1.37	0.54	39.4	41.13	4.52	11.0
0.10	0.75	174.0	1.19	0.46	39.1	41.31	4.48	10.8
0.10	0.85	197.9	1.05	0.41	39.0	41.45	4.45	10.7
0.10	0.95	221.7	0.94	0.36	38.9	41.56	4.43	10.7
0.25	0.05	-0.6	44.52	-21.94	-49.3	-2.02	26.19	-1296.1
0.25	0.15	23.3	14.84	5.40	36.4	27.66	6.68	24.2
0.25	0.25	47.2	8.90	2.78	31.3	33.60	5.25	15.6
0.25	0.35	71.0	6.36	1.86	29.3	36.14	4.84	13.4
0.25	0.45	94.9	4.95	1.40	28.3	37.55	4.66	12.4
0.25	0.55	118.8	4.05	1.12	27.8	38.45	4.57	11.9
0.25	0.65	142.6	3.42	0.94	27.4	39.08	4.51	11.5
0.25	0.75	166.5	2.97	0.81	27.2	39.53	4.46	11.3
0.25	0.85	190.4	2.62	0.71	27.1	39.88	4.44	11.1
0.25	0.95	214.2	2.34	0.63	27.0	40.16	4.41	11.0
0.50	0.05	-13.1	89.04	-135.65	-152.3	-46.54	139.90	-300.6
0.50	0.15	10.8	29.68	9.84	33.2	12.82	8.15	63.6
0.50	0.25	34.7	17.81	4.99	28.0	24.69	5.68	23.0
0.50	0.35	58.5	12.72	3.31	26.0	29.78	5.02	16.9
0.50	0.45	82.4	9.89	2.48	25.1	32.61	4.75	14.6
0.50	0.55	106.3	8.09	1.99	24.5	34.41	4.62	13.4
0.50	0.65	130.1	6.85	1.66	24.2	35.65	4.54	12.7
0.50	0.75	154.0	5.94	1.42	24.0	36.56	4.49	12.3
0.50	0.85	177.9	5.24	1.25	23.8	37.26	4.45	11.9
0.50	0.95	201.7	4.69	1.11	23.7	37.81	4.42	11.7
0.75	0.05	-25.6	133.56	-340.26	-254.8	-91.06	344.51	-378.3
0.75	0.15	-1.7	44.52	-6.45	-14.5	-2.02	10.70	-529.3
0.75	0.25	22.2	26.71	7.27	27.2	15.79	6.18	39.1
0.75	0.35	46.0	19.08	4.82	25.3	23.42	5.25	22.4
0.75	0.45	69.9	14.84	3.60	24.3	27.66	4.89	17.7
0.75	0.55	93.8	12.14	2.88	23.7	30.36	4.70	15.5
0.75	0.65	117.6	10.27	2.40	23.4	32.23	4.60	14.3
0.75	0.75	141.5	8.90	2.06	23.2	33.60	4.53	13.5
0.75	0.85	165.4	7.86	1.81	23.0	34.64	4.49	13.0
0.75	0.95	189.2	7.03	1.61	22.9	35.47	4.46	12.6

Table A2.6. (continued).

$Q^* = 100\ W\ m^{-2}$

ΔT (°C)	ΔT_w (°C)	Δe (Pa)	Q_H (W m⁻²)	δQ_H (W m⁻²)	$\delta Q_H/Q_H$ (%)	Q_E (W m⁻²)	δQ_E (W m⁻²)	$\delta Q_E/Q_E$ (%)
0.05	0.05	9.4	17.81	17.28	97.0	67.19	22.21	33.1
0.05	0.15	33.3	5.94	4.11	69.3	79.06	11.42	14.4
0.05	0.25	57.2	3.56	2.28	64.1	81.44	10.07	12.4
0.05	0.35	81.0	2.54	1.58	62.2	82.46	9.57	11.6
0.05	0.45	104.9	1.98	1.21	61.2	83.02	9.32	11.2
0.05	0.55	128.8	1.62	0.98	60.7	83.38	9.16	11.0
0.05	0.65	152.6	1.37	0.83	60.3	83.63	9.05	10.8
0.05	0.75	176.5	1.19	0.71	60.1	83.81	8.98	10.7
0.05	0.85	200.4	1.05	0.63	59.9	83.95	8.92	10.6
0.05	0.95	224.2	0.94	0.56	59.8	84.06	8.87	10.6
0.10	0.05	6.9	35.62	27.09	76.1	49.38	28.47	57.6
0.10	0.15	30.8	11.87	5.74	48.3	73.13	11.86	16.2
0.10	0.25	54.7	7.12	3.08	43.2	77.88	10.15	13.0
0.10	0.35	78.5	5.09	2.10	41.2	79.91	9.58	12.0
0.10	0.45	102.4	3.96	1.59	40.2	81.04	9.30	11.5
0.10	0.55	126.3	3.24	1.29	39.7	81.76	9.14	11.2
0.10	0.65	150.1	2.74	1.08	39.4	82.26	9.03	11.0
0.10	0.75	174.0	2.37	0.93	39.1	82.63	8.95	10.8
0.10	0.85	197.9	2.10	0.82	39.0	82.90	8.90	10.7
0.10	0.95	221.7	1.87	0.73	38.9	83.13	8.85	10.7
0.25	0.05	-0.6	89.04	-43.89	-49.3	-4.04	52.39	-1296.1
0.25	0.15	23.3	29.68	10.80	36.4	55.32	13.37	24.2
0.25	0.25	47.2	17.81	5.57	31.3	67.19	10.51	15.6
0.25	0.35	71.0	12.72	3.73	29.3	72.28	9.68	13.4
0.25	0.45	94.9	9.89	2.80	28.3	75.11	9.32	12.4
0.25	0.55	118.8	8.09	2.25	27.8	76.91	9.13	11.9
0.25	0.65	142.6	6.85	1.88	27.4	78.15	9.01	11.5
0.25	0.75	166.5	5.94	1.62	27.2	79.06	8.93	11.3
0.25	0.85	190.4	5.24	1.42	27.1	79.76	8.87	11.1
0.25	0.95	214.2	4.69	1.26	27.0	80.31	8.83	11.0
0.50	0.05	-13.1	178.08	-271.30	-152.3	-93.08	279.80	-300.6
0.50	0.15	10.8	59.36	19.68	33.2	25.64	16.31	63.6
0.50	0.25	34.7	35.62	9.98	28.0	49.38	11.36	23.0
0.50	0.35	58.5	25.44	6.63	26.0	59.56	10.04	16.9
0.50	0.45	82.4	19.79	4.96	25.1	65.21	9.50	14.6
0.50	0.55	106.3	16.19	3.97	24.5	68.81	9.23	13.4
0.50	0.65	130.1	13.70	3.31	24.2	71.30	9.07	12.7
0.50	0.75	154.0	11.87	2.85	24.0	73.13	8.97	12.3
0.50	0.85	177.9	10.48	2.50	23.8	74.52	8.90	11.9
0.50	0.95	201.7	9.37	2.22	23.7	75.63	8.85	11.7
0.75	0.05	-25.6	267.13	-680.52	-254.8	-182.13	689.02	-378.3
0.75	0.15	-1.7	89.04	-12.89	-14.5	-4.04	21.39	-529.3
0.75	0.25	22.2	53.43	14.55	27.2	31.57	12.36	39.1
0.75	0.35	46.0	38.16	9.64	25.3	46.84	10.50	22.4
0.75	0.45	69.9	29.68	7.21	24.3	55.32	9.77	17.7
0.75	0.55	93.8	24.28	5.76	23.7	60.72	9.41	15.5
0.75	0.65	117.6	20.55	4.81	23.4	64.45	9.20	14.3
0.75	0.75	141.5	17.81	4.13	23.2	67.19	9.07	13.5
0.75	0.85	165.4	15.71	3.62	23.0	69.29	8.98	13.0
0.75	0.95	189.2	14.06	3.22	22.9	70.94	8.91	12.6

Table A2.6. (continued).

$Q^* = 200\ W\ m^{-2}$

ΔT (°C)	ΔT_w (°C)	Δe (Pa)	Q_H ($W\ m^{-2}$)	δQ_H ($W\ m^{-2}$)	$\delta Q_H/Q_H$ (%)	Q_E ($W\ m^{-2}$)	δQ_E ($W\ m^{-2}$)	$\delta Q_E/Q_E$ (%)
0.05	0.05	9.4	35.62	34.55	87.0	134.38	44.43	33.1
0.05	0.15	33.3	11.87	8.22	69.3	158.13	22.85	14.4
0.05	0.25	57.2	7.12	4.57	64.1	162.88	20.14	12.4
0.05	0.35	81.0	5.09	3.16	62.2	164.91	19.15	11.6
0.05	0.45	104.9	3.96	2.42	61.2	166.04	18.63	11.2
0.05	0.55	128.8	3.24	1.96	60.7	166.76	18.32	11.0
0.05	0.65	152.6	2.74	1.65	60.3	167.26	18.10	10.8
0.05	0.75	176.5	2.37	1.43	60.1	167.63	17.95	10.7
0.05	0.85	200.4	2.10	1.26	59.9	167.90	17.84	10.6
0.05	0.95	224.2	1.87	1.12	59.8	168.13	17.75	10.6
0.10	0.05	6.9	71.23	54.18	76.1	98.77	56.93	57.6
0.10	0.15	30.8	23.74	11.47	48.3	146.26	23.72	16.2
0.10	0.25	54.7	14.25	6.15	43.2	155.75	20.30	13.0
0.10	0.35	78.5	10.18	4.19	41.2	159.82	19.16	12.0
0.10	0.45	102.4	7.91	3.19	40.2	162.09	18.60	11.5
0.10	0.55	126.3	6.48	2.57	39.7	163.52	18.28	11.2
0.10	0.65	150.1	5.48	2.16	39.4	164.52	18.06	11.0
0.10	0.75	174.0	4.75	1.86	39.1	165.25	17.91	10.8
0.10	0.85	197.9	4.19	1.63	39.0	165.81	17.80	10.7
0.10	0.95	221.7	3.75	1.46	38.9	166.25	17.71	10.7
0.25	0.05	-0.6	178.08	-87.77	-49.3	-8.08	104.77	-1296.1
0.25	0.15	23.3	59.36	21.61	36.4	110.64	26.74	24.2
0.25	0.25	47.2	35.62	11.14	31.3	134.38	21.01	15.6
0.25	0.35	71.0	25.44	7.45	29.3	144.56	19.37	13.4
0.25	0.45	94.9	19.79	5.61	28.3	150.21	18.65	12.4
0.25	0.55	118.8	16.19	4.50	27.8	153.81	18.26	11.9
0.25	0.65	142.6	13.70	3.76	27.4	156.30	18.02	11.5
0.25	0.75	166.5	11.87	3.23	27.2	158.13	17.86	11.3
0.25	0.85	190.4	10.48	2.84	27.1	159.52	17.74	11.1
0.25	0.95	214.2	9.37	2.53	27.0	160.63	17.65	11.0
0.50	0.05	-13.1	356.17	-542.60	-152.3	-186.17	559.60	-300.6
0.50	0.15	10.8	118.72	39.36	33.2	51.28	32.61	63.6
0.50	0.25	34.7	71.23	19.96	28.0	98.77	22.71	23.0
0.50	0.35	58.5	50.88	13.25	26.0	119.12	20.08	16.9
0.50	0.45	82.4	39.57	9.92	25.1	130.43	19.01	14.6
0.50	0.55	106.3	32.38	7.94	24.5	137.62	18.47	13.4
0.50	0.65	130.1	27.40	6.63	24.2	142.60	18.15	12.7
0.50	0.75	154.0	23.74	5.69	24.0	146.26	17.94	12.3
0.50	0.85	177.9	20.95	4.99	23.8	149.05	17.80	11.9
0.50	0.95	201.7	18.75	4.45	23.7	151.25	17.70	11.7
0.75	0.05	-25.6	534.25	-1361.05	-254.8	-364.25	1378.05	-378.3
0.75	0.15	-1.7	178.08	-25.79	-14.5	-8.08	42.79	-529.3
0.75	0.25	22.2	106.85	29.09	27.2	63.15	24.72	39.1
0.75	0.35	46.0	76.32	19.27	25.3	93.68	21.01	22.4
0.75	0.45	69.9	59.36	14.41	24.3	110.64	19.54	17.7
0.75	0.55	93.8	48.57	11.53	23.7	121.43	18.81	15.5
0.75	0.65	117.6	41.10	9.62	23.4	128.90	18.40	14.3
0.75	0.75	141.5	35.62	8.26	23.2	134.38	18.13	13.5
0.75	0.85	165.4	31.43	7.24	23.0	138.57	17.95	13.0
0.75	0.95	189.2	28.12	6.44	22.9	141.88	17.82	12.6

Table A2.6. (continued).

$Q^* = 400$ W m^{-2}

ΔT (°C)	ΔT_w (°C)	Δe (Pa)	Q_H (W m^{-2})	δQ_H (W m^{-2})	$\delta Q_H/Q_H$ (%)	Q_E (W m^{-2})	δQ_E (W m^{-2})	$\delta Q_E/Q_E$ (%)
0.05	0.05	9.4	71.23	69.10	97.0	268.77	88.85	33.1
0.05	0.15	33.3	23.74	16.45	69.3	316.26	45.70	14.4
0.05	0.25	57.2	14.25	9.14	64.1	325.75	40.29	12.4
0.05	0.35	81.0	10.18	6.33	62.2	329.82	38.29	11.6
0.05	0.45	104.9	7.91	4.84	61.2	332.09	37.26	11.2
0.05	0.55	128.8	6.48	3.93	60.7	333.52	36.63	11.0
0.05	0.65	152.6	5.48	3.30	60.3	334.52	36.21	10.8
0.05	0.75	176.5	4.75	2.85	60.1	335.25	35.90	10.7
0.05	0.85	200.4	4.19	2.51	59.9	335.81	35.67	10.6
0.05	0.95	224.2	3.75	2.24	59.8	336.25	35.49	10.6
0.10	0.05	6.9	142.47	108.36	76.1	197.53	113.86	57.6
0.10	0.15	30.8	47.49	22.95	48.3	292.51	47.45	16.2
0.10	0.25	54.7	28.49	12.31	43.2	311.51	40.61	13.0
0.10	0.35	78.5	20.35	8.39	41.2	319.65	38.32	12.0
0.10	0.45	102.4	15.83	6.37	40.2	324.17	37.21	11.5
0.10	0.55	126.3	12.95	5.14	39.7	327.05	36.55	11.2
0.10	0.65	150.1	10.96	4.31	39.4	329.04	36.12	11.0
0.10	0.75	174.0	9.50	3.72	39.1	330.50	35.82	10.8
0.10	0.85	197.9	8.38	3.27	39.0	331.62	35.59	10.7
0.10	0.95	221.7	7.50	2.92	38.9	332.50	35.42	10.7
0.25	0.05	-0.6	356.17	-175.55	-49.3	-16.17	209.55	-1296.1
0.25	0.15	23.3	118.72	43.22	36.4	221.28	53.47	24.2
0.25	0.25	47.2	71.23	22.28	31.3	268.77	42.03	15.6
0.25	0.35	71.0	50.88	14.91	29.3	289.12	38.73	13.4
0.25	0.45	94.9	39.57	11.21	28.3	300.43	37.30	12.4
0.25	0.55	118.8	32.38	9.00	27.8	307.62	36.52	11.9
0.25	0.65	142.6	27.40	7.52	27.4	312.60	36.04	11.5
0.25	0.75	166.5	23.74	6.46	27.2	316.26	35.72	11.3
0.25	0.85	190.4	20.95	5.67	27.1	319.05	35.48	11.1
0.25	0.95	214.2	18.75	5.05	27.0	321.25	35.31	11.0
0.50	0.05	-13.1	712.33	-1085.20	-152.3	-372.33	1119.20	-300.6
0.50	0.15	10.8	237.44	78.71	33.2	102.56	65.22	63.6
0.50	0.25	34.7	142.47	39.92	28.0	197.53	45.43	23.0
0.50	0.35	58.5	101.76	26.51	26.0	238.24	40.16	16.9
0.50	0.45	82.4	79.15	19.85	25.1	260.85	38.02	14.6
0.50	0.55	106.3	64.76	15.89	24.5	275.24	36.93	13.4
0.50	0.65	130.1	54.79	13.26	24.2	285.21	36.30	12.7
0.50	0.75	154.0	47.49	11.39	24.0	292.51	35.89	12.3
0.50	0.85	177.9	41.90	9.98	23.8	298.10	35.60	11.9
0.50	0.95	201.7	37.49	8.89	23.7	302.51	35.39	11.7
0.75	0.05	-25.6	1068.50	-2722.09	-254.8	-728.50	2756.09	-378.3
0.75	0.15	-1.7	356.17	-51.58	-14.5	-16.17	85.58	-529.3
0.75	0.25	22.2	213.70	58.18	27.2	126.30	49.44	39.1
0.75	0.35	46.0	152.64	38.55	25.3	187.36	42.02	22.4
0.75	0.45	69.9	118.72	28.83	24.3	221.28	39.09	17.7
0.75	0.55	93.8	97.14	23.06	23.7	242.86	37.63	15.5
0.75	0.65	117.6	82.19	19.23	23.4	257.81	36.79	14.3
0.75	0.75	141.5	71.23	16.51	23.2	268.77	36.26	13.5
0.75	0.85	165.4	62.85	14.47	23.0	277.15	35.90	13.0
0.75	0.95	189.2	56.24	12.89	22.9	283.76	35.64	12.6

APPENDIX 3 - DAILY, DAYLIGHT AND NIGHT PERIOD RADIATION BALANCE VALUES

Day		K_0	t	$K\downarrow$	a	$K\uparrow$	K^*	$L\downarrow$	$L\uparrow$	L^*	Q^*
June 26	daily	41.7	0.793	33.1	0.172	5.7	27.4	17.3	29.0	-11.7	15.7
	daylight	41.7	0.793	33.1	0.172	5.7	27.4	12.1	21.4	-9.3	18.1
	night							5.3	7.6	-2.4	-2.4
June 27	daily	41.7	0.742	31.0	0.170	5.3	25.7	19.2	29.8	-10.5	15.2
	daylight	41.7	0.742	31.0	0.170	5.3	25.7	13.5	21.8	-8.3	17.4
	night							5.7	8.0	-2.2	-2.2
June 28	daily	41.7	0.555	23.1	0.163	3.8	19.4	21.8	29.7	-7.9	11.5
	daylight	41.7	0.555	23.1	0.163	3.8	19.4	15.4	21.5	-6.1	13.3
	night							6.3	8.1	-1.8	-1.8
June 29	daily	41.6	0.663	27.6	0.163	4.5	23.1	21.4	29.7	-8.2	14.9
	daylight	41.6	0.663	27.6	0.163	4.5	23.1	15.4	21.5	-6.2	16.9
	night							6.1	8.1	-2.1	-2.1
June 30	daily	41.6	0.639	26.6	0.170	4.5	22.0	20.4	30.0	-9.7	12.4
	daylight	41.6	0.639	26.6	0.170	4.5	22.0	14.4	21.9	-7.5	14.5
	night							6.0	8.1	-2.2	-2.2
July 1	daily	41.6	0.765	31.8	0.169	5.4	26.4	19.3	30.8	-11.5	14.9
	daylight	41.6	0.765	31.8	0.169	5.4	26.4	13.6	22.5	-8.9	17.5
	night							5.7	8.3	-2.6	-2.6
July 2	daily	41.5	0.755	31.3	0.170	5.3	26.0	19.3	30.8	-11.6	14.4
	daylight	41.5	0.755	31.3	0.170	5.3	26.0	13.2	22.5	-9.3	16.7
	night							6.1	8.3	-2.2	-2.2
July 3	daily	41.4	0.726	30.1	0.167	5.0	25.1	21.0	31.7	-10.7	14.4
	daylight	41.4	0.726	30.1	0.167	5.0	25.1	14.4	23.1	-8.6	16.5
	night							6.5	8.6	-2.1	-2.1
July 4	daily	41.4	0.718	29.7	0.168	5.0	24.7	20.9	32.1	-11.2	13.5
	daylight	41.4	0.718	29.7	0.168	5.0	24.7	14.6	23.7	-9.2	15.6
	night							6.3	8.4	-2.1	-2.1
July 5	daily	41.3	0.749	30.9	0.172	5.3	25.6	20.2	31.4	-11.2	14.4
	daylight	41.3	0.749	30.9	0.172	5.3	25.6	14.0	22.6	-8.6	17.0
	night							6.2	8.8	-2.5	-2.5

Day		K_0	t	K↓	a	K↑	K*	L↓	L↑	L*	Q*
July 6	daily	41.2	0.750	30.9	0.174	5.4	25.5	18.5	30.5	-12.0	13.6
	daylight	41.2	0.750	30.9	0.174	5.4	25.5	12.9	22.2	-9.3	16.3
	night							5.6	8.3	-2.7	-2.7
July 7	daily	41.2	0.651	26.8	0.170	4.5	22.2	21.6	30.9	-9.3	13.0
	daylight	41.2	0.651	26.8	0.170	4.5	22.2	15.2	22.5	-7.3	15.0
	night							6.4	8.4	-2.0	-2.0
July 8	daily	41.1	0.729	29.9	0.173	5.2	24.7	20.3	31.9	-11.6	13.2
	daylight	41.1	0.729	29.9	0.173	5.2	24.7	13.3	23.2	-9.2	15.5
	night							6.3	8.7	-2.3	-2.3
July 9	daily	41.0	0.638	26.1	0.170	4.5	21.7	22.9	31.9	-9.0	12.6
	daylight	41.0	0.638	26.1	0.170	4.5	21.7	16.4	23.3	-6.9	14.8
	night							6.4	8.6	-2.2	-2.2
July 10	daily	40.9	0.674	27.5	0.177	4.9	22.7	21.7	31.2	-9.6	13.1
	daylight	40.9	0.674	27.5	0.177	4.9	22.7	14.6	22.4	-7.8	14.9
	night							7.0	8.8	-1.8	-1.8
July 11	daily	40.8	0.654	26.7	0.175	4.7	22.0	20.6	31.4	-10.8	11.2
	daylight	40.8	0.654	26.7	0.175	4.7	22.0	14.2	22.9	-8.6	13.4
	night							-2.0	6.4	-8.4	8.5
July 12	daily	40.7	0.361	14.7	0.177	2.6	12.0	22.5	29.3	-6.8	5.3
	daylight	40.7	0.361	14.7	0.177	2.6	12.0	15.8	20.9	-5.1	7.0
	night							6.7	8.4	-1.7	-1.7
July 13	daily	40.6	0.400	16.2	0.180	2.9	13.3	22.6	28.0	-5.4	7.9
	daylight	40.6	0.400	16.2	0.180	2.9	13.3	15.1	19.8	-4.7	8.6
	night							7.4	8.1	-0.7	-0.7
July 14	daily	40.4	msg	msg	msg	msg	msg	msg	msg	msg	msg
	daylight	40.4	msg	msg	msg	msg	msg	msg	msg	msg	msg
	night							msg	msg	msg	msg
July 15	daily	40.3	0.536	21.6	0.170	3.7	18.0	22.5	30.0	-7.5	10.5
	daylight	40.3	0.536	21.6	0.170	3.7	18.0	15.4	21.6	-6.1	11.8
	night							7.1	8.4	-1.4	-1.4

Day		K_e	t	K↓	a	K↑	K*	L↓	L↑	L*	Q*
July 16	daily	40.2	0.303	12.2	0.159	1.94	10.3	24.3	27.8	-3.5	6.8
	daylight	40.2	0.303	12.2	0.159	1.94	10.3	16.8	19.6	-2.7	7.5
	night							7.4	8.2	-0.8	-0.8
July 17	daily	40.1	0.258	10.3	0.211	2.2	8.1	24.0	26.3	-2.4	5.8
	daylight	40.1	0.258	10.3	0.211	2.2	8.1	16.4	18.2	-1.8	6.3
	night							7.5	8.0	-0.5	-0.5
July 18	daily	40.0	0.730	29.2	0.165	4.8	24.4	19.1	28.6	-9.4	14.9
	daylight	40.0	0.730	29.2	0.165	4.8	24.4	13.3	20.7	-7.4	16.9
	night							5.8	7.8	-2.0	-2.0
July 19	daily	39.8	0.635	25.3	0.169	4.3	21.0	20.8	29.2	-8.4	12.6
	daylight	39.8	0.635	25.3	0.169	4.3	21.0	14.5	21.1	-6.5	14.4
	night							6.3	8.1	-1.9	-1.9
July 20	daily	40.0	0.671	26.6	0.169	4.5	22.1	20.8	30.7	-9.9	12.2
	daylight	40.0	0.671	26.6	0.169	4.5	22.1	14.5	22.4	-7.8	14.3
	night							6.3	8.3	-2.0	-2.0
July 21	daily	39.5	0.738	29.2	0.174	5.1	24.1	21.0	31.9	-10.9	13.2
	daylight	39.5	0.738	29.2	0.174	5.1	24.1	14.7	23.4	-8.7	15.4
	night							6.3	8.5	-2.2	-2.2
July 22	daily	39.4	0.563	22.2	0.174	3.9	18.3	22.3	30.8	-8.5	9.8
	daylight	39.4	0.563	22.2	0.174	3.9	18.3	15.6	22.2	-6.6	11.7
	night							6.7	8.6	-1.9	-1.9
July 23	daily	39.2	0.463	18.2	0.165	3.0	15.2	23.8	28.6	-4.8	10.4
	daylight	39.2	0.463	18.2	0.165	3.0	15.2	15.8	20.1	-4.3	10.8
	night							8.0	8.4	-0.4	-0.4
July 24	daily	39.1	0.698	27.2	0.170	4.6	22.6	20.7	29.2	-8.4	14.1
	daylight	39.0	0.698	27.2	0.170	4.6	22.6	13.2	19.9	-6.6	16.0
	night							7.5	9.3	-1.8	-1.8
July 25	daily	38.9	0.772	30.0	0.170	5.1	24.9	18.8	30.4	-11.6	13.4
	daylight	38.9	0.772	30.0	0.170	5.1	24.9	12.1	21.1	-9.0	16.0
	night							6.7	9.3	-2.6	-2.6

Day		K_0	t	$K\downarrow$	a	$K\uparrow$	K^*	$L\downarrow$	$L\uparrow$	L^*	Q^*
July 26	daily	38.7	0.737	28.6	0.172	4.9	23.6	18.8	30.3	-11.5	12.1
	daylight	38.7	0.737	28.6	0.172	4.9	23.6	12.4	21.3	-8.9	14.7
	night							6.3	9.0	-2.6	-2.6

All values are in MJ m^{-2}, except t and a which are dimensionless.

The missing data on July 14 (indicated by msg) is due to a data recording problem which resulted in the loss of a portion of the data for this day.

. All flux density values are based on the sum of the half-hourly means. The daylight period was defined as all the half-hourly periods where the mean K_0 value was greater than 0. The night period was defined as all the half-hourly periods where the mean K_0 value was 0.

K_0 is the theoretical solar radiation receipt for a site at this latitude, assuming no horizon shading, calculated using the approach suggested by Sellers (1965).

$K\downarrow$, $K\uparrow$ and Q^* were measured directly.

L was calculated using surface temperature measurements and the Stefan-Boltzmann expression (equation 2.5). Surface emissivity was assumed to be constant at 0.90.

$L\downarrow$ was calculated by substituting the measured $K\downarrow$, $K\uparrow$, Q^* and calculated $L\uparrow$ into the radiation balance expression (equation 2.1) and solving it for $L\downarrow$.

t was calculated from the mean daily and daylight period values of K_0 and $K\downarrow$.

a was calculated from the mean daily and daylight period values of $K\uparrow$ and $K\downarrow$.

APPENDIX 4 - DAILY, DAYLIGHT AND NIGHT PERIOD ENERGY BALANCE VALUES

Day		Q^*	Q_H	Q_E	Q_G	β	α
June 27	daily	15.2	6.9	6.4	1.9	1.078	0.803
	daylight	17.4	8.4	6.1	2.9	1.372	0.680
	night	-2.2	-1.5	0.3	-1.0	-5.354	
June 28	daily	11.5	4.9	4.9	1.6	1.001	0.827
	daylight	13.3	6.3	4.5	2.5	1.385	0.694
	night	-1.8	-1.3	0.4	-0.9	-3.278	
June 29	daily	14.9	8.2	5.3	1.3	1.541	0.644
	daylight	16.9	9.7	5.1	2.2	1.925	0.535
	night	-2.1	-1.5	0.3	-0.9	-5.137	
June 30	daily	12.4	3.3	7.6	1.5	0.438	1.099
	daylight	14.5	5.2	6.9	2.4	0.751	0.868
	night	-2.2	-1.9	0.6	-0.9	-2.944	
July 1	daily	14.9	2.9	10.5	1.5	0.277	1.209
	daylight	17.5	6.9	8.0	2.5	0.863	0.804
	night	-2.6	-4.0	2.4	-1.0	-1.662	
July 2	daily	14.4	msg	msg	1.5	msg	msg
	daylight	16.7	msg	msg	2.5	msg	msg
	night	-2.2	msg	msg	-1.0	msg	
July 3	daily	14.4	msg	msg	2.0	msg	msg
	daylight	16.5	msg	msg	2.6	msg	msg
	night	-2.1	msg	msg	-0.6	msg	
July 4	daily	13.5	8.2	3.2	2.0	2.548	0.412
	daylight	15.6	9.6	3.1	2.9	3.099	0.347
	night	-2.1	-1.4	0.1	-0.9	-10.089	
July 5	daily	14.4	11.8	1.7	1.2	7.126	0.183
	daylight	17.0	13.8	1.5	1.7	9.114	0.145
	night	-2.5	-2.0	0.1	-0.7	-14.511	

Day		Q^*	Q_H	Q_E	Q_G	β	α
July 6	daily	13.6	9.8	3.0	0.7	3.236	0.370
	daylight	16.3	11.7	2.9	1.7	4.037	0.302
	night	-2.7	-1.9	0.1	-1.0	-13.896	
July 7	daily	13.0	9.2	2.4	1.3	3.900	0.314
	daylight	15.0	10.5	2.3	2.2	4.579	0.267
	night	-2.0	-1.3	0.1	-0.8	-18.786	
July 8	daily	13.2	9.9	1.6	1.7	6.373	0.198
	daylight	15.5	11.7	1.4	2.4	8.271	0.154
	night	-2.3	-1.8	0.1	-0.6	-13.585	
July 9	daily	12.6	msg	msg	msg	msg	msg
	daylight	14.8	msg	msg	msg	msg	msg
	night	-2.2	msg	msg	msg	msg	
July 10	daily	13.1	6.4	5.4	1.2	1.180	0.666
	daylight	14.9	7.8	5.3	1.8	1.455	0.581
	night	-1.8	-1.3	0.1	-0.6	-10.740	
July 11	daily	11.2	msg	msg	1.2	msg	msg
	daylight	13.4	msg	msg	2.0	msg	msg
	night	-2.2	msg	msg	-0.8	msg	
July 12	daily	5.3	2.2	1.4	0.7	1.575	0.629
	daylight	7.0	4.3	1.8	2.3	0.820	0.479
	night	-2.1	-0.5	-0.8	4.6		
July 13	daily	7.9	msg	msg	0.2	msg	msg
	daylight	8.6	msg	msg	0.9	msg	msg
	night	-0.7	msg	msg	-0.7	msg	
July 14	daily	msg	msg	msg	msg	msg	msg
	daylight	msg	msg	msg	msg	msg	msg
	night	msg	msg	msg	msg	msg	

Day		Q^*	Q_H	Q_E	Q_G	β	α
July 15	daily	10.5	6.9	2.7	0.9	2.507	0.477
	daylight	11.8	8.5	1.7	1.5	4.888	0.283
	night	-1.4	-1.6	1.0	-0.7	-1.624	
July 16	daily	6.8	msg	msg	-0.1	msg	msg
	daylight	7.5	msg	msg	0.6	msg	msg
	night	-0.8	msg	msg	-0.7	msg	
July 17	daily	5.8	msg	msg	-0.5	msg	msg
	daylight	6.3	msg	msg	0.2	msg	msg
	night	-0.5	msg	msg	-0.7	msg	
July 18	daily	14.9	4.6	8.9	1.4	0.525	1.099
	daylight	16.9	5.9	8.7	2.4	0.678	0.960
	night	-2.0	-1.2	0.2	-0.9	-7.238	
July 19	daily	12.6	8.0	3.3	1.3	2.392	0.495
	daylight	14.4	9.1	3.2	2.2	2.862	0.432
	night	-1.9	-1.1	0.2	-0.9	-6.677	
July 20	daily	12.2	4.7	6.2	1.5	0.753	0.884
	daylight	14.3	6.1	6.0	2.3	1.008	0.746
	night	-2.0	-1.4	0.2	-0.8	-8.747	
July 21	daily	13.2	4.9	7.0	1.5	0.697	0.878
	daylight	15.4	6.5	6.8	2.4	0.961	0.735
	night	-2.2	-1.6	0.3	-0.9	-6.213	
July 22	daily	9.8	4.4	5.1	0.5	0.861	0.816
	daylight	11.7	5.8	4.6	1.4	1.259	0.658
	night	-1.9	-1.5	0.4	-0.9	-3.311	
July 23	daily	10.4	2.6	7.8	0.2	0.330	1.306
	daylight	10.8	3.7	6.5	0.6	0.590	1.093
	night	-1.1	1.3	-0.6	-0.9		
July 24	daily	14.1	6.4	7.0	0.8	0.914	0.876
	daylight	17.0	7.9	7.3	1.8	1.087	0.779
	night	-2.9	-1.6	-0.3	-1.0	4.814	

Day		Q^*	Q_H	Q_E	Q_G	β	α
July 25	daily	13.4	5.6	6.7	1.0	0.823	0.862
	daylight	16.0	7.3	6.5	2.1	1.118	0.707
	night	-2.6	-2.1	-0.2	-1.1	12.280	
July 26	daily	12.0	6.3	4.5	1.2	1.415	0.665
	daylight	14.7	8.3	4.2	2.3	1.969	0.533
	night	-2.7	-1.9	0.3	-1.1	-7.272	

All values are in MJ m^{-2}, except β and α which are dimensionless.

Missing data is indicated by msg.

Missing Q_H and Q_E data on July 2 is due to the intercomparison of the differential psychrometer sensors conducted on this day.

Missing Q_H and Q_E data on July 3 is due to water feed problems experienced with the differential psychrometer system.

Missing Q_G data on July 9 prevented the use of the BREB approach to determine Q_H and Q_E on this day. The Q_G data was not available due to data recording problems.

Missing Q_H and Q_E data on July 11 is due to the intercomparison of the differential psychrometer sensors conducted on this day.

Missing Q_H and Q_E data on July 13 is the result of low vapour pressure gradients which prevented the use of the BREB approach for portions of this day.

Missing Q^* and Q_G data on July 14 prevented the use of the BREB approach to determine Q_H and Q_E on this day. The Q^* and Q_G data was not available due to data recording problems.

The storm on July 16 and July 17 resulted in low vapour pressure gradients which prevented the use of the BREB approach to determine Q_H and Q_E on these days.

REFERENCES

Addison, P.A. and L.C. Bliss, 1980, Summer Climate, Micro-climate and Energy Balance of a Polar Semi-Desert on King Christian Island, N.W.T., Canada, Arctic and Alpine Research, 12: 161-170.

Aufdemberge, T. P., 1974, Energy Balance Studies over Glacier and Tundra Surfaces, Chittistone Pass, Alaska, Summer 1969. In Icefield Ranges Research Project, Vol. 4 , edited by V.C. Bushnell and M.G. Marcus. American Geographical Society and Arctic Institute of North America: 29-32.

Bailey, W.G., 1983, Modelling Hourly and Daily Evaporation from Cropped Surfaces. In Proceedings of the 5th Conference on Hydrometeorology, Oct. 17-19, 1983, Tulsa, OK, American Meteorological Society, Boston, Mass.: 229-235.

Bailey, W.G. and J.A. Davies, 1981a, The Effect of Uncertainty in Aerodynamic Resistance on Evaporation Estimates from the Combination Model, Boundary-Layer Meteorology, 20: 187-199.

Bailey, W.G. and J.A. Davies, 1981b, Bulk Stomatal Resistance Control on Evaporation, Boundary-Layer Meteorology, 20: 401-415.

Ball, D.F., 1964, Loss-On-Ignition as an Estimate of Organic Matter and Organic Carbon in Non-Calcareous Soils, Journal of Soil Science, 15: 84-92.

Barry, R.G., 1979, High Altitude Climates, In High Altitude Geoecology, edited by P.J. Weber. American Association for the Advancement of Science: 55 74.

Barry, R.G., 1981, Mountain Weather and Climate , Meuthen, New York, 313 pp.

Barry, R.G. and J.D. Ives, 1974, Introduction. In Arctic and Alpine Environments, edited by J.D. Ives and R. Barry, Methuen, London: 1-13.

Bradley, E.F. 1969, A Small Scale Anemometer System for Agricultural Meteorology, Agricultural Meteorology, 6: 185-194.

Bradley, E.F. 1972, The Influence of Thermal Instability on a Drag Coefficient Measured Close to the Ground, Agricultural Meteorology, 9: 183-190.

Brazel, A.J., 1970, Surface Heat Exchange at Chitistone Pass, Alaska, Proceedings of the American Association of Geographers, 2: 26-30.

Brazel, A.J., and S.I. Outcalt, 1973, The Observation and Simulation of Diurnal Surface Thermal Contrast in an Alaskan Alpine Pass, Arch. Met. Geoph. Biokl., Ser. B, 21: 157-174.

Brunt, D., 1932, Notes on Radiation in the Atmosphere: I, Quarterly Journal of the Royal Meteorological Society, 58: 389-420.

Brutsaert, W., 1975, On a Derivable Formula for Long-wave Radiation from Clear Skies, Water Resources Research, 11: 742-744.

Brutsaert, W., 1982, Evaporation into the Atmosphere, Theory, History and Applications , D. Reidel Publishing, Dordrecht, Holland, 299 pp.

Bryant, J.P. and E. Scheinberg, 1970, Vegetation and Frost Activity on an Alpine Fellfield on the Summit of Plateau Mountain, Alberta, Canadian Journal of Botany, 48: 751-771.

Budyko, M.I., 1974, Climate and Life, Academic Press, New York, 508 pp.

Davies, J.A., 1963, Albedo Investigations in Labrador-Ungava, Arch. Met. Geoph. Biokl., Ser. B, 13: 137-150.

Davies, J.A., 1967, A Note on the Relationship Between Net Radiation and Solar Radiation, Quarterly Journal of the Royal Meteorological Society, 93: 109-115.

Davies, J.A. and C.D. Allen, 1973, Equilibrium, Potential and Actual Evaporation from Cropped Surfaces in Southern Ontario, Journal of Applied Meteorology, 12: 649-657.

Davies, J.A. and S.B. Idso, 1979, Estimating the Surface Radiation Balance and its Components. In Modification of the Aerial Environment of Crops, edited by B.J. Barfield and J.F. Gerber, American Society of Agric. Eng., St. Joseph, MI: 183-210.

Davies, J.A., W. Schertzer and M. Nunez, 1975, Estimating Global Solar Radiation, Boundary-Layer Meteorology, 9: 33-52.

Denmead, O.T., 1976, Temperate Cereals. In Vegetation and the Environment, Vol. 2. Edited by J.L. Monteith, Academic Press, London: 1-30.

Dyer, A.J., 1967, The Turbulent Transport of Heat and Water Vapour in an Unstable Atmosphere, Quarterly Journal of the Royal Meteorological Society, 93: 501-508.

Dyer, A.J., 1974, A Review of Flux Profile Relationships, Boundary-Layer Meteorology, 7: 363-372.

Dyer, A.J. and B.B. Hicks, 1970, Flux-Gradient Relationships in the Constant Flux Layer, Quarterly Journal of the Royal Meteorological Society, 96: 715-721.

Enz, J.W., J.L. Clink and D.G. Baker, 1975, Solar Radiation Effects on Pyrgeometer Performance, Journal of Applied Meteorology, 14: 1297-1302.

Fox, D.G., 1981, Judging Air Quaility Model Performance, Bulletin of the American Meteorological Society, 62: 599-609.

Fritschen, L.J., 1967, Net and Solar Radiation Relations Over Irrigated Field Crops, Agricultural Meteorology, 4: 55-62.

Fuchs, M. and C.B. Tanner, 1968, Surface Temperature Measurements of Bare Soils, Journal of Applied Meteorology, 7: 302-305.

Fuchs, M. and C.B. Tanner, 1970, Error Analysis of Bowen Ratios Measured by Differential Psychrometry, Agricultural Meteorology, 7: 329-334.

Garret, J.R. and B.B. Hicks, 1973, Momentum, Heat and Water Vapour Transfer to and From Natural and Artificial Surfaces, Quarterly Journal of the Royal Meteorological Society, 99: 680-687.

Gash, J.H.C. and J.B. Stewart, 1975, The Average Surface Resistance of a Pine Forest Derived from Bowen Ratio Measurements, Boundary-Layer Meteorology, 8: 453-464.

Gates, D.M., and R. Janke, 1966, The Energy Environment of the Alpine Tundra, Oecologia Plantarum, 1: 39-61.

Gay, L.W., 1971, The Regression of Net Radiation Upon Solar Radiation, Arch. Met. Geoph. Biokl., Ser. B, 19: 1-14.

Geiger, R., 1961, The Climate Near the Ground , Harvard University Press, Cambridge, Mass., 611 pp.

Greenland, D. and B. Clothier, 1975, A Study of Radiation in the New Zealand Southern Alps, Geografiska Annaler A, 57: 143-151.

Hare, K.H. and M.K. Thomas, 1979, Climate Canada, 2nd Edition, John Wiley and Sons, Toronto, 230 pp.

Harris, S.A. and R.J.E. Brown, 1978, Plateau Mountain: A Case Study of Alpine Permafrost in the Canadian Rocky Mountains. In Proceedings of Third International Conference on Permafrost, July 10-13, 1978, Edmonton, Alberta, National Research Council, Ottawa: 385-391.

Hatfield, J.L. and D.F. Wanjura, 1985, Actual Evapotranspiration from Dryland Agriculture, In Proceedings of the National Conference on Advances in Evapotranspiration, December 16-17, 1985, Chicago, IL American Society of Agric. Eng., St. Joseph, MI: 151-158.

Hillel, D., 1982, Introduction to Soil Physics, Academic Press, New York, 364 pp.

Holland, W.D. and G.M. Cohen, Eds., 1982, Ecological (Biophysical) Land Classification of Banff and Jasper National Parks, Publication number SS-82-44, Alberta Institute of Pedology, Edmonton.

Idso, S.B., 1971, Relations Between Net and Solar Radiation, Journal of Met. Soc. of Japan, Series 2, 49: 1-12.

Idso, S.B., 1974, On the Use of Equations to Estimate Atmospheric Thermal Radiation, Arch. Met. Geoph. Biokl., Ser. B, 22: 287-299.

Idso, S.B., D.G. Baker and B.L. Blad, 1969a, Relations of Radiation Fluxes over Natural Surfaces, Quarterly Journal of the Royal Meteorological Society, 95: 244-257.

Idso, S.B., R.D. Jackson, W.L. Ehrler and S.T. Mitchell, 1969b, A Method for Determination of Infrared Emittance of Leaves, Ecology, 50: 899-902.

Jackson, R.D. and S.B. Idso, 1975, Surface Albedo and Desertification, Science, 189: 1012-1013.

Johns, D., J.B. Beard and C.H.M. van Bavel, 1983, Resistances to Evapotranspiration from a St. Augustinegrass Turf Canopy, *Agronomy Journal*, *75*: 419-422.

Kanemasu, E.T., M.L. Wesley, B.B. Hicks and J.L. Heilman, 1979, Techniques for Calculating Energy and Mass Fluxes. In *Modification of the Aerial Environment of Crops*, edited by B.J. Barfield and J.F. Gerber, American Society of Agric. Eng., St. Joseph, MI: 156-182.

Lang, H., 1981, Is Evaporation an Important Component in High Alpine Hydrology, *Nordic Hydrology*, *12*: 217-224.

LeDrew, E.F., 1975a, Energy Balance of a Mid-Latitude Alpine Site During the Growing Season, 1973, *Arctic and Alpine Research*, *7*: 301-314 .

LeDrew, E.F., 1975b, Estimation of Clear Sky Atmospheric Emittance at High Altitudes, *Arctic and Alpine Research*, *7*: 227-236 .

LeDrew, E.F. and G. Weller, 1978, A Comparison of the Radiation and Energy Balance During the Growing Season for an Arctic and Alpine Tundra, *Arctic and Alpine Research*, *10*, 665-678.

Lewis, M.C. and T.V. Callaghan, 1976, Tundra, In *Vegetation and the Environment*, *Vol. 2*. Edited by J.L. Monteith, Academic Press, London: 399-433.

Löve, D., 1970, Subarctic and Subalpine: Where and What?, *Arctic and Alpine Research*, *2*: 63-73.

Lowry, W.P., 1980, Clear-Sky Direct-Beam Solar Radiation vs. Altitude: A Proposal for Standard Soundings, *Journal of Applied Meteorology*, *19*: 1323-1327.

Marcus, M.G., 1973, The High Mountain Environment Project. In *Icefield Ranges Research Project*, *Vol. 4* , edited by V.C. Bushnell and M.G. Marcus. American Geographical Society and Arctic Institute of North America: 63-79.

Marsh, P., W.R. Rouse and Ming-Ko Woo, 1981, Evaporation at a High-Arctic Site, *Journal of Applied Meteorology*, *20*: 713-716.

Mawdsley, J.A. and M.F. Ali, 1985, Estimating Nonpotential Evapotranspiration by means of the Equilibrium Evaporation Concept, *Water Resources Research*, *21*: 383-391.

McKeague, J.A., 1972, *Manual of Soil Sampling and Methods of Analysis, Second Edition* , Canadian Society of Soil Science, 212 pp.

Monteith, J.L., 1965, Evaporation and the Environment. In *The State and Movement of Water in Living Organisims*, *19th Symp. Soc. Exp. Biol.* , University Press, Cambridge: 205-234.

Monteith, J.L., 1973, *Principles of Environmental Physics*, Edward Arnold, London, 240 pp.

Monteith, J.L., 1981, Evaporation and Surface Temperature, *Quarterly Journal of the Royal Meteorological Society*, *107*: 494-500.

Munro, D.S., 1982, On Determining Volumetric Soil Moisture Variations in Peat by the Gravimetric Method, *Soil Science, 133*: 103–110.

Murray, F.W., 1967, On the Computation of Saturation Vapour Pressure, *Journal of Applied Meteorology, 6*: 203–204.

Nkemdirim, L.C., 1972, A Note on the Albedo of Surfaces, *Journal of Applied Meteorology, 19*: 867–874.

Nkemdirim, L.C., 1973, Radiative Flux Relations over Crops, *Agricultural Meteorology, 11*: 229–242.

Ogilvie, R.T., 1976, The Alpine and Subalpine in the Rocky Mountains of Alberta. In *Proceedings of a Workshop on Alpine and Subalpine Environments*, Resources Analysis Branch, Ministry of the Environment, Victoria, B.C.: 34–46.

Ohmura, A., 1982, Evaporation from the Surface of the Arctic Tundra on Axel Heiberg Island, *Water Resources Research, 18*: 291–300.

Oke, T.R., 1978, *Boundary Layer Climates*, Methuen, London, 372 pp.

Panofsky, H.A., 1963, Determination of Stress from Wind and Temperature Measurements, *Quarterly Journal of the Royal Meteorological Society, 89*: 85–94.

Peattie, R., 1936, *Mountain Geography*, Greenwood Press, New York, 257 pp.

Penman, H.L., 1948, Natural Evaporation from Open Water, Bare Soil and Grass, *Proceedings of the Royal Society of London, Series A, 193*: 120–145.

Petzold, D.E. and A.N. Rencz, 1975, The Albedo of Selected Subarctic Surfaces, *Arctic and Alpine Research, 7*: 393–398.

Price, L.W., 1981, *Mountains and Man*, University of California Press, Berkeley, 506 pp.

Priestley, C.H.B., and R.J. Taylor, 1972, On the Assessment of Surface Heat Flux and Evaporation Using Large Scale Parameters, *Monthly Weather Review, 100*: 81–92.

Pruitt, W.O. and F.L. Lourence, 1969, A Psychrometer System for Micrometeorology Profile Determination, *Journal of Applied Meteorology, 8*: 492–498.

Ripley, E.A. and R.E. Redmann, 1976, Grassland, In *Vegetation and the Environment, Vol. 2*. Edited by J.L. Monteith, Academic Press, London: 351–396.

Rott, H., 1979, Vergleichende Untersuchungen der Energiebilanz im Hochgebirge, *Arch. Met. Geoph. Biokl., Ser. A., 28*: 211–232.

Rouse, W. R., 1984, Microclimate at the Arctic Treeline, 1, Radiation Balance of Tundra and Forest, *Water Resources Research, 20* : 57–66.

Rouse, W.R. and R.B. Stewart, 1972, A Simple Model for Determining Evaporation from High Latitude Upland Sites, *Journal of Applied Meteorology, 11*: 1063–1070.

Rouse, W.R., P. Mills and R.B. Stewart, 1977, Evaporation in High Latitudes, *Water Resources Research, 13*: 909-914.

Sellers, W.D., 1965, *Physical Climatology*, University of Chicago Press, Chicago, 272 pp.

Schmugge, T.J., T.J. Jackson and H.L. Mckim, 1980, Survey of Methods for Soil Moisture Determination, *Water Resources Research, 16*: 961-979.

Slatyer, R.D. and I.C. McIlroy, 1961, *Practical Microclimatology*, Council for Scientific and Industrial Research, Melbourne, Australia, 310 pp.

Slaymaker, H.0., 1974, Alpine Hydrology. In *Arctic and Alpine Environments*, edited by J.D. Ives and R. Barry, Methuen, London: 135-158.

Staudinger, M. and H. Rott, 1981, Evaporation at Two Mountain Sites During the Vegetation Period, *Nordic Hydrology, 12*: 207-216.

Stewart, J.B., 1971, The Albedo of a Pine Forest, *Quarterly Journal of the Royal Meteorological Society, 97*: 561-564.

Stewart, R.B., 1972, *An Evaporation Model for High Latitude Upland Lichen Surfaces*, unpublished M. Sc. thesis, McMaster University, Hamilton, Ont., 47 pp.

Stewart, R.B. and W.R. Rouse, 1976, Simple Models for Calculating Evapotranspiration for Dry and Wet Tundra Surfaces *Arctic and Alpine Research, 8*: 263-274.

Swinbank, W.C., 1951, The Measurement of Vertical Transfer of Heat and Water Vapour by Eddies in the Lower Atmosphere, *Journal of Meteorology, 8*: 135-145.

Swinbank, W.C., 1963, Longwave Radiation from Clear Skies, *Quarterly Journal of the Royal Meteorological Society, 89*: 339-348.

Szeicz, G. and I.F. Long, 1969, Surface Resistance of Crop Canopies, *Water Resources Research, 5*: 380-394.

Tan, C.S., and T.A. Black, 1976, Factors Affecting the Canopy Resistance of a Douglas-Fir Forest, *Boundary-Layer Meteorology, 10*: 475-488.

Tanner, C.B., 1963, *Soils Bulletin 6: Basic Instrumentation and Measurements for Plant Environment and Micrometeorology*, Evapotranspiration Measurements. Dept. of Soil Science, College of Agriculture, University of Wisconsin, Madison, WIS.

Tanner, B.D., M.S. Tanner, W.A. Ducas, E.C. Campbell and B.L. Bland. 1985, Evaluation of an Operational Eddy Correlation System for Evapotranspiration Measurements. In *Proceedings of the National Conference on Advances in Evapotranspiration, December 16-17, 1985, Chicago, IL* American Society of Agric. Eng., St. Joseph, MI: 87-99.

Terjung, W.P., R. Kickert, G.L. Potter and S.W. Swarts, 1969, Energy and Moisture Balances of an Alpine Tundra in Mid-July, *Arctic and Alpine Research, 1*: 247-266.

Thom, A.S. 1972, Momentum, Mass and Heat Exchange of Vegetation, Quarterly Journal of the Royal Meteorological Society, 98: 124–134.

Thom, A.S. 1975, Momentum, Mass and Heat Exchange of Plant Communities. In Vegetation and the Atmosphere, Vol. 1 , edited by J.L. Monteith, Academic Press, London: 57–109.

Turner, H., P. Rochat and A. Streule, 1975, Thermische Charakteristik von Hauptstandurtstypen im Bereich der Oberen Walgrenze, Mitt. Eidg. Anstalt Forstl. Versuchwesen, 51: 95–119.

Willmott, C.J., 1982, Some Comments on the Evaluation of Model Performance, Bulletin of the American Meteorological Society, 63: 1309–1313.

Wilson, R.C. and H.S. Hudson, 1981, Variations of Solar Irradiance, Astrophysical Journal, Letters, 244,: L185–L189.

Wilson, R.G., 1971, The Concept of Equilibrium Evapotranspiration, Climatological Bulletin, 9: 1–8.

Wilson, R.G. and W.R. Rouse, 1972, Moisture and Temperature Limits of the Equilibrium Evapotranspiration Model, Journal of Applied Meteorology, 11,, 436–442.

Yaglom, A.M., 1977, Comments on Wind and Temperature Flux Profile Relationships, Boundary-Layer Meteorology, 11, 89–102.

Zwinger, A.H. and B.E. Willard, 1972, Land Above the Trees: A Guide to American Alpine Tundra, Harper and Row, New York, 489 pp.